# Experimentally observing discharge characteristics of Si-air batteries

Using KOH and BMPyr[NTf2] as electrolytes

by

Michael Zhu

Student number: 4575857

Thesis committee: Dr. R.A.C.M.M van Swaaij EEMCS/ESE/PVMD - supervisor

Prof.dr.ir. A.H.M. Smets

Dr. E.M. Kelder

Project Duration: November 2022 - July 2023

Faculty: EEMCS

Style: TU Delft Report Style, with modifications by Daan Zwan-

EEMCS/ESE/PVMD

AS/RST/SEE

eveld



## **Abstract**

An increasing penetration of renewable energy sources in the global energy market necessitates an increasing amount of energy storage. Batteries are an excellent source of short term storage, used in vehicles, home storage and mobile applications. However modern technologies such as Li-ion batteries face resource scarcity and hence introduce geopolitical dependence. To this end Si-air batteries were recently, in 2009, explored in an attempt to devise a battery with high energy density and abundant materials.

The Si-air battery makes use of a silicon anode and an porous carbon cathode, to allow the circulation of air into the battery. Two electrolytes have been looked at in the past, KOH and the Room Temperature Ionic Liquid (RTIL) EMIm(HF) $_{2.3}$ F. The Si-air battery has excellent energy density in theory, with volumetric density being theoretically as high as  $1 \cdot 10^4$  Wh/L. However, this theoretical energy density is as of yet far from reached, current research uses electrolytes which have a parasitic corrosion reaction with the silicon anode. This work aims to explore the usage of a new RTIL, BMPyr[NTf $_2$ ], as the electrolyte in this battery. This RTIL has seen usage in Zn-air batteries, however it is yet untested for Si-air. The objective is to determine the discharge characteristics for a Si-air battery using this RTIL through comparison with KOH, with focus on the conductivity.

To do so first the relationship between conductivity and discharge potential for KOH was determined experimentally. The result found is that the discharge potential using KOH decreases with decreasing conductivity, however, this decrease is much larger than what can be solely attributed to the conductivity.

Next the chosen RTIL BMPyr[NTf $_2$ ], having a conductivity of 2.2 mS/cm at room temperature in a pristine state, was used in the battery discharges, where it was established to have an OCP of 0.7-0.8 V. From measurements no detectable consumption of Si was found after 1 hour of OCP. Further during the discharges it was found that the potential drops rapidly when discharge current is equal or greater to 2.5  $\mu$ A. In an attempt to decrease the resistance in the battery cell a new design was created where the distance between the two electrodes is decreased from 2 cm to 0.8 cm, using this second design a maximum OCP of 1.1 V was measured.

Finally by mixing in 1wt% and 3wt% water into the RTIL two mixtures are obtained with conductivity of 2.6 mS/Cm and 3.0 mS/cm at room temperature. Discharging these two mixtures at 20 nA, 100 nA, 500 nA and 2.5  $\mu$ A it was found that for the 1 wt% the highest potential was found for 20 nA at 0.8 V. Meanwhile for the 3 wt% mixture the 20 nA discharge exhibited significantly lower potential at 0.4 V. For the 100 nA, 500 nA and 2.5  $\mu$ A increasing conductivity led to increased potential, however similar to the KOH experiment, this difference in potential is larger than what is to be expected from purely conductivity changes. Finally, reproducibility of these experiments is low as a series of discharges with the same materials and current showed different potentials. These results combined lead to the conclusion of this work, that the relationship between conductivity and potential for the RTIL BMPyr[NTf2] is inconclusive, there are unknown factors influencing the discharge potential.

# Acknowledgements

This research was not done alone, here I would like to thank all who have helped me with this work and through their assistance led me to this finalized report. Their help was crucial to achieving these results and as such are to be acknowledged.

First is my supervisor Dr. René van Swaaij, he is the one who introduced this thesis topic to me and has been with me throughout the entire process. His expertise and prior knowledge in this field have been invaluable, it is through his experience that I found a starting point for this research. During my 8 months working on this project he has made time weekly to discuss my progress and offer guidance when needed. His incisive remarks upon my results have assisted me greatly in refining and improving this report, this report would be greatly lessened without his assistance.

Secondly I would like to extend my gratitude to the staff of the EKL and the PVMD group for the training and assistance offered, with emphasis on the technicians Martijn Thijssen and Stefaan Heirman. Who both have taken their time to assist me in operating the various machinery and equipment available in the EKL Cleanrooms. Martijn in particular has teached me the procedures regarding the usage of the PVMD wet benches within the CR 10000. Martijn and Stefaan both have assisted me greatly with logistical issues such as ordering the materials used during the experiments, without which this report would be fully theoretical.

Thirdly, I offer my thanks to Prof. Arno Smets and Prof. Erik Kelder for taking time out of their busy schedules in the holiday season to take a seat in my thesis defence committee.

Finally, I would like to thank my friends and family for supporting me during this process, being understanding of my occasional unavailability.

M. Zhu Delft, July 2023

# Contents

Ab	strac	ct									i
Αc	knov	vledgei	nents								ii
Lis	st of I	Figures	<b>;</b>								٧
Lis	st of 7	Tables									ix
1	Intro	ductio	n								1
	1.1 1.2 1.3 1.4 1.5 1.6	Renew Storag Batteri Metal-	fuels		 	 	 	 	 	   	 1 3 5 7 7 8
2	Si-ai	ir Batte	ries								9
	2.2 2.3 2.4	2.1.1 2.1.2 2.1.3 Metal-Anode Cathod Electro 2.5.1 2.5.2	ations of battery op Red-Ox Reactions Working Principle Overpotentials air batteries		 			 			 9 10 11 12 13 14 15 15 17 22
3	•		tal Method								24
	3.1		mental Environmen construction Anode Cathode Electrolyte Battery Design	  	   	 	 	   	 	   	 24 24 24 26 26 27
	3.3 3.4	Measu Experi 3.4.1 3.4.2 3.4.3	rement	ion entrations	 	 	 	 	 	 	 28 32 32 33 33 34
4	<b>Res</b> i 4.1	Verifica	ation of setup Reproducibility			 	 	 	 	 	<b>36</b> 36 36

Contents

4.1.2 Comparing silicon anodes 4.1.3 Comparing battery design 4.2 RTIL characterization 4.2.1 Initial Test 4.2.2 Boundary testing 4.2.3 Limiting factors 4.2.4 Comparing battery design 4.3 KOH concentrations 4.4 RTIL water mixing  5 Discussion 5.1 Battery cell 5.1.1 Inconsistent Native Oxide 5.1.2 Curved Anode Samples 5.2 KOH 5.2.1 Corrosion & OCP period 5.2.2 Leakage & Evaporation 5.3 RTIL 5.3.1 Miscibility & Reproducibility 5.3.2 Low Current 6 Conclusion 6.1 Conclusions 6.2 Recommendations  References  A Error Calculation Dektak
4.1.3 Comparing battery design  4.2 RTIL characterization  4.2.1 Initial Test  4.2.2 Boundary testing  4.2.3 Limiting factors  4.2.4 Comparing battery design  4.3 KOH concentrations  4.4 RTIL water mixing  5 Discussion  5.1 Battery cell  5.1.1 Inconsistent Native Oxide  5.1.2 Curved Anode Samples  5.2 KOH  5.2.1 Corrosion & OCP period  5.2.2 Leakage & Evaporation  5.3 RTIL  5.3.1 Miscibility & Reproducibility  5.3.2 Low Current  6 Conclusion  6.1 Conclusions  6.2 Recommendations
4.1.3 Comparing battery design  4.2 RTIL characterization 4.2.1 Initial Test 4.2.2 Boundary testing 4.2.3 Limiting factors 4.2.4 Comparing battery design  4.3 KOH concentrations 4.4 RTIL water mixing  5 Discussion 5.1 Battery cell 5.1.1 Inconsistent Native Oxide 5.1.2 Curved Anode Samples  5.2 KOH 5.2.1 Corrosion & OCP period 5.2.2 Leakage & Evaporation  5.3 RTIL 5.3.1 Miscibility & Reproducibility 5.3.2 Low Current  6 Conclusion 6.1 Conclusions
4.1.3 Comparing battery design  4.2 RTIL characterization  4.2.1 Initial Test  4.2.2 Boundary testing  4.2.3 Limiting factors  4.2.4 Comparing battery design  4.3 KOH concentrations  4.4 RTIL water mixing  5 Discussion  5.1 Battery cell  5.1.1 Inconsistent Native Oxide  5.1.2 Curved Anode Samples  5.2 KOH  5.2.1 Corrosion & OCP period  5.2.2 Leakage & Evaporation  5.3 RTIL  5.3.1 Miscibility & Reproducibility
4.1.3 Comparing battery design  4.2 RTIL characterization 4.2.1 Initial Test 4.2.2 Boundary testing 4.2.3 Limiting factors 4.2.4 Comparing battery design  4.3 KOH concentrations 4.4 RTIL water mixing  5 Discussion 5.1 Battery cell 5.1.1 Inconsistent Native Oxide 5.1.2 Curved Anode Samples  5.2 KOH 5.2.1 Corrosion & OCP period
4.1.3 Comparing battery design  4.2 RTIL characterization 4.2.1 Initial Test 4.2.2 Boundary testing 4.2.3 Limiting factors 4.2.4 Comparing battery design  4.3 KOH concentrations 4.4 RTIL water mixing  5 Discussion 5.1 Battery cell 5.1.1 Inconsistent Native Oxide
4.1.3 Comparing battery design  4.2 RTIL characterization  4.2.1 Initial Test  4.2.2 Boundary testing  4.2.3 Limiting factors  4.2.4 Comparing battery design  4.3 KOH concentrations

# List of Figures

1.1	Years of fossil fuel left as of 2020. Retrieved from [4]	1
1.2	Displayed are the Brent crude oil price, dutch title transfer facility day-ahead gas price, the Rotterdam coal futures price and the electricity is the weighted	
	average of the five largest electricity markets in Europe. The prices shown here	
	are relative to the price observed on 23 February 2022, where the prices on	
	that date are defined as 100. The grey vertical line denotes the intensification	
	of hostilities in the Ukrainian/Russian conflict. Retrieved from [7].	2
1.3	This figure shows the CO <sub>2</sub> levels from the last 10000 years, obtained through ice cores for older measurements and direct air measurements for the most	
	recent ones. Retrieved on 30-5-2023 from [11]	3
1.4	Given here are the global annual renewable energy growth per source, given	
	in GW. The last four columns represent forecasted energy growth for 2023 and	
1 5	2024. Retrieved from [17]	4
1.5	Depicted are the generation of the same PV system on two different days. Retrieved from [18]	4
1.6	This figure shows the typical time scale of the most relevant storage technolo-	4
1.0	gies as a function of the typical capacity scale. Retrieved from [19]	5
1.7	Displayed are the cost per kWh in USD for three different types of Li-ion battery	
	usage. Vertical lines denote a doubling in global cumulative capacity installed.	
	Retrieved from [21]	6
1.8	This figure shows the global yearly growth, in GW, of battery storage for different	
	countries. Retrieved from [20].	6
2.1	An example of the Butler-Volmer equation	11
2.2	The theoretical gravimetric and volumetric capacities of a selected few metal-air	
	pairs and gasoline. Adapted from [34]	12
2.3	Presence of elements inside the earth's crust given in microgram per gram given	
	in log scale. Retrieved from [47]	13
2.4	Air cathode which comprises of three distinct layers, the gas diffusion, current	
2.5	collector and catalyst layers. Taken from [50]	14
2.5	Conductivity of KOH at various temperatures from a series of sources. Through each of the data points there is a curve plotted approximating the conductivity	
	according to an equation. Retrieved from and compiled by [61]	16
2.6	Here is shown in a) the clogging mechanism at low discharge current and in b)	. 0
	the mechanism at high current. Retrieved from [38]	18
2.7	Depicted in (a) is a proposed surface reaction of the Zn-air battery pair when	
	using pristine BMPyr[NTf2], where the formation of a surface layer occurs. In (b)	
	is shown the proposed reaction when water is introduced, acting as a transport	
	for the zinc ions, preventing the formation of this layer. Figure adapted from [39].	
2.8	Displayed in (a) are the discharge curves using 0.5wt% water mixed with BMPyr[N7	$[t_2]$
	for various currents and in (b) are shown the discharge using various different	
	wt% water mixed with BMPyr[NTf <sub>2</sub> ] with the highest current still providing stable discharge. Figure taken from [39].	21
	- ulbonaryo. i lyuro takon iloni jodj	

List of Figures vi

2.9	Shown here are the chemical structures of the two candidates, on the left side is shown the BMIm based RTIL and on the right side the BMPyr based RTIL. Retrieved from [70]	22
2.10	Shown here are the a) the first 4 charge/discharge cycles from the secondary Si-air battery and b) the measured coulombic efficiency for the first 10 cycles, note that after the $6_th$ cycle the electrolyte is refreshed. Retrieved from [75].	23
3.1 3.2	A roll of the cathode. Partially used up	26
3.3	from [48]	27
3.4	more than twice as thin, at only 8 mm thickness	27
3.5	O-rings. Retrieved from [48]	28
3.6	what type of discharge happens and the current range	29 29
3.7	The interior of the Dektak profilometer, the sample is to be placed on the silver coloured disc and has to be manually put into position beneath the red needle.	31
3.8	Shown here is the battery cell in various stages of assemblage. The stages are denoted by letters, A to D and correspond to the following situations. A, the cathode is cut into the correct shape and placed on the center piece. B, the cathode side is fixed in place using an outer piece and bolts. C, the anode is prepared and placed on the other side of the center piece. D, the anode is fixed in place using an outer piece and bolts.	32
4.1	1 hour OCP and 6 hour discharge at 10 μA using a Topsil wafer. The OCP	52
4.2	period is highlighted in grey	36
4.3	sample lengthwise	37
4.4	each measurement is held at OCP, again highlighted in grey Displayed are the heights of both the Siegert and the Topsil samples. Of note is that one of the Topsil measurements used a larger scan length than the remainder of the measurements, however this has no impact on the step itself	38 39

List of Figures vii

4.5	Plotted here are the calculated mass on the y-axis against the weighed mass on the x-axis. In black is a line representing the two masses being equal. A first order polynomial fit is made through the data points.	40
4.6	Given in this figure is the total mass consumed versus the time for both anodes, using the mass determined by a scale. Included are the first order polynomial	
4.7	fits of the data points and their 95% confidence intervals	41
4.8	after 10 hours	42
4.9	of 2.0 cm	42
4.10	the native oxide and once without	43
4.11	changed. Pristine RTIL was used for these discharges	44
4.12	ing reused midway in a 20 minute discharge. The legend denotes which component was reused for which graph	45
4.13	with the old battery cell and one with the new cell. This measurement has as result that the OCP of the new cell is higher than that of the old cell Plotted here is the conductivity of KOH as obtained from Equation 2.11 using	46
4 14	T = 294.15 K. Vertical lines denote the concentrations which were used in this experiment, accompanying horizontal lines point to the conductivity Displayed are two sets of discharge curves for varying KOH concentration. Dis-	47
	played in (a) are the discharges at 1 $\mu$ A and in (b) those at 50 $\mu$ A. Notably the discharge curves on the left show erratic behaviour. Meanwhile the curves on the right exhibit stable behaviour, with sharper decreases in potential only	47
4.15	occurring after more than 10 hours have past	47 48
4.16	Shown here are in (a) the step heights obtained from the samples discharged with KOH at 50 $\mu$ A and in (b) the corresponding mass, obtained using the	
4.17	method described in Appendix A	49
4.18	and 2.5 $\mu$ A	50 51
5.1	This picture shows four samples taken from the CD holder at random. They are each submerged in water and then taken out and flipped horizontally such that a picture may be taken. The residual water on sample A is clearly different when compared to samples B, C and D. Where in A the water is diffused over the entire surface, meanwhile in B, C and D they form distinct droplets	53

List of Figures viii

5.2	Step height of an unused anode. Two graphs are included, one going vertically across the middle of the sample and one going diagonally across the sample. Both measurements were done on the same side of the sample. The vertical middle measurement has a major spike on the right side of the graph, likely caused by surface contaminants.	54
5.3	An 24 hour discharge using a Siegert sample, where it can be seen that the OCP is of a low value up until 15 hours into the measurement, unlike the expected value of 40 minutes.	55
5.4	The step heights measured for the discharges done at a current of 1 $\mu$ A. Notable is that with exception of the 6.6M KOH discharge, the step heights are highly erratic, where a flat plane was expected	56
5.5	Shown here are a set of pictures showing leakage. On the left side is shown the backside of the cathode being wet. And on the right is seen liquid surrounding the cathode, outside of the smaller O-ring.	57
5.6	Displayed in this picture is the battery cell after a 20 hour discharge using KOH.  During this discharge a cap was placed on the battery cell to seal off the electrolyte inlet. Encircled is the cathode holder where liquid is visible	58
5.7	Presented in this figure is a picture of the RTIL, BMPyr[NTf <sub>2</sub> ], being mixed with water. Note that due to the a-polar vs polar interaction an emulsion is created, but only at a thin layer near the surface due to the imbalance in the two liquid	50
5.8 5.9	quantities and densities	59 59 60
A.1	Dektak and on the right side the leveled step height	70
A.2	Shown here are on the left side pre-step height and on the right side the post-step height with a fit included	71
B.1 B.2	Shown here is the mass versus the calculated mass, using an area of 1.6 cm <sup>2</sup> . Shown here is an small O-ring intended to be placed on the anode sample. The inner and outer diameter are visualized by usage of the red lines and the ruler	72
B.3	at the bottom	73
	below	73

# List of Tables

2.1	Shown here are the parameters of the discussed RTIL's, where the values are all given for a room temperature of 20 degrees celsius	22
3.1	Shown here are the parameters of the two brands of wafers, note that both are essentially identical	25
4.1	Shown here are the conductivities of the RTIL as measured using the conductivity meter. Also given is the temperature of the conductivity during the measurement.	50

## Introduction

#### 1.1. Fossil fuels

Currently, the global consumption of energy is expected to keep increasing with time [1], however, with estimates of some fossil fuel reserves being exhausted as early as 2050 [2][3] this growth cannot be sustained without some alternative form of power generation. In Figure 1.1 the reserves can be seen as of 2020, with the time based on the annual consumption rate at that time.

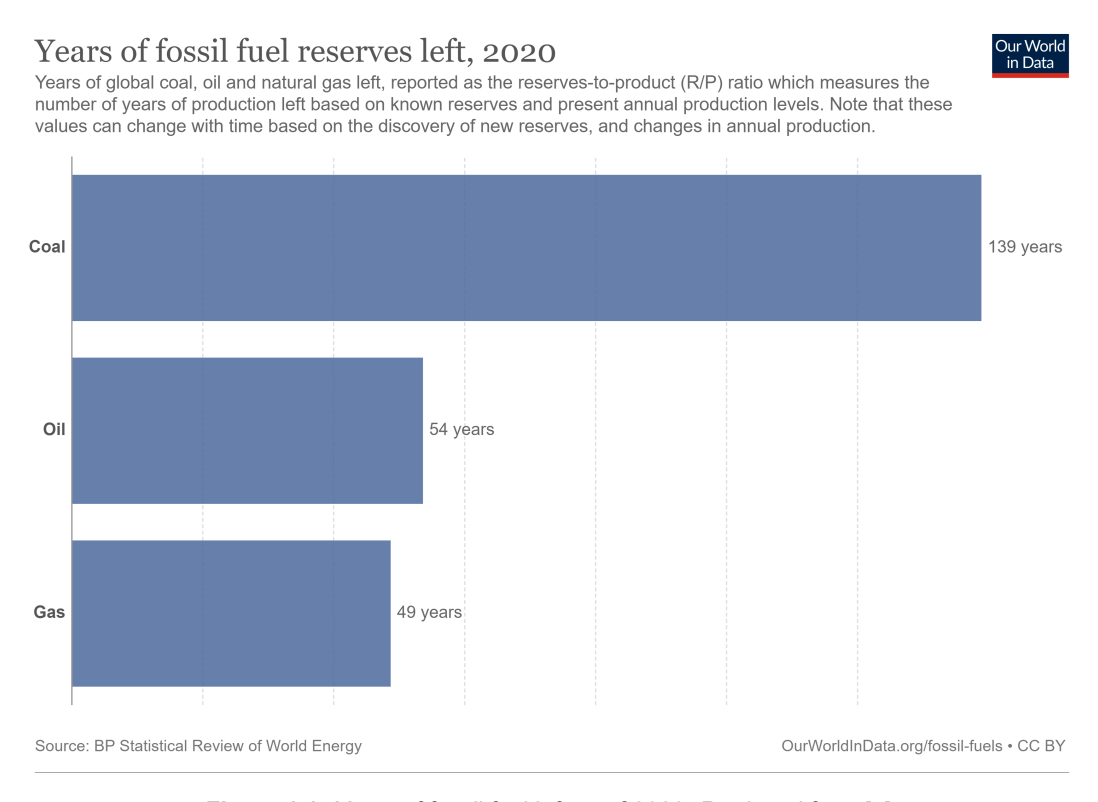


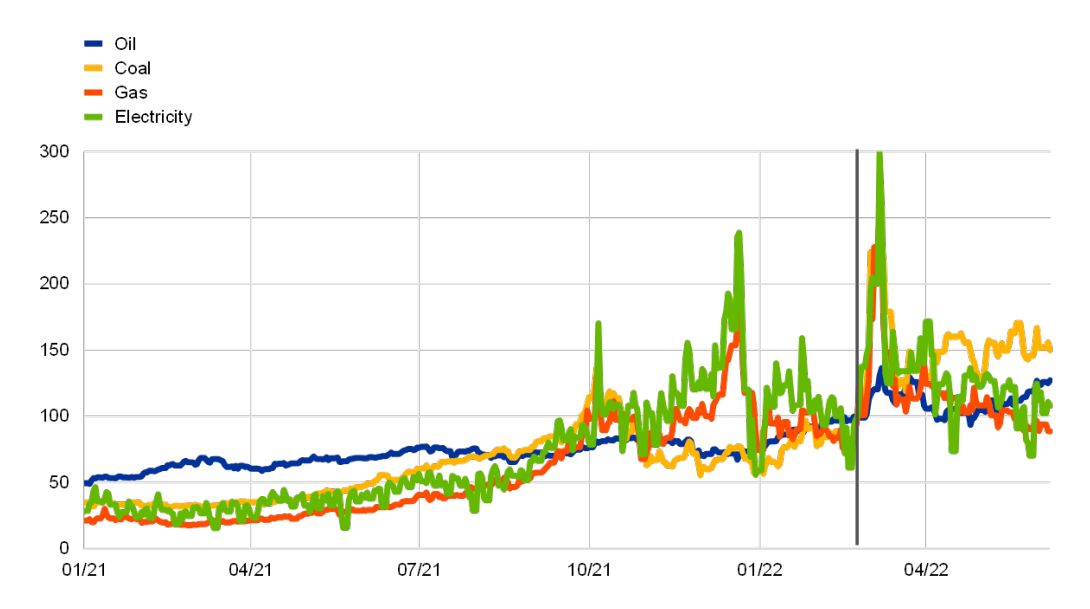
Figure 1.1: Years of fossil fuel left as of 2020. Retrieved from [4].

Figure 1.1 shows that based on the annual consumption of 2020 and the proven reserves at that time, oil and gas may be exhausted in as little as 54 and 49 years, respectively. Coal will take longer to exhaust at current consumption levels, it being projected to have sufficient reserves to last for 139 years. However, this projection assumes no change in consumption in these 139 years and should nothing be done, this consumption is certain to rise once oil and

1.1. Fossil fuels

gas have been exhausted.

A further incentive to renewable energy is its availability to all countries, allowing every country to theoretically be self sufficient in energy needs. Recent geopolitical events have shown that reliance on external energy networks can introduce vulnerabilities into local energy markets. An example of such is the recent war between Russia and Ukraine in Europe, which has led to increased volatility in the energy market and price increases [5][6]. As can be seen in Figure 1.2, though prices were already on a steady climb, the events in Ukraine caused a spike to occur [7].



**Figure 1.2:** Displayed are the Brent crude oil price, dutch title transfer facility day-ahead gas price, the Rotterdam coal futures price and the electricity is the weighted average of the five largest electricity markets in Europe. The prices shown here are relative to the price observed on 23 February 2022, where the prices on that date are defined as 100. The grey vertical line denotes the intensification of hostilities in the Ukrainian/Russian conflict. Retrieved from [7].

Shown is that at intensification in the conflict between Ukraine and Russia the energy prices in Europe saw a significant increase. These price increases expose the vulnerability of being dependent on external sources for energy and thus make self sufficient energy sources all the more attractive.

Finally, rising average global temperatures [8][9][10], accompanying the rising  $CO_2$  levels in the atmosphere as shown in Figure 1.3 further incentivizing the implementation of renewable energy sources.

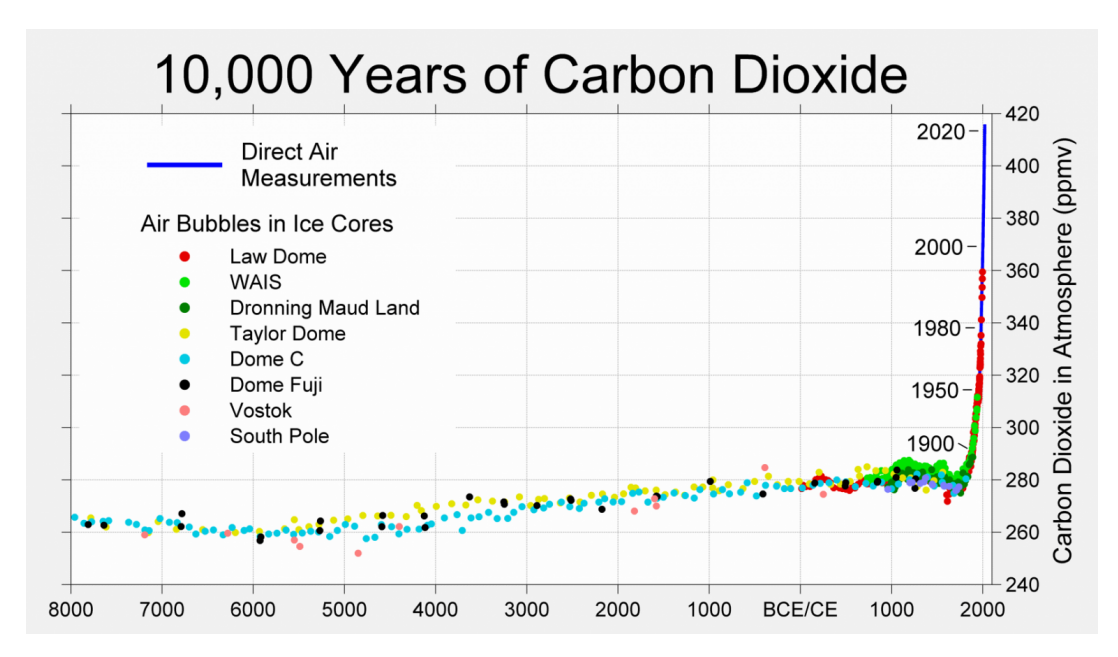


**Figure 1.3:** This figure shows the  $CO_2$  levels from the last 10000 years, obtained through ice cores for older measurements and direct air measurements for the most recent ones. Retrieved on 30-5-2023 from [11].

As seen in Figure 1.3 the  $CO_2$  levels have risen considerably in recent years compared to historic levels.  $CO_2$  is a major greenhouse gas, leading to temperature increases, therefore the emittance of  $CO_2$  into the atmosphere should be curtailed, through for example replacing fossil fueled energy by renewable energy.

#### 1.2. Renewable Energy

The topics introduced in the previous section can be in large part be addressed by the implementation in society of renewable energy technologies, which are functionally inexhaustible and, for solar, wind, freely available to every country. Furthermore, the cost of such technologies is rapidly dropping with photovoltaic (PV) module manufacturing costs dropping by over 90% in the last decade [12]. In addition, the Levelized Cost Of Energy (LCOE), this being the present day cost of the module when considering all the future maintenance costs against the expected lifetime energy yield, has also dropped by 85% [13]. Meanwhile wind energy has seen a decrease of LCOE of 39% between 2010 and 2019 [14]. And with costs expected to continue to decrease for both solar and wind energy [15][16] the economical prospects of renewable technologies look promising. Leading to increasing adoption of such energy sources over the years, which is shown in Figure 1.4 [17].

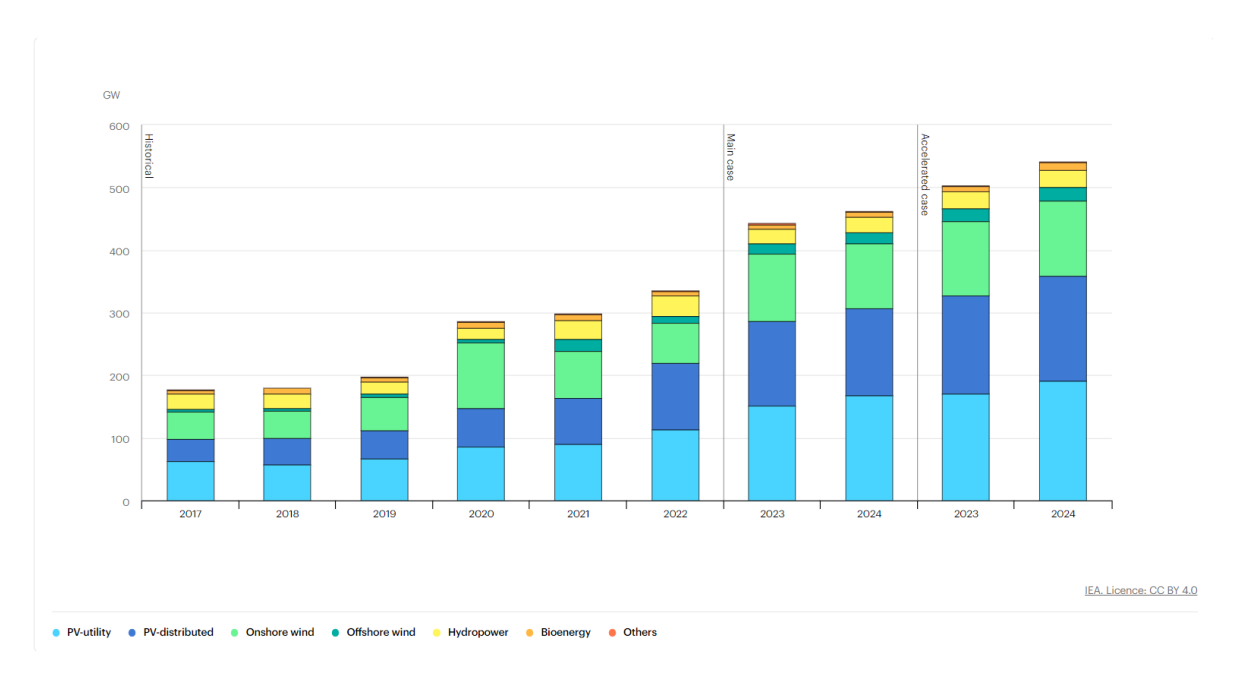


**Figure 1.4:** Given here are the global annual renewable energy growth per source, given in GW. The last four columns represent forecasted energy growth for 2023 and 2024. Retrieved from [17].

Seen in Figure 1.4 are the annual additions to global renewable energy production. On the left of the figure are historical additions and on the right are two predictions of future additions. It can be seen that the amount of renewable energy production added year over year is increasing over time, with the primary contributor to this increase being PV energy.

It is clear that renewable energy is being implemented actively and its rate of implementation is growing. Yet renewable energy is not without downsides. To use PV energy as an example, an issue to be considered is intermittency. This refers to the tendency of the energy source to vary over time. For PV this is caused not only by the day/night cycle and seasonal variation but also by shading, be it from weather conditions or objects covering the panels directly. Figure 1.5 shows an example of this intermittency.

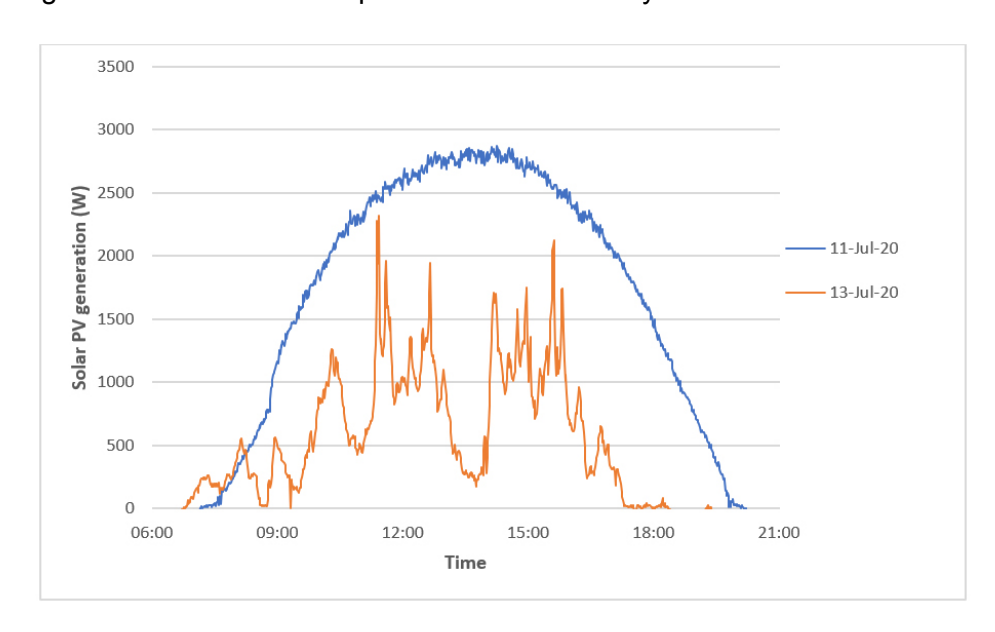


Figure 1.5: Depicted are the generation of the same PV system on two different days. Retrieved from [18].

1.3. Storage 5

Figure 1.5 shows the power generated by a PV system for two different days. The generation on July 13th is lower and less stable than that of July 11th. Corresponding with a day with high cloud coverage and a day with a clear sky. It can be seen in the figure that there is a day/night cycle to PV generation and that weather conditions can influence the generation drastically. This intermittency leads to less stable energy generation, giving consumers less certainty on whether or not there will be sufficient energy to meet demands. Furthermore, on a grid scale supply and demand need to be closely linked and any deviations of such would lead to the grid collapsing. While a surplus of energy is easily solvable by decreasing the production of other sources, a deficit can necessitate grid operators to curtail load by implementing power outages.

#### 1.3. Storage

Thus it is crucial to ensure a stable energy supply and this issue of intermittency must be overcome. This can be done through the implementation of storage technologies. Such technologies allow the generated energy to be used at a later time, when it is needed, thereby improving energy security and allowing for easier maintenance of grid stability. Storage technologies include, but are not limited to, pumped hydro storage, hydrogen storage and battery storage. With each technology operating at differing scales, in terms of both capacity and time. Figure 1.6 shows an overview of various storage technologies.

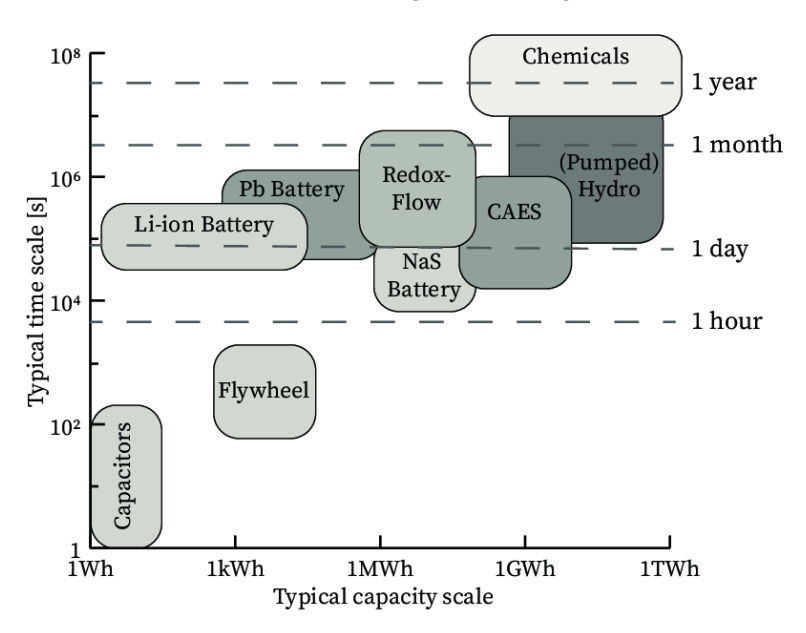


**Figure 1.6:** This figure shows the typical time scale of the most relevant storage technologies as a function of the typical capacity scale. Retrieved from [19].

Figure 1.6 shows that there are several storage technologies. Many of these technologies are needed due to storage demands being varied in capacity and discharge time. However, when considering grid-scale storage as much as 90% of the current global grid-scale energy storage lies in pumped hydro storage [20], with other technologies being far smaller in energy capacity.

Battery storage, however, is beginning to catch up, due to batteries becoming cheaper rapidly. This has caused the viability of using batteries for sub-hourly, hourly and even daily storage to increase, leading to increasing implementation of grid scale battery storage globally. Figure 1.7 displays the cost of Li-ion batteries over time and Figure 1.8 shows the global annual grid scale battery additions.

1.3. Storage 6

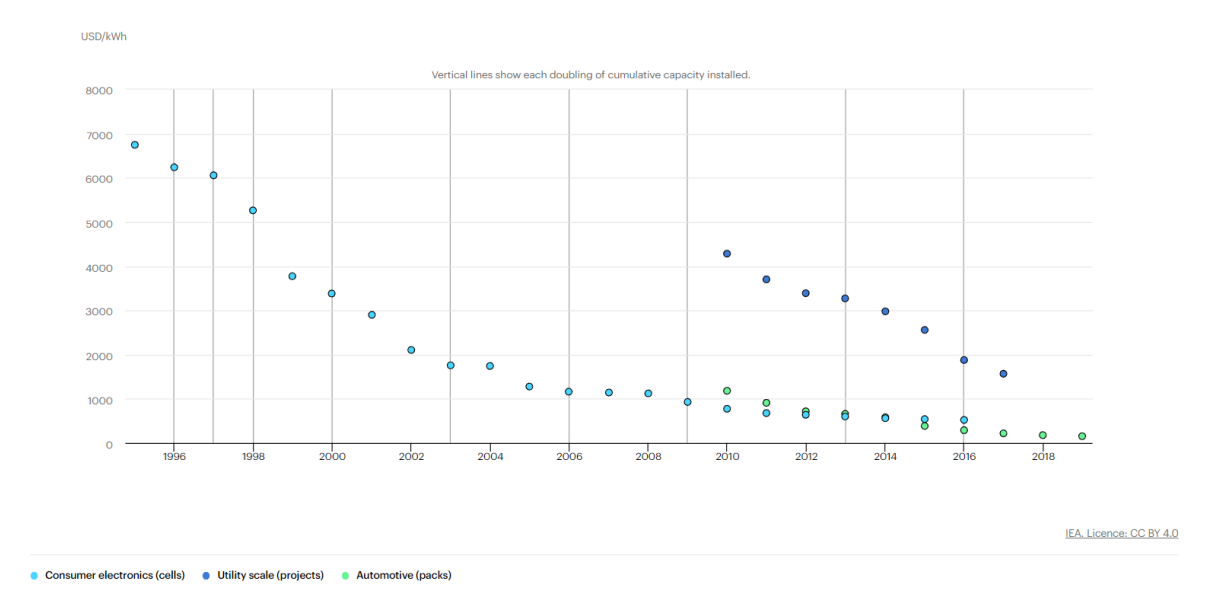


**Figure 1.7:** Displayed are the cost per kWh in USD for three different types of Li-ion battery usage. Vertical lines denote a doubling in global cumulative capacity installed. Retrieved from [21].

Figure 1.7 shows the cost of three types of Li-ion batteries, note the decrease of the cost of each type over time. This decrease in cost allows for greater implementation of batteries in storage solutions.

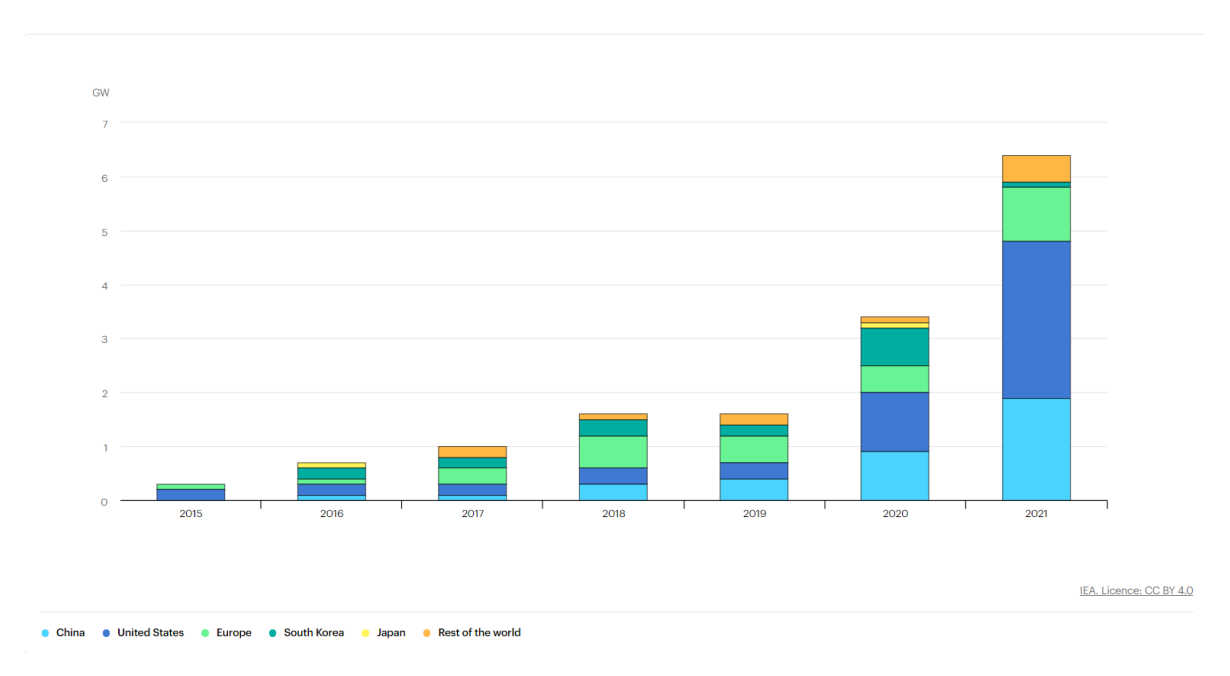


**Figure 1.8:** This figure shows the global yearly growth, in GW, of battery storage for different countries. Retrieved from [20].

Figure 1.8 displays the annual installed battery capacity for a series of countries, seen here is that the rate of installation is increasing, due to the costs decreasing as was shown in Figure 1.7 and countries accelerating efforts to meet climate goals, such as China attempting to be carbon neutral by 2060 [22]. In conclusion, batteries are seen as a critical storage method and will be further elaborated on in Section 1.4.

1.4. Batteries 7

#### 1.4. Batteries

Batteries are a type of electrochemical storage, where electrical energy is converted to chemical energy when stored, and the reverse is carried out when discharged. A battery, consists of three components, these being the anode, the cathode and an electrolyte. The anode and cathode are composed of materials which have the ability of taking in or releasing electrons in what is known as a redox reaction. The electrolyte is present to prevent electron conduction between the two but still allow ionic conduction. The battery functions by being connected to an external circuit, allowing electron flow, with the direction depending determining whether the battery is being charged or discharged. Note, however, that not all reactions are equally reversible. When the reaction within a battery is one direction only and therefore can only be discharged one time, it is known as a primary battery. Meanwhile should a battery be rechargeable, it will be known as a secondary battery.

A popular type of secondary battery is the Li-ion battery. This is a type of battery that uses intercalation of Li<sup>+</sup> ions, that is, moving lithium ions into a host material, as the storage method. There are a variety of host materials which have been used, be it commercially or experimentally, such as cobalt, phosphorus, various metals, alloying anodes (Si, Ge, Sn, etc.), chalcogenides (S, Se, Te), and metal halides (F, Cl, Br, I) [23][24].

Li-ion batteries have the advantage of a high energy density, both gravimetric and volumetric, with commercially available batteries having as high as  $5 \cdot 10^2$  Wh/kg and  $1.4 \cdot 10^3$  Wh/L energy densities [25]. This advantage means the battery is well suited for small-scale applications such as EV's, mobile phones and laptops. Furthermore, the full potential of Li-ion batteries has not yet been achieved and improvement is possible, with experimental batteries having demonstrated capacities as high as  $1 \cdot 10^3$  Wh/kg [26].

Li-ion batteries are not without disadvantages however. The main disadvantage is the scarcity of lithium, where the crust of the earth only contains approximately 20 ppm, meanwhile sea water contains even less at 0.17 ppm [27]. Furthermore, high concentrations are only found in some countries including, but not limited to, Australia, Chile, Bolivia, Argentina, the United States and China [28]. It is these countries which have access to lithium in high concentrations and quantities, which in turn implies geopolitical dependence. For this reason, an alternative material with which a battery can be made is of interest. One such group of alternatives lie in the metal-air batteries, which will be discussed in Section 1.5.

#### 1.5. Metal-air batteries

Metal-air batteries when compared to Li-ion batteries are advantageous in terms of scarcity, this subset of batteries consist out of a metal anode and a porous cathode, such as carbon. The reactive element, however, is not carbon, but oxygen, hence the name of this type of battery. Metal-air batteries have been demonstrated using a variety of metals, such as aluminium, magnesium, zinc, sodium and even lithium itself [29]. Each of these metals has high theoretical energy densities [30], allowing for similar use cases in theory. In addition, certain metal-air batteries, such as Li-air, Zn-air or even K-air show promise as secondary batteries [31][32]. Finally, metals such as aluminium and sodium are far more abundant than lithium and therefore bypass the scarcity disadvantage.

Within this subset of batteries lies the silicon-air battery, which is of interest due to two factors. First the components of this battery, silicon and oxygen, are the two most abundant elements in earth's continental crust [33]. Furthermore, Si-air batteries theoretically have an

extremely high volumetric energy density at nearly  $1 \cdot 10^4$  Wh/kg [34][29]. These advantages, however, come paired with challenges which face the design and implementation of such batteries.

To understand the challenges first some background on Si-air batteries must be known. A working example of this battery has been demonstrated using two different electrolytes, KOH [35] and a Room Temperature Ionic Liquid (RTIL) 1-ethyl-3-methylimidazolium fluorohydrogenates (EMIm(HF)<sub>2,3</sub>F) [36]. The chemical reaction governing the battery discharge is not the same when considering the two different electrolytes, however, they have a commonality in that silicon is being consumed to fuel the reaction. Where in both cases a byproduct is generated, SiO<sub>2</sub>, which is a highly resistive oxide and therefore its build up can prevent the battery from fully discharging. Furthermore, both electrolytes react with silicon itself in a parasitic corrosion reaction even when not discharging. This has as consequence that the efficiency is greatly lowered. Experimental results show efficiencies no higher than 6% for KOH [37] and 10% for the RTIL [38]. Therefore, finding alternative electrolytes that do not exhibit this parasitic reaction are of interest. This report, is focused on one such potential alternative, namely 1-butyl-1-methylpyrrolidinium bis(trifluoromethyl-sulfonyl)imide (BMPyr[NTf<sub>2</sub>]). This RTIL is of interest due to its previous usage in a zinc-air battery [39], where variation in discharge potential was observed when mixing the RTIL with water. A potential disadvantage of this RTIL is the low potential it exhibited during its usage in the Zinc-air battery. This lower potential may be caused by the RTIL having a lower conductivity when compared to KOH and EMIm(HF)<sub>2.3</sub>F.

#### 1.6. Thesis objective

The objective of this thesis is to experimentally record discharge characteristics of a silicon-air battery using BMPyr[NTf<sub>2</sub>] mixed with varying amounts of water as the electrolyte, focusing on the conductivity. The aim is to determine whether or not the conductivity has a large role in determining the potential of the battery during discharge.

In this thesis the results of experiments will be presented on the application of BMPyr[NTf2] in Si-air batteries. Specifically, the background of Si-air batteries will be explored in Chapter 2 where battery mechanics will be looked at, the components of the Si-air battery will be studied and alternative electrolytes will be looked at. Next in Chapter 3 the experimental method will be shown. In Chapters 4 and 5 the results to the experiments mentioned in the previous chapter will be given and discussed. Finally, a conclusion and an answer to the question posed will be given in Chapter 6.

## Si-air Batteries

In this chapter the theory behind Si-air batteries will be explored, first in Section 2.1 some background information regarding batteries will be provided, next in Section 2.2 metal-air batteries will be covered, a category of batteries to which Si-air batteries belong to. Afterwards in Sections 2.3, 2.4, 2.5 the battery components will be discussed, these being the anode, cathode and electrolyte, respectively. Finally Section 2.6 have a short overview of a different type of Si fueled battery which shows the potential of being rechargeable.

#### 2.1. Foundations of battery operation

Batteries work by converting chemical energy into electrical energy, during discharge and vice-versa during charging. This is done through a redox reaction, which most simply seen is a reaction between two species where an electron is transferred. Naturally, there is complexity regarding which species are involved, whether the reaction is reversible and how many electrons are transferred. In a battery this concept is applied through the usage of an anode, a cathode, and an electrolyte. Where the anode and cathode represent the two species involved in a typical redox reaction and the electrolyte a material facilitating ionic transport. The electrons are transported externally through for example wires, completing the circuit and allowing a battery to discharge or charge. Further details regarding the redox reaction, how the battery potential is determined, what causes the potential and the inescapable losses are in the following subsections.

#### 2.1.1. Red-Ox Reactions

As was mentioned previously, a redox reaction is where two species interact through exchanging electrons. In batteries this is done through having half of the reaction occuring at each electrode. Previously written were the terms anode and cathode, these terms signify the electrode that is releasing electrons and the one that is accepting electrons, respectively. It is important to note that which of the two electrodes is which depends on the state of the battery, namely whether it is charging or discharging.

At the anode an oxidation reaction releases electrons, and these electrons will accumulate at the anode, making it more negative with respect to the cathode. Inversely, a reduction reaction occurs at the cathode by accepts electrons, leading to a decrease in electron concentration at the cathode, making it more positive relatively. This difference in charge causes a flow of electrons between the two electrodes, should the battery be connected to an external circuit allowing this. Meanwhile, the two electrodes are separated by an electrolyte, which facilitates the transfer of ions between the two electrodes to compensate for the moving electrons.

Finally, the elements mentioned previously will together make a battery. It is important to note that the energy produced by a battery comes from the potential difference between the components, yet the potential of a single component cannot be accurately measured by itself, thus a work around is used. Namely, the usage of hydrogen as a reference electrode, or the Standard Hydrogen Electrode (SHE) as given in Equation 2.1:

$$H_2 \rightarrow 2H^+ + 2e^-(E = 0.00 \text{ V})$$
 (2.1)

In this reaction an hydrogen atom is split into two  $H^+$  ions and two electrons, by definition having a potential of 0.00 V at all temperatures [40]. This way, should an electrode material be likelier to donate electrons than the SHE, thus leading to a more negative potential, that material will be called the anode. Inversely, should an electrode material be more willing to accept electrons than the SHE, thus leading to a more positive potential, that material will be called the cathode. The battery potential is defined by Equation 2.2:

$$E^0 = E^c - E^a (2.2)$$

Where  $E^0$  is the battery potential,  $E^c$  is the cathode potential and  $E^a$  is the anode potential, in reference to the SHE.

#### 2.1.2. Working Principle

Of course, not all materials are suitable for usage in a redox reaction. Part of the research into better and cheaper batteries in the modern day is to find novel materials or combination of materials which are suitable after all.

It is the Gibbs free energy G which is effectively the chemical energy stored within a closed system, equalling the maximum work which can be derived from said system, assuming temperature and pressure are kept constant [40]. However, rarely is it that all the chemical energy in a system is used in a single reaction, instead more interestingly is  $\Delta G$  that represents a change in the Gibbs free energy when the previously mentioned system undergoes a state transition. Each half of the redox reaction is such a transition and therefore has a corresponding  $\Delta G$ . By definition a positive  $\Delta G$  means energy must be supplied for the transition to take place, and as such must be driven by some outside force. Meanwhile a negative  $\Delta G$  implies that the reaction releases energy, and as such could occur spontaneously. Thus if  $\Delta G$  is zero, neither energy is needed nor is gained and as such the system is in thermal equilibrium [40].

For a battery to be functional, the  $\Delta G$  must be non-zero. A discharging battery has a negative  $\Delta G$ , meaning there is energy being released by the reaction occurring inside the battery. This relates the  $\Delta G$  to the battery potential  $E^0$  through Equation 2.3

$$\Delta G = -nFE^0 \tag{2.3}$$

where n is the number of electrons involved in the reaction and F the Faraday constant which is defined as  $96485 \text{ C mol}^{-1}$ .

Finally, the relation between Gibbs free energy and battery potential as given only holds if the concentrations of every substance involved in the reaction is equal. If that is not the case, the battery potential can be calculated via the Nernst equation [41], as given below.

$$E = E^0 - \frac{RT}{nF} \ln(Q) \tag{2.4}$$

where R is the molar gas constant, defined as 8.3145 J K<sup>-1</sup> mol<sup>-1</sup>, T the temperature and Q the reaction quotient, which depends on the reaction in question according to Equation 2.5

$$Q = \frac{(a_C)^{\gamma} (a_D)^{\delta}}{(a_A)^{\alpha} (a_B)^{\beta}} \quad ; \quad \alpha A + \beta B \to \gamma C + \delta D$$
 (2.5)

where  $a_x$  denotes concentration per material,  $\alpha, \beta, \gamma$  and  $\delta$  denote the quantity of each material present per reaction. Notably solids and water are ignored in this equation, so if they are present in the reaction, their segment  $(a_x)^y$  may be set as 1.

#### 2.1.3. Overpotentials

So far the battery potential has been viewed entirely theoretically and the method which is used to calculate it does not take any losses into account. In reality this is not the case and there may be many different reasons why the practical potential of a battery differs from the theoretical potential as described by Equation 2.4. These losses are called overpotentials and are divided into three categories, namely activation overpotential, concentration overpotential and ohmic overpotential.

#### **Activation Overpotential**

The activation overpotential is related to the activation barrier of the reaction of interest. It is the energy required to break chemical bonds, if they are present, prior to starting the chemical reaction. The activation overpotential can be determined depending on the electron transfer coefficient, the exchange current density, the current at the electrode and the temperature. This relationship is known as the Butler-Volmer equation [42] where the overpotential is increased as the current is increased. Inversely this overpotential is negligible for smaller currents, as can be seen in Figure 2.1, which shows an example of this relationship [42].

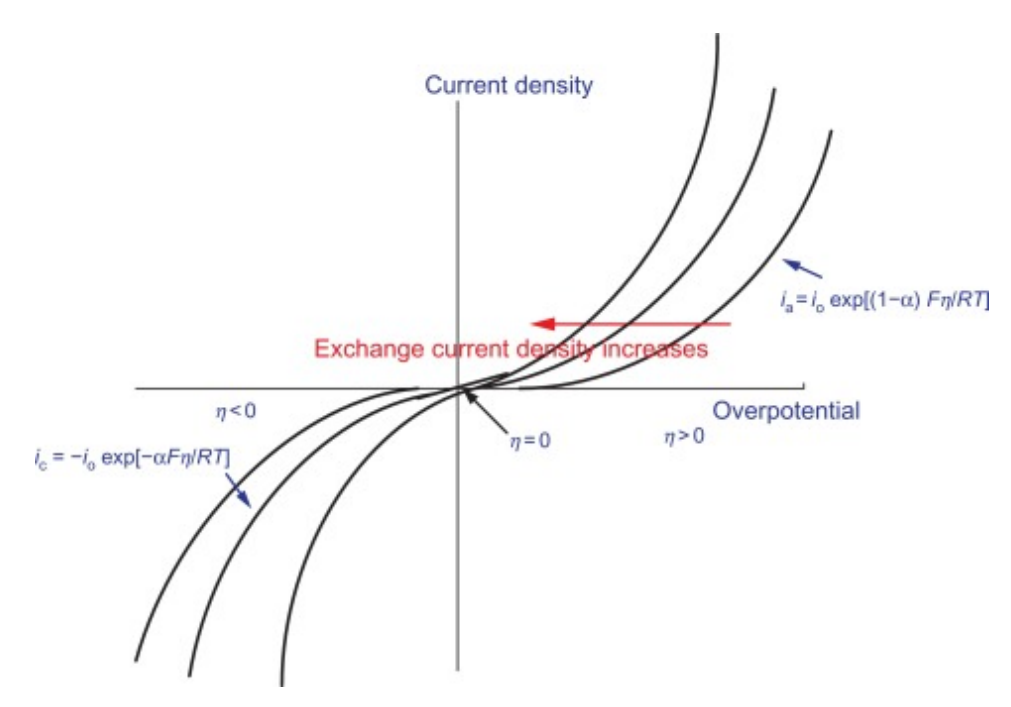


Figure 2.1: An example of the Butler-Volmer equation.

#### **Concentration Overpotential**

The concentration overpotential refers to the losses caused by a deficit in mass transport, in which case the battery experiences a slowed reaction leading to lower potential. This slowed

reaction can be either due to insufficient reactants being able to reach the reaction site or the reaction products accumulating at the reaction site and thus blocking off further reactions. This overpotential is linked by the current density of the battery, given that a higher current density implies a faster reaction, assuming the same materials are used, and thus a higher requirement in terms of mass transport. The mass transport in bulk electrolyte may be calculated using the Nernst-Planck equation [43].

#### Ohmic Overpotential

The ohmic overpotential as the name suggests is governed by ohm's law [44]. Where the overpotential is found according to  $\eta_{\text{ohmic}}=iR$ , meaning higher current would lead to higher overpotentials. The resistance can originate from any part of the battery, be it the electrolyte, electrodes or the current collector.

Previously it has been established that there are three categories of overpotentials and these three overpotentials together represent the losses a battery will experience. Each overpotential grows differently as per the previous subsections and as such the dominating overpotential changes depending on the battery materials and the current at which it is charged/discharged. Aside of the losses the reaction rate within the battery also is related to the overpotentials, where a dominating overpotential can become the rate-limiting step of a reaction, forcing the reaction to slow down.

#### 2.2. Metal-air batteries

Having considered batteries in general, now the focus will be put upon a subset of batteries known as metal-air batteries. Which has anode materials such as zinc, aluminium, iron and lithium. This type of battery has been of interest due to the high theoretical capacity as seen in Figure 2.2 [34]

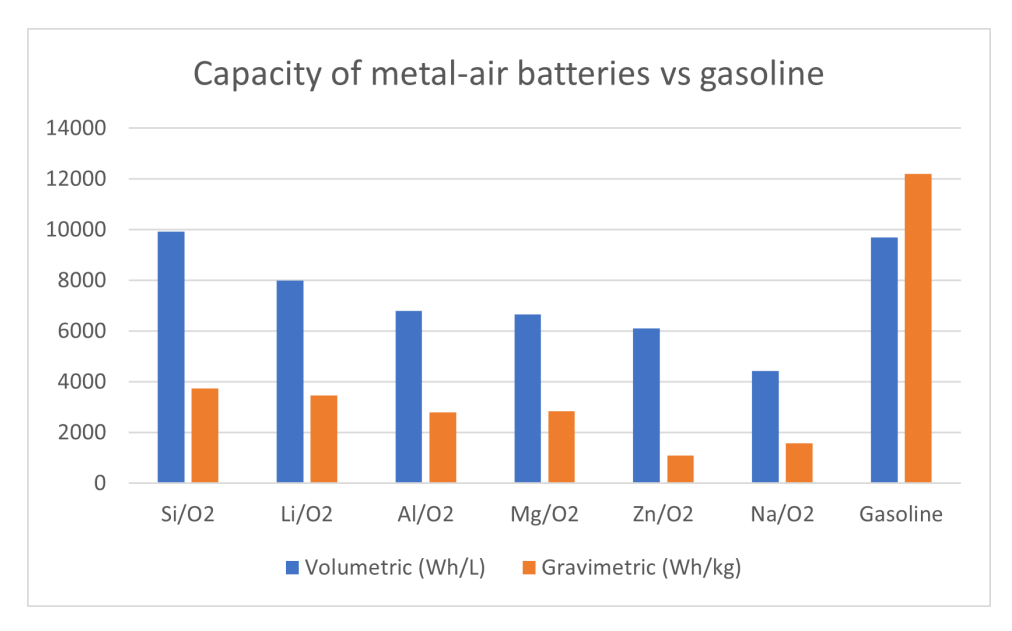


**Figure 2.2:** The theoretical gravimetric and volumetric capacities of a selected few metal-air pairs and gasoline. Adapted from [34].

Visible in Figure 2.2 are the volumetric and gravimetric energy densities of a series of metal-air batteries, with those using materials such as Si, Li and Al having comparable volumetric energy density to gasoline. This makes this type of battery promising in terms of energy density.

2.3. Anode 13

As with all batteries, this type too works through red-ox reactions, which convert chemical energy into electrical energy through an oxidation and reduction reaction pair at the two electrodes which make up a battery. For metal-air batteries, one of the electrodes is oxygen, the other electrode is one of the previously mentioned metals. With this established, of further importance is the distinction of battery class, namely whether it is a primary or a secondary battery. Primary batteries being single use batteries which have an irreversible charge, secondary batteries in contrast work via a reversible reaction and can in principle be reused. Research into metal-air batteries has yielded good results, allowing for the commercial viability of Zn-air batteries as early as in 1930 [45], however this viability only holds for its implementation as a primary battery, attempts at creating a viable secondary battery has not had commercial success due to low cyclability [32]. Similar research into secondary batteries for the Li-air pair has also been executed by Jiang and Abraham [46]. However these two metal-air pairs still possesses weaknesses which the next pair and the focus of this report hopes to address. This pair being the Si-air battery, which in comparison to the Zn-air pair has a much higher gravimetric and volumetric energy density. Secondly the Si-air pair is far more abundantly available in the world compared to the Li-air pair which requires lithium. As can be seen in Figure 2.3 where Si is more than a hundred thousand times as abundant as Li [47].

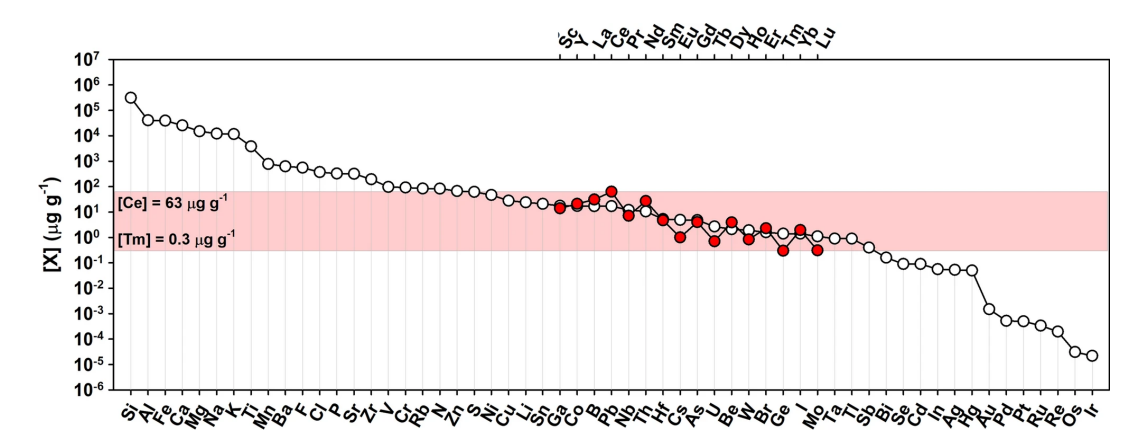


**Figure 2.3:** Presence of elements inside the earth's crust given in microgram per gram given in log scale. Retrieved from [47].

Si-air batteries have multiple options to choose when selecting an electrolyte, these being the aqueous and non-aqueous electrolytes of which examples are Room Temperature Ionic Liquids (RTIL) and KOH, respectively. Lastly a solid state gel is also a possibility. Nonetheless, no secondary Si-air battery has been demonstrated at room temperature as of yet and of the primary batteries which have been made, none show comparable efficiency to modern batteries, much work must still be done for this type of battery to be viable.

This report aims to further explore this Si-air pair through examining the operation of such a battery using a yet untested RTIL as electrolyte. To do so the next three sections will cover the components of such a battery.

#### 2.3. Anode

First the anode of the Si-air battery shall be discussed. Initial experiments used a <100> mono-crystalline silicon wafer, with heavy n doping using As [36]. This type of anode has seen use in later studies, in both the <100> and <111> orientations [35][37]. Additionally, an experiment was done to study the battery behaviour when using a non-uniformly doped <100>

2.4. Cathode

mono-crystalline wafer, as opposed to the prior uniformly doped wafers [48].

Though initial studies used mono-crystalline Si wafers, later studies branched out into using modified silicon wafers, such as adding silicon nano-wires on top of the <100> wafers [49]. This has as result an increase in discharge time and discharge voltage, presumed to be due to the increased reaction area, which are advantageous in two manners, a decrease in the speed in which  ${\rm SiO}_2$  accumulates upon the surface and an increase in the  ${\rm Si(OH)_4}$  dissolve rate.

In every experiment, a constant remains however, the usage of a metal back contact, this is due to silicon by itself not being very conductive, therefore a metal back contact is used as a current collector.

#### 2.4. Cathode

The cathode of the silicon air battery can be taken from its name, namely the active component is air. Naturally, the battery cannot simply have exposure to the open air without some level of containment. The degree and scope of this containment is what matters for the design of this type of battery. In studies the usage of a porous carbon based cathode was prevalent [37][35][36]. This cathode can be divided into three layers as shown in Figure 2.4

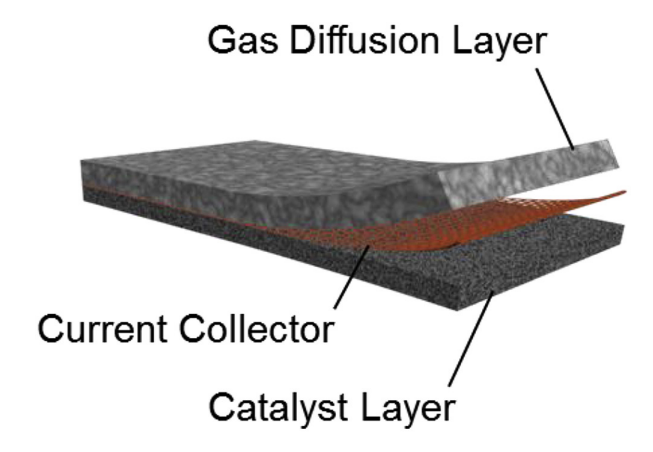


**Figure 2.4:** Air cathode which comprises of three distinct layers, the gas diffusion, current collector and catalyst layers. Taken from [50]

where the three layers can be seen, this design was first used in 1932 to build Zn-air batteries, but has seen continued use till the modern day [51]. Some properties are desired of the cathode, namely that it must be permeable to oxygen as this is needed for the battery to discharge, yet it must not be permeable to the electrolyte as else there will be leakage. This is a careful balancing act as to prevent leakage the pores must be made hydrophobic using agents such as polytetrafluoroethylene (PTFE), polyvinylidene fluoride (PVDF), and fluorinated ethylene propylene (FEP) [52][53]. Yet this causes a decrease in oxygen diffusion and as such too much of such hydrophobic agents would impact battery performance [54]. The optimal wt% is variable per battery design as the electrolyte permeability can differ, however an estimate has been made that optimally it will range between 30-70 wt%[50].

In contrast to the diffusion layer, the current collector layer is chosen on basis of economic benefit as outside of the necessity of the collector being oxygen permeable as well, there are many options for both the material as well as the design and thus the most economically viable is to be chosen [50].

Next covered is the catalyst layer, here the reaction takes place and as such a proper catalyst is required, one which positively impacts the desired reaction. Traditionally noble metals, such as platinum, have been used [55] however this is not ideal as such catalysts are expensive. For the Si-air battery an alternative catalyst in the form of  $MnO_2$  was used [37].

Finally, a study has suggested that pre-wetting the cathode when used in conjunction with KOH as electrolyte could lead to improved discharge potential [56]. It was found that applying a pre-treatment to the cathode with 30% KOH would lead to increased discharge time and discharge potential, with results showing a potential increase from 0.7-0.8 V to 1-1.2V and discharge time increasing from seconds to 71 hours at the higher end. The highest value for both the discharge time and potential was found for a pre-wetting time of 8 hours [56].

#### 2.5. Electrolyte

The last component of this battery to be discussed is the electrolyte, for the Si-air battery two types of electrolyte will be discussed here, first an aqueous electrolyte, in this case KOH and secondly a non-aqueous electrolyte, where in literature the RTIL  $EMIm(HF)_{2.3}F$  has been used. However further information regarding RTIL's in general is also provided here.

#### 2.5.1. Aqueous

A Si-air battery using KOH was first demonstrated by X.Zhong et al. [35]. Where they used the discharge process as given in Equation 2.6 [57]

$$Si + O_2 + 2H_2O \rightarrow Si(OH)_4 (E_0 = 2.09 V)$$
 (2.6)

consisting of the anode and cathode reactions given in Equations 2.7 and 2.8

Anode: 
$$Si + 4OH^- \rightarrow Si(OH)_4 + 4e^- (E_0 = 1.69 \text{ V})$$
 (2.7)

Cathode : 
$$O_2 + 2H_2O + 4e^- \rightarrow 4OH^- (E_0 = 0.4 \text{ V})$$
 (2.8)

At the anode Si reacts with  $4OH^-$  and produces  $Si(OH)_4$  and 4 electrons, meanwhile at the cathode oxygen is reduced into  $OH^-$ . The anode and cathode reactions together lead to a standard potential of +2.09V [48].

In an ideal scenario the produced  $Si(OH)_4$  would remain inert and simply build up in the electrolyte, however this is not what occurs. Instead a passivation reaction occurs where the  $Si(OH)_4$  is broken down, as seen in Equation 2.9

$$Si(OH)_4 \rightarrow SiO_2 + 2H_2O \tag{2.9}$$

This reaction creates water and  $SiO_2$ , said  $SiO_2$  is what passivates the battery, as the oxide will be deposited on the surface of the silicon anode, leading to the formation of an oxide layer. As  $SiO_2$  is highly resistive, this layer will halt the discharge of the battery.

The main advantage of using KOH is its capability to dissolve  $Si(OH)_4$  when in sufficient concentration, this means that in theory the passivation mechanism at the Si electrode is self regulated. Furthermore, KOH can even remove any existing native oxide layer as it is capable of dissolving  $SiO_2$  at a rate of 3.4 nm/hour at 6.6M concentration [58]. However, though KOH can prevent the formation of a passivation layer and remove any that is present, it also parasitically corrodes the Si anode directly [48][35]. As such a major disadvantage when using

KOH as electrolyte is the parasitic corrosion of the Si anode, where the rate at which this parasitic corrosion occurs influenced by both the concentration of the KOH and the temperature at which it is occurring. This is problematic as a high KOH concentration is needed to prevent passivation. This parasitic corrosion reaction is given by Reaction 2.10 [59]:

$$Si + 2OH^{-} + 2H_{2}O \rightarrow SiO_{2}(OH)_{2}^{-2} + 2H_{2}$$
 (2.10)

where the Si reacts with  $OH^-$  and water to form silicates and hydrogen gas, this reaction lowers the efficiency of the cell and as such is not desired. At room temperature using 6.6M KOH parasitic corrosion rates between 1.25 and 2.2  $\mu$ m per hour have been reported [48][60].

In attempts to increase the efficiency of the Si-air battery the concentration of KOH has been varied in experiments finding that increasing the concentration leads to higher open circuit potentials, of 1.1 V at 0.6M to 1.32 V at 6M [35]. Though increasing the concentration also enhances the parasitic corrosion effects of the electrolyte up to a maximum at approximately 6M [37]. As such the longevity of the Si-air battery using KOH comes at the cost of a lowered discharge voltage and vice versa [60].

Furthermore, the conductivity of KOH changes based on the concentration which also influences the potential, shown next is Figure 2.5 representing this change in conductivity, the figure also shows a fitted curve representing the conductivity according to an equation given after the figure.

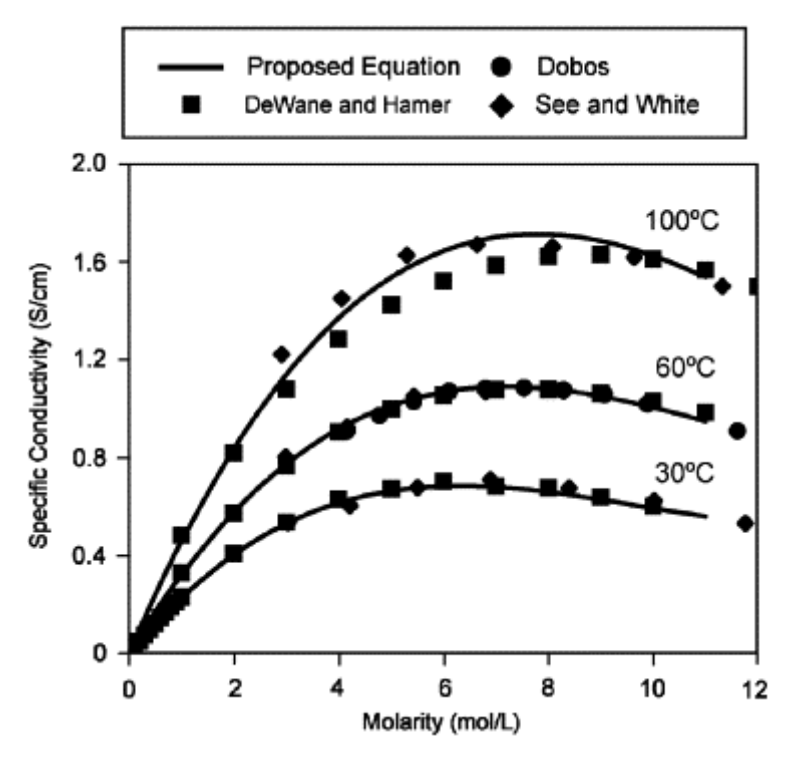


**Figure 2.5:** Conductivity of KOH at various temperatures from a series of sources. Through each of the data points there is a curve plotted approximating the conductivity according to an equation. Retrieved from and compiled by.[61]

Seen in the figure is that the conductivity of KOH appears to reach a maximum for room at approximately 6M for a temperature of 30 degrees Celsius. Further it is seen that with increasing temperature this maximum is reached at higher and higher molarities. This relationship

between concentration and conductivity is obtained through the following equation:

$$\kappa = AM + BM^2 + CMT + D\frac{M}{T} + EM^3 + FM^2T^2$$
 (2.11)

where A,B,C,D,E and F are all constants with values of -2.041, -0.0028, 0.005332, 207.2, 0.001043 and -0.0000003, respectively. M is the molarity, T is the temperature in Kelvin and  $\kappa$  is the conductivity in S/cm.[61] Of note is that this equation is a fit to experimental measurements of the conductivity, and as such the dimensions of both sides do not necessarily match up. Furthermore, the fit was created using molarities of 0 to 12M and temperatures between 0 and 273.15 and 373.15 Kelvin. As such outside of these ranges the equation becomes highly unreliable.

#### 2.5.2. Non-Aqueous

RTIL's are a broad group of chemicals having differing characteristics, which individually or collectively in groups make RTIL's useful for different purposes. For example two RTIL's named bmimPF<sub>6</sub> and bmimCl are used for their wetting capability and viscosity during gas chromatography [62]. In the same vein RTIL's exist that are used in water splitting, wood industries, solar photo and thermal conversion and even as paint additives [63]. With such a broad range of applications and characteristics, however, it becomes important to determine how the characteristics of an RTIL are developed and which of these are important when designing a battery.

RTIL's are composed of a cation and an anion, of which the cation determines the physical properties such as density, melting point, vapour pressure and viscosity, meanwhile the anion determines the reactive properties of the RTIL [64]. For the function of a Si-air battery it is important that the RTIL facilitates the redox reaction, as such any chosen RTIL should have an anion which permits this. Furthermore, as the electrolyte will be exposed to the open air, ideally the RTIL should have high stability in such an environment. Finally the RTIL should have a high conductivity, this to prevent the transport of ions inside the RTIL from being a rate-limiting step.

The first published work regarding Si-air batteries used the RTIL EMIm(HF)<sub>2.3</sub>F as electrolyte [36]. This RTIL was chosen due to its high conductivity at 100 mS cm $^{-1}$ , low viscosity and chemical stability in air. The reactions occurring when using EMIm(HF)<sub>2.3</sub>F are given below, where first the reaction at the anode side is shown.

$$Si + 12(HF)_2F^- \rightarrow SiF_4 + 8(HF)_3F^- + 4e^-$$
 (2.12)

here the Si reacts with 12 dihydrogen-fluoride anions, forming SiF<sub>4</sub>, notably one of the reactants and one of the products,  $(HF)_2F^-$  and  $(HF)_3F^-$  are already present in the RTIL, the liquid is composed of a 70/30 mixture of the di- and tri-hydrogenated fluoride anions [38].

Next the reaction at the cathode is given, there are in fact two reactions which occur at the cathode.

$$O_2 + 12(HF)_3F^- + 4e^- \rightarrow 2H_2O + 16(HF)_2F^-$$
 (2.13)

This reaction describes the reduction of oxygen at the cathode, resulting in the formation of water. Next the presence of water facilitates the final reaction which occurs, as shown next.

$$SiF_4 + 2H_2O + 4(HF)_2F^- \rightarrow SiO_2 + 4(HF)_3F^-$$
 (2.14)

Where  $SiF_4$ , created at the anode, reacts with water and  $(HF)_2F^-$ to create  $SiO_2$  and  $(HF)_3F^-$ . Given that all these reactions either use or produce  $(HF)_2F^-$  and  $(HF)_3F^-$ , a final reaction

can be found which combines Equations 2.12,2.13 and 2.14 which describes the discharge process.

$$Si + O_2 \rightarrow SiO_2 \tag{2.15}$$

Here it is seen that the discharge process ultimately creates  $SiO_2$ , which itself is not further used in any other reactions.

This accumulation of  $SiO_2$  is the main challenge of using  $EMIm(HF)_{2.3}F$ , as due to this the pores which allow air flow into the battery at the cathode side will get clogged, thereby limiting the discharge capacity of the battery. The mechanism by which the pores are clogged differ depending on the discharge current, where the  $SiO_2$  particles size is proportional to the discharge current. The clogging is shown schematically in Figure 2.6.

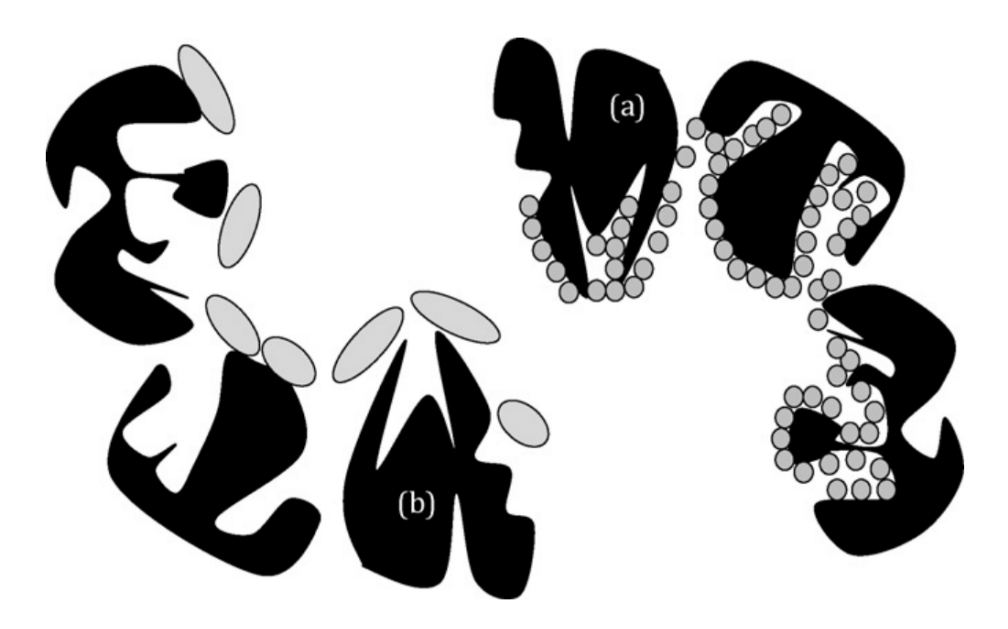


Figure 2.6: Here is shown in a) the clogging mechanism at low discharge current and in b) the mechanism at high current. Retrieved from [38]

Here is seen that the precise manner in which the airflow gets restricted differs slightly, as with low discharge currents the pores become clogged, but with high discharge currents the pores instead are blocked off. However, the ultimate result is the same: a cessation of the discharge reaction due to insufficient oxygen. Studies have found that mixing the RTIL with water can partially mitigate this issue by causing Reaction 2.14 to occur in the bulk of the electrolyte as opposed to the surface of the cathode [65]. With results suggesting that addition of 15% water increases the discharge capacity by as much as 40%. But increasing the water fraction even further leads to a rapid decline in discharge capacity with a 30% water addition resulting in a 50% decrease in capacity [65]. Seemingly adding water beyond 15% causes the formation of a resistive oxide at the anode surface [48]. Compared to KOH, however, EMIm(HF)<sub>2.3</sub>Fhas the advantage of relatively low parasitic corrosion to the Si anode, with a heavily n-type doped anode showing as little as 0.08 nm/min [36][38]. Only a fraction of even the lower reported value for KOH electrolyte, at 1.25  $\mu$ m/hour. Of note is that heavily p-type doped silicon shows even lower parasitic corrosion rates, of <0.01 nm/min however such silicon anodes also show lower potential [36].

Though EMIm(HF) $_{2.3}$ Fis a suitable electrolyte, it still offers some challenges as mentioned previously. Therefore this report will attempt to explore using different RTIL's as the electrolyte.

To do so three classes of alternative RTIL's are viewed.

Firstly RTIL's which have anions that are already proven to work, this means RTIL's
which have (HF)<sub>3</sub>F<sup>-</sup> and (HF)<sub>2</sub>F<sup>-</sup> anions are hypothesized to react in a similar manner
to EMIm(HF)<sub>2,3</sub>F.

- Secondly RTIL's that have similar anions, meaning in the form of  $(HF)_xF^-$ .
- And finally RTIL's which have an entirely different anion.

#### Same anions

Starting with the same anions, examples of such an RTIL are  $Cs(FH)_{2.3}F$  and  $DMIm(FH)_{2.3}F$  [66] [67], which have similarly high conductivity at 86.3 and 110 mS cm<sup>-1</sup>, respectively. Such RTIL's may be good candidates as alternatives for usage in Si-air batteries and determining which one to use could be done based on their respective conductivities. The hypothesis here is that the battery using a RTIL with the same anion will discharge in a similar manner and exhibit a similar potential to a battery using  $EMIm(HF)_{2.3}F$ , accounting for any differences caused by increased or decreased conductivity. Should however these alternatives be unavailable due to economic reasons or difficulty of manufacturing, the next option would be to find RTIL's which have a similar anion structure.

#### Similar anions

The second method of finding alternative's is looking for RTIL's having an anion in the form of  $(HF)_xF^-$ , with examples of such  $(CH_3)_4N(HF)_nF$  with n between 3 and 5 [68]. This set of RTIL's have a possibility of being viable due to the presence of the HF groups which react with the electrodes in a Si-air set up. Furthermore, for n=4 this RTIL has a very high conductivity at 197.6 mS cm $^{-1}$  [68]. Similar to the case of the same anions, the selection of which RTIL to use would come down to the conductivity, though here preference could be given to those RTIL's which have the most similar anion. The hypothesis here is that the battery potential will be different due to a different chemical reaction, through the high likelihood that the discharge reaction will be different. However, there are still HF groups present which were the primary reactants when using EMIm(HF) $_{2.3}$ Fand it is due to the presence of these HF groups that it is hypothesized a viable battery cell can be made.

#### Different anions

Using different anions introduces a new problem, as using RTIL's with untested anions have no guarantee of producing a viable battery. The number of available RTIL's is large, but a narrowing of possibilities can be made by only testing those RTIL's that have an acceptable conductivity, of at least 1 mS/cm, and ease of access. As it is yet unknown whether or not a viable battery will be created using this set of RTIL's, it is advantageous to start with those which easiest to obtain. Two readily available RTIL's are 1-butyl-1-methylpyrrolidinium bis(trifluoromethyl-sulfonyl)imide (BMPyr[NTf2]) and 1-butyl-3-methylimidazolium bis(trifluoromethylsulfonyl)imide (BMIm[NTf2]), proposed by J.Nithin [69]. Unfortunately these two RTIL's have lower conductivity than EMIm(HF)2.3Fat room temperature, approximately 3 and 4 mS cm<sup>-1</sup>, respectively [70] as such should this alternate RTIL be viable it is expected that greater resistive losses would be experienced.

Nonetheless, BMIm[NTf<sub>2</sub>] has seen usage in electrodeposition of Si [71] meaning the RTIL shows the capability of interacting with silicon. Furthermore, BMPyr[NTf<sub>2</sub>] has been used in a Zn-air battery pair, showing that there is potential for this RTIL for usage in metal-air batteries [39]. Shown also in the paper is a hypothesised reaction behaviour for the Zn-air pair, shown in Figure 2.7.

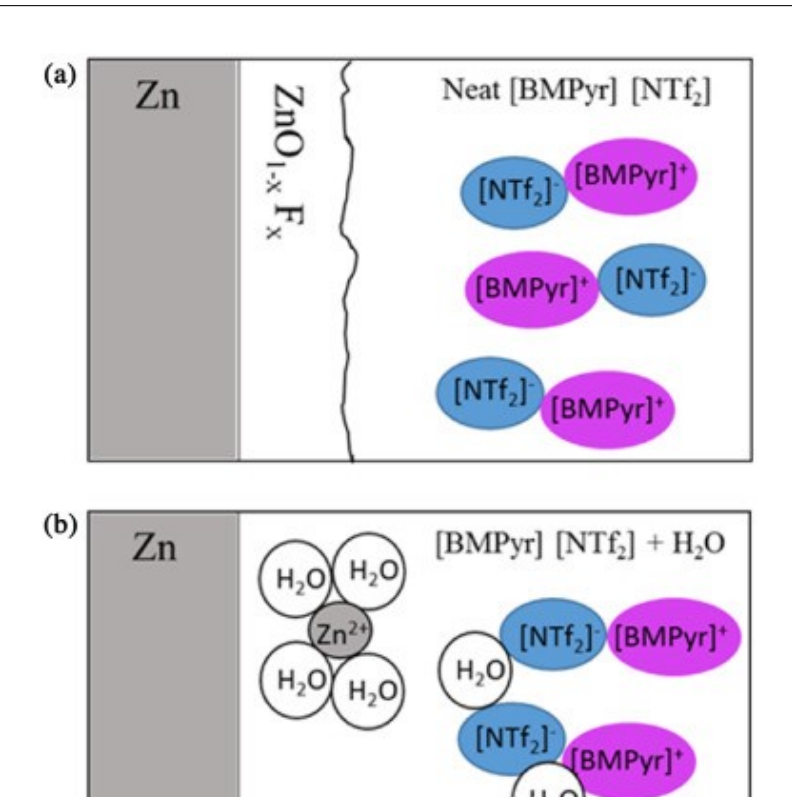


**Figure 2.7:** Depicted in (a) is a proposed surface reaction of the Zn-air battery pair when using pristine BMPyr[NTf<sub>2</sub>], where the formation of a surface layer occurs. In (b) is shown the proposed reaction when water is introduced, acting as a transport for the zinc ions, preventing the formation of this layer. Figure adapted from [39].

[BMPyr]+

Seen in part (a) of this figure is a possible reaction mechanism for the Zn-air pair. Where using pristine BMPyr[NTf $_2$ ] a surface layer of zinc oxides are created, drawing a parallel to the Si-air pair suggests the creation of a SiO $_2$  layer, this is not desirable as such a layer would prevent discharge due to high resistances. Instead looking at part (b) in Figure 2.7 the suggestion is that the introduction of water into the RTIL will have said water act as a transport method. Preventing the growth of the oxide layer at the anode surface by moving the zinc ions into the bulk of the electrolyte. Thereby allowing continuous exposure of the anode to the electrolyte. The experiments that have been carried out show an increase in discharge potential and stable current based on adding varying amounts of water, as shown in Figure 2.8.

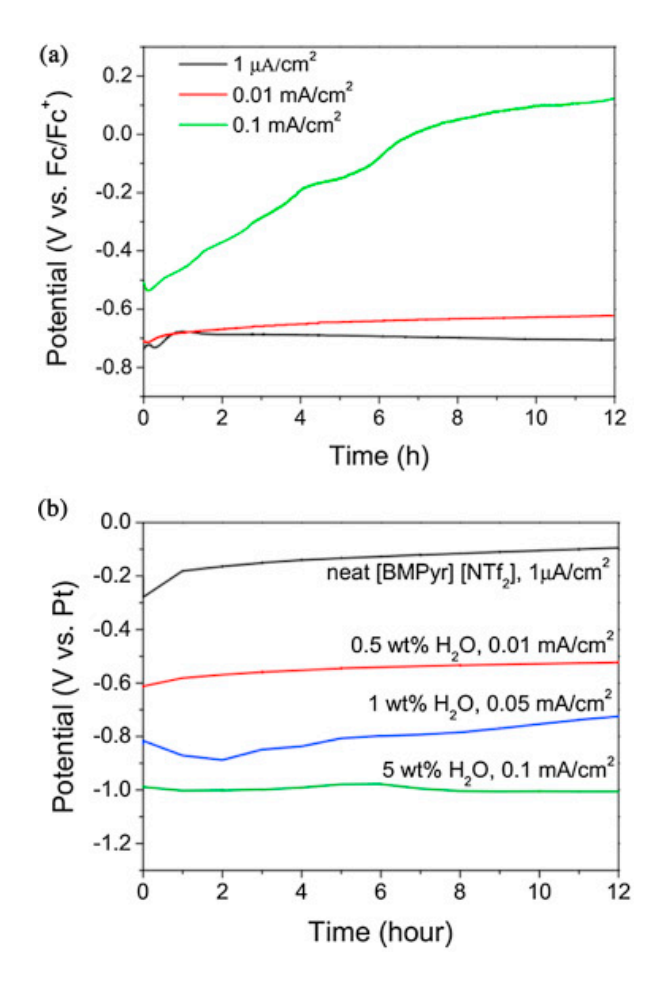


**Figure 2.8:** Displayed in (a) are the discharge curves using 0.5wt% water mixed with BMPyr[NTf<sub>2</sub>] for various currents and in (b) are shown the discharge using various different wt% water mixed with BMPyr[NTf<sub>2</sub>] with the highest current still providing stable discharge. Figure taken from [39].

Shown in (a) of Figure 2.8 are the discharges carried out using 0.5wt% water added to the RTIL for varying current, where it is seen that the discharge destabilizes for 0.1 mA/cm $^2$ . However in (b) of the same figure is shown a series of stable discharges using varying water concentrations. From this result it appears that BMPyr[NTf $_2$ ] shows an increased stable current and potential with increasing water, as the previously unstable 0.1 mA/cm $^2$  discharge is stable when repeated using 5wt% water.

This is of interest due to the work function of zinc, this being between 3.73 and 4.33 eV for zinc depending on crystal orientation [72]. Given that silicon has an electron affinity of 4.01 eV and with a band gap of 1.12 eV, this report hypotheses that a sufficiently doped sample of silicon will function in a similar manner to zinc in a metal-air battery setup. With a doping concentration of  $5 \cdot 10^{14}$  dopants per cm<sup>2</sup> the work function of silicon could be adjusted to be similar to the upper end zinc, that being 4.3 eV. Should instead the lower end of the zinc work function range be considered, the silicon will have no possibility of having a comparable work function. Given that it is lower than the electron affinity.

With the two RTIL's being covered, next will be given in Figure 2.9 the chemical structures of said RTIL's, BMPyr[NTf<sub>2</sub>] and BMIm[NTf<sub>2</sub>].

**Figure 2.9:** Shown here are the chemical structures of the two candidates, on the left side is shown the BMIm based RTIL and on the right side the BMPyr based RTIL. Retrieved from [70]

In this report these different anions will be further studied, though focus will be on BMPyr[NTf<sub>2</sub>] and BMIm[NTf<sub>2</sub>] will play a lesser role. To that end some key characteristics of these RTIL's will be given in Table 2.1.

**Table 2.1:** Shown here are the parameters of the discussed RTIL's, where the values are all given for a room temperature of 20 degrees celsius.

Parameter	$BMPyr[NTf_2]$	$BMIm[NTf_2]$
Conductivity (mS/cm)	2.21	3.23
pH (-)	8.6	7
Density (g/cm <sup>3</sup> )	1.392	1.43
Dynamic Viscosity (mPas)	98.8	63.8

As seen in this table both RTIL's have a high viscosity, namely 98.8 and 63.8 mPas, compared to the approximately 1 mPas dynamic viscosity of room temperature water. Similarly, the density of the RTIL is higher than that of both water and 6.6M KOH. With water having a density of 1 g/cm<sup>3</sup> and 6.6M KOH a density of 1.23 g/cm<sup>3</sup> at room temperature [73]. Finally as mentioned earlier the conductivity of these two RTIL's are low at room temperature.

## 2.6. Secondary Si fueled batteries

So far, only primary batteries have been considered. However, when considering Si-air batteries and their use as energy storage for the renewable future, secondary batteries are much preferred. A secondary battery is defined as a battery that can be reused. A secondary battery using Si-air has been demonstrated, however it was done at significantly elevated temperatures of 1073 K [74].

Recently however, a battery functional at room temperature has been successfully manufactured [75]. Unfortunately, the rechargeable nature of this battery has as requirement the absence of SiO<sub>2</sub>. Due to this, air cannot be introduced into the battery, meaning that this battery is not a Si-air pair. Furthermore, the parasitic corrosion still present using RTIL, as described in Section 2.5.2, needed to be suppressed further for a viable secondary battery. Therefore a different electrolyte was chosen, namely a hybrid electrolyte was used based on Py1,4-TFSI with 4%v/v Py1,4-HF2.3-F [75]. The novel design uses a bromine based cathode, leading to changed anode and cathode reactions as shown in Equations 2.16,2.17, respectively

$$Si_{n++} + x(FH)_nF_{sol}^- + yBr_{sol}^- \longleftrightarrow SiF_xBr_{y(sol)} + (HF)_n(sol) + 4e^- \tag{2.16}$$

$$Br_{3(sol)}^{-} + 2e^{-} \longleftrightarrow 3Br_{(sol)}^{-}$$
 (2.17)

with n++ subscript denoting that the silicon sample is highly n-type doped. And the subscript sol meaning colloid, effectively a mass of very fine particles. Furthermore was found that adding various colloids improved the battery performance even further. These colloids being  $Py_{1,4}$ -Br,  $Br_2$  and  $SiBr_4$ . Adding these in the previously named electrolyte at 0.1 M for the first three colloids and 0.2 M for allowed for 6 charge discharge cycles before battery failure, notably replacing the electrolyte post failure allowed further cycles to be executed. This can be seen in Figure 2.10

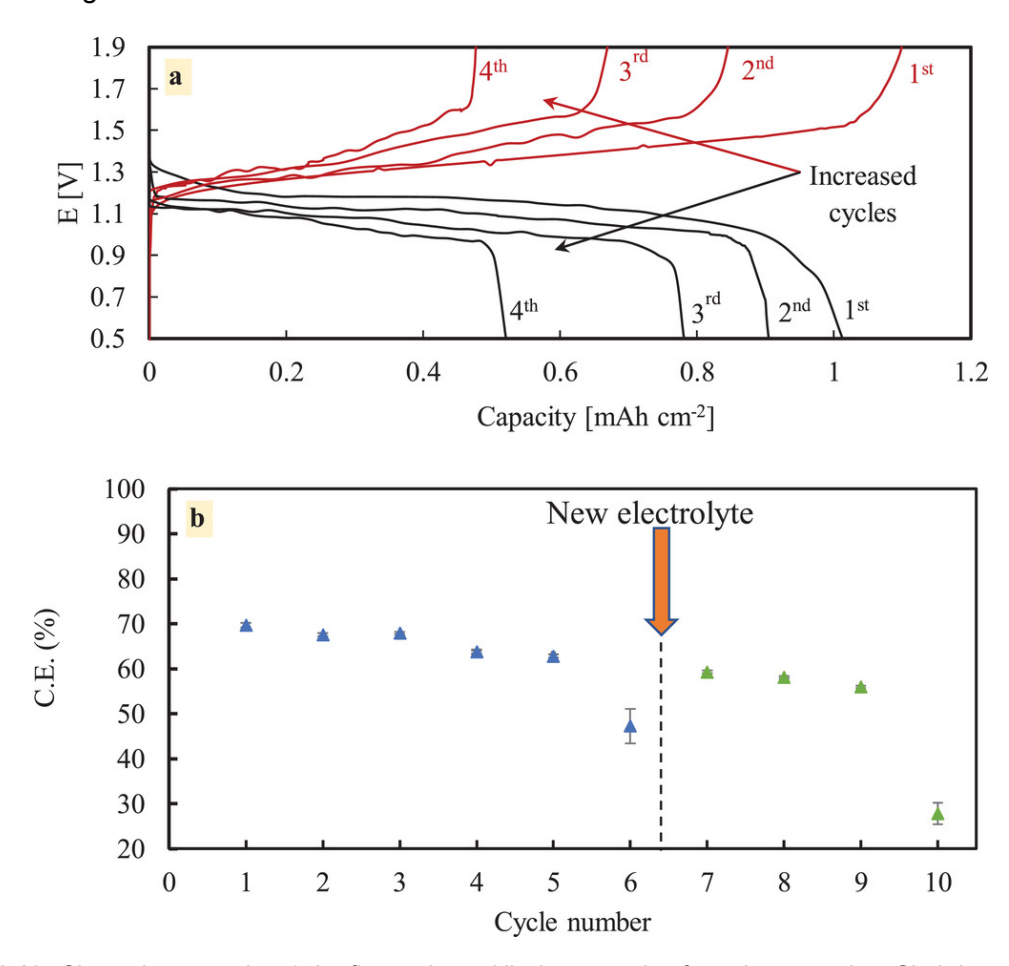


**Figure 2.10:** Shown here are the a) the first 4 charge/discharge cycles from the secondary Si-air battery and b) the measured coulombic efficiency for the first 10 cycles, note that after the  $6_th$  cycle the electrolyte is refreshed. Retrieved from [75].

Ein-Eli et al. find that this degradation of performance happens due to parasitic behaviour in the electrolyte leading to decreased dissolved Si and F species inside the electrolyte [75]. Further research into this type of battery may be of interest, as unlike the Si-air batteries thus far, this type of silicon redox battery is rechargeable, while still using silicon as the main fuel source.

## Experimental Method

The experimental method can be described in four parts, first the environment in which the experiments are conducted. Secondly, the preparation and assembly of the battery cell. Thirdly, the measurement methods are discussed, in particular the errors will be detailed. And lastly given are the specific experiments done using the prior parts. Covered in Sections 3.1 3.2, 3.3 and 3.4, respectively.

#### 3.1. Experimental Environment

Prior to describing the details of the experiments, it is important to note the environmental factors, as these may influence the results. To that end, the experiments were carried out in a Cleanroom facility provided by the Else Kooi Laboratory (EKL). Specifically the measurements have been carried out in an ISO class 7 Cleanroom and a select few steps of the anode preparation have been carried out in an ISO class 5 Cleanroom. The ISO class signifies the maximum number of impurities allowed in the air at 10000 particles of 0.5  $\mu m$  diameter or larger for the ISO class 7 and 100 of such particles for the ISO class 5. Further controlled in the environment are the temperature and the humidity. These are identical for the two Cleanrooms and are set at a temperature of 21  $\pm 2\,^{\circ} C$  and a humidity level of 48 $\pm 5\%$ .

During all measurements and actions within the Cleanroom appropriate gear is worn, including a Cleanroom suit, nitrile gloves and a face cover, these items are primarily to prevent the human from contaminating the environment and not necessarily a safety feature. When pouring chemicals additionally neoprene gloves, protective glasses and an apron are worn. These items are worn for safety reasons, as the experiments make use of KOH and HF, which are both dangerous chemicals.

### 3.2. Battery construction

The construction of the battery is covered in this section. Specifically the anode, cathode and electrolyte preparation will be detailed. The assemblage of the components and the clean up between experiments will also be covered.

#### 3.2.1. Anode

For the anode two brands of wafers were used, both manufactured using the Czochralski method. These brands being Topsil and Siegert. Shown in the following table are the characteristics of these two wafers as shown on their labels.

Table 3.1: Shown here are the parameters of the two brands of wafers, note that both are essentially identical.

Parameter	Siegert	Topsil
Doping Type (-)	N (As)	N (As)
Orientation (-)	<100>	<100>
Thickness (µm)	280	280
Resistivity (mS/cm <sup>2</sup> )	2-5	2-5

From Table 3.1 it is seen immediately that for all the listed parameters these two wafers are identical. However there have been anecdotal results which suggest that the Topsil wafer shows slightly superior passivation behaviour during deposition, when manufacturing for example a PV cell. This is not expected to influence the discharging behaviour of a Si-air battery created using these wafers however, and as such both these wafers have been used.

The wafers are cleaned of surface contaminants by going through a cleaning line, consisting of alternating baths of  $HNO_3$  and DI water, next the native oxide is removed by going through a maragoni cleaning line, using HF and IPA to remove the native oxide and passivate the surface of the wafer, this passivation will remain effective for at least a day after the maragoni process is finished, allowing for some flexibility in choosing when to apply the back contact. Following is the flowchart used during this process.

- Start heating the second HNO<sub>3</sub> bath to 110 degrees celsius, if not yet heated.
- Submerge wafers for 10 minutes in the 99% HNO<sub>3</sub> bath at room temperature.
- Rinse in DI water for 5 minutes.
- Submerge wafers for 10 minutes in the 69.5% HNO<sub>3</sub> bath at 110 degrees Celsius.
- Rinse in DI water for 5 minutes.
- Transfer wafers to the maragoni cleaning line. Ensure the bath is empty and load the wafers with primary flat facing downwards.
- Fill the bath with 0.55% HF.
- · Lower wafers into the bath and start a 4 minute timer.
- Once the timer is over, start adding DI water into the bath until the pH becomes neutral.
- Start the IPA flow and wait 1 minute for a cloud to form.
- Raise the wafers from the bath, the surface is now free of native oxide and passivated.

Once cleaned an 675nm thick Al(99%):Si(1%) back contact is applied through sputtering, done using a Trikon Sigma machine, this to ease the current collection. The machine available in the EKL CR100 has preset recipes which allow for an easy deposition of the back contact, as such the process in which this is achieved is simply inserting the wafers into the machine and selecting the appropriate recipes. If the machine has not seen a deposition using similar material in the last 2 hours, a dummy wafer is required in front of the to be processed wafers. This dummy wafer is to be used to execute a cleaning recipe, before the aluminium is to be sputtered on the target wafers.

Finally once the back contact has been deposited the wafer can be prepared into samples, this is done through the usage of a laser cutter and a CAD software to draw the laser shapes. This report has chosen to divide the wafer into squares of 16.2 mm width and length. The program attached to the laser cutter permits easy to change laser parameters. These parameters being the power of the laser, the speed at which the laser moves, the frequency of the laser and the number of loops the laser makes on the drawn path. This report has used the following

values for the parameters mentioned. The power of the laser was set at 100%, equalling 20 W, the speed at 150 mm/sec, the frequency at 100 kHz and a loop count of 15 was chosen.

#### 3.2.2. Cathode

The cathode consists of porous carbon with a magnesium oxide (MgO) catalyst, the cathode is given structure by a nickel mesh. The cathode is obtained in a prepared state from the company "Electric Fuel" as shown in Figure 3.1.



Figure 3.1: A roll of the cathode. Partially used up.

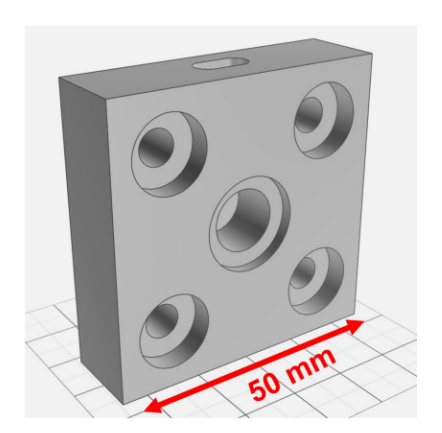
This roll of the cathode material is cut into appropriate pieces when assembling the battery. Of note is that the cathode due to its porous nature can have leakage occur when used. This leakage is difficult to prevent in the currently proposed set up, as such it should be worked around in terms of replacing the electrodes whenever they get degraded by the leaking KOH or Room Temperature Ionic Liquid (RTIL).

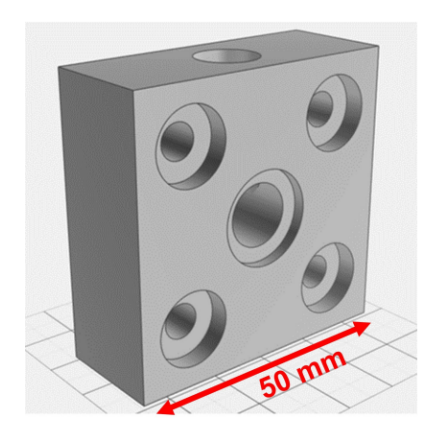
#### 3.2.3. Electrolyte

This work has used three distinct electrolytes in the preparation of the battery, namely KOH, BMIn[NTf $_2$ ] and BMPyr[NTf $_2$ ]. The two RTIL's have been purchased from the chemical company Solvionic, the KOH was available in the EKL cleanrooms in a 30% solution, corresponding with a molarity of 6.6M. The KOH has been used at various concentrations, varying from 6.6M to 0.22M. The two RTIL's have been primarily used in pristine condition, but BMPyr[NTf $_2$ ] has seen some slight water mixed into it, up to 3wt%. Of these electrolytes, KOH has shown the ability to corrode SiO $_2$  which allows simplification during the preparation of the battery, as the native oxide layer present on the samples does not need to be removed first. The two RTIL's have not shown this ability and as such require a preparatory step to remove this oxide layer.

#### 3.2.4. Battery Design

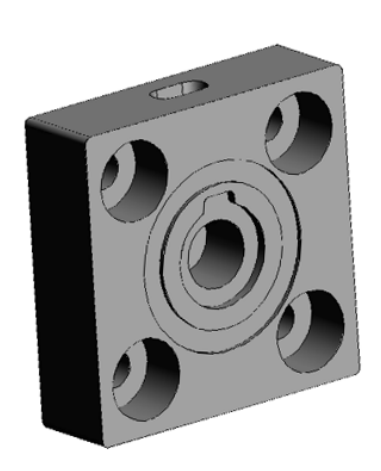
The battery used in this paper initially has the same design as used previously by R.Coerkamp, however some modifications were made in the later stages in an attempt to reduce the resistance in the cell and to improve the ease at which the electrode may be replaced. Figure 3.2 shows a schematic of the older design.

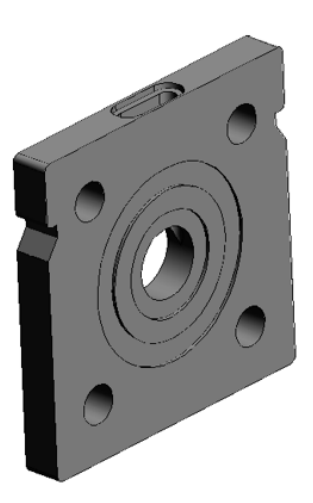




**Figure 3.2:** On the left hand side the anode and cathode containers are displayed, on the right hand side the electrolyte container, the central hole is where the battery set up is aligned, the corners are for screws to assemble the battery. Retrieved from [48]

In this design the central container depicted on the right of Figure 3.2 has the following dimensions 50 mm x 50 mm x 20 mm, where 20 mm is the thickness of the piece. This 20 mm therefore is also the distance between the two electrodes in the assembled battery cell. This central container is also where the electrolyte will be held, which after assembly can simply be poured down the hole present at the top. The volume of electrolyte which fits into the container is 4 ml. Note the indents in the center of both containers, these are used to place O-rings when assembling the battery, as otherwise the liquid electrolyte may leak out of the battery. These O-rings have an inner diameter of 11 mm. Shown next in Figure 3.3 is the updated design.

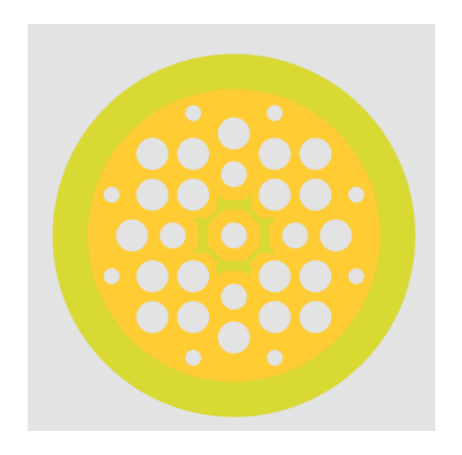


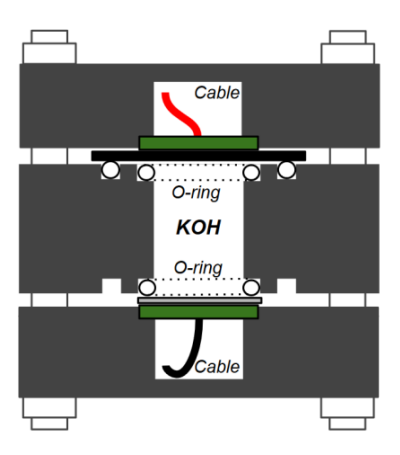


**Figure 3.3:** Shown here is the new battery design. On the right is shown the anode/cathode container, which has an added indent to allow for easier PCB replacement. On the right is shown the electrolyte holder, which is compared to the older design more than twice as thin, at only 8 mm thickness.

The main difference between the two designs of the battery cell is the thickness of the central segment, which is where the electrolyte is contained. This thickness influences the resistance

encountered by the battery cell. As such, the new design with the lower thickness has with the same electrolyte a lower resistance than the old cell. This thinning of the center segment is not without disadvantages however, as the volume is reduced. Furthermore, due to the thinner reservoir, the indents where the O-rings are to be placed are less deep, as such thinner O-rings are required in comparison to the older design. A small indent is added to the center ring to allow for easier replacement of the PCB's when necessary. The PCB's themselves are unchanged compared to those used by Coerkamp [48] and the schematic below shows said PCB and a cross-sectional view of the assembled battery. The cross-sectional view is of the older design, however the new design is largely the same, only the central section would be thinner.





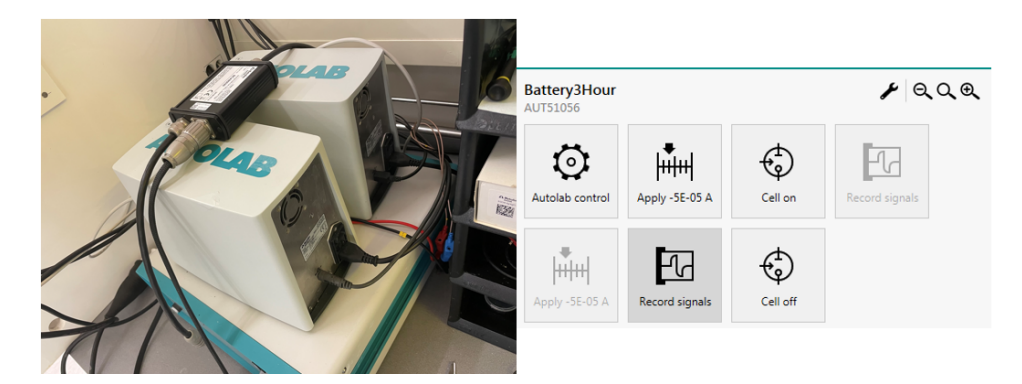
**Figure 3.4:** Given on the left is the used PCB design, notable are the holes in the design which allow for air flow. On the right is a cross-sectional view of the assembled battery, including the PCB connections, the anode, cathode, electrolyte and the O-rings. Retrieved from [48].

Figure 3.4 shows the PCB on the left and a cross-sectional view of the old battery design on the right. The PCB is plated with gold to improve longevity when used with KOH.

#### 3.3. Measurement

There are four measurements being done in this report, namely a galvanostatic discharge, a weight measurement, a step height measurement and a conductivity measurement. These are done using an Autolab, a scale, a Dektak profilometer and a conductivity meter, respectively.

An autolab is used for the galvanostatic discharge plot, the one available in the EKL clean-room is manufactured by "Metrohm". The autolab comes with an application containing a robust GUI, this application is used to execute the measurement, below Figure 3.5 shows a picture of the autolab in question and a screenshot of the settings.



**Figure 3.5:** On the left is shown the metrohm autolab the EKL possesses of two such machines, for the purposes of this report however they are used individually, as such having a single machine is sufficient. On the right is a screenshot of the settings window of the autolab program. Where the control block determines what type of discharge happens and the current range.

These settings are used for all experiments, with some small edits where appropriate. Notable such edits are the inclusion or exclusion of an OCP period prior to discharge. The adjustment of the current range, the discharge current and the measurement time. The current range is important due to the machine having an accuracy dependant on said range, with the accuracy being 0.1% of the selected range. The machine has as available ranges 10 nA up to 1 A, with steps of one order of magnitude between each range. The range signifies the maximum negative and positive current which can be set. Where a negative current represents discharging and a positive current charging.

The autolab comes equipped with five connections, a Working Electrode (WE), a Counter Electrode (CE), a Reference Electroder (RE) and the ground and sense connections. Of these five, four are used in a two electrode setup such as the battery in this report. Namely the WE, the CE the RE and the sense. A schematic representation of how these connections are ordered is shown in Figure 3.6.

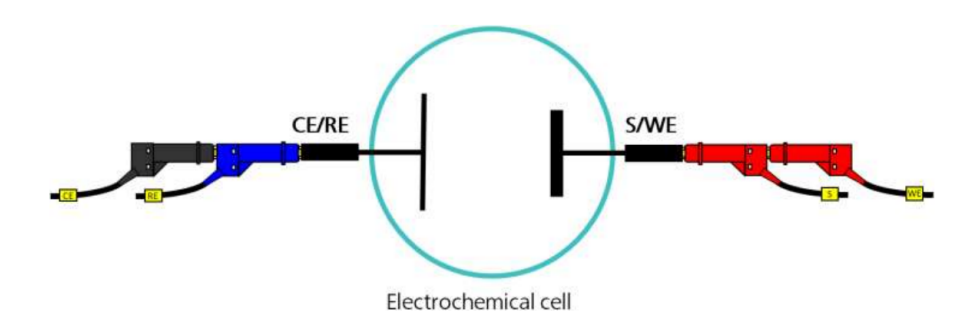


**Figure 3.6:** This figure shows the way in which the connections should be arranged when used in a two electrode setup. Here the CE and the RE are short-circuited and connected to the anode. Meanwhile the Sense and the WE are short-circuited and connected to the cathode side. Retrieved from [76]

In Figure 3.6 the way the connections are arranged is shown. From the manual it is obtained that the sense should be directly connected to the cathode when working with high current. As this report does not use high currents, the order in which the two connections on each electrode are connected does not matter [76].

Once connected properly the measurement can be started, which will measure the potential based on a preset constant current. The returned results from the measurement will include

the time, the potential and the current.

The mass can be calculated through usage of a weight scale, however, as this method uses the difference in the weight before and after the discharge care must be taken with error propagation. Furthermore, as the scale is very sensitive and the expected weights are small, the samples must be cleaned thoroughly to ensure no contaminants are present. The EKL is equipped with nitrogen gas guns which allow efficient removal of moisture.

With there being two measurements, Equation 3.1 can be used to determine the error of the mass.

$$\sigma_{\text{total}} = \sqrt{\sigma_{\text{before}}^2 + \sigma_{\text{after}}^2}$$
 (3.1)

where the sigma represents the error in each instance, valued at 0.1 mg for both instances. This gives a total error of  $1.4*10^{-4}$ g.

Once the mass difference is known, the mass lost to parasitic consumption can be obtained with the following equation, assuming there are no other mechanisms which consume the Si.

$$m_{\text{difference}} = m_{\text{discharge}} + m_{\text{parasitic}}$$
 (3.2)

where the discharge mass in grams can be obtained with the equation below.

$$m_{\text{discharge}} = \frac{3.6 \cdot 10^3 JAt}{\frac{nF}{M_{Si}}} \tag{3.3}$$

in which J is the current density in Ampere, A the surface area in  $cm^2$ , t the discharge time in hours, n the number of electrons involved in the discharge reaction, 4 for Si, F the faraday constant, taken to be 96485 C/Mol and  $M_{Si}$  the molar mass of silicon, taken to be 28.05 g/mol.

Taking Equations 3.2 and 3.3 together an expression for the mass lost to parasitic consumption can be found, as given below.

$$m_{\text{parasitic}} = m_{\text{difference}} - \frac{3.6JAt}{\frac{nF}{M_{\text{Si}}}}$$
 (3.4)

Finally, the efficiency can be obtained through dividing  $m_{\rm discharge}$  through  $m_{\rm difference}$  and multiplying by 100%. As shown following.

$$\eta = \frac{3.6JAt}{m_{\text{difference}} \frac{nF}{M_{\text{Si}}}} * 100\% \tag{3.5}$$

Where  $\eta$  is the efficiency of the reaction in %.

Next is the step height measurement, which is carried out using a Dektak profilometer, which also comes connected to a computer with an accompanying GUI. In this GUI parameters for the scan can be inputted such as the scan length, needle force and scan time. The scan parameters settled on in this report are 12500-15000  $\mu$ m scan length, default needle force and 90 seconds scan time. The length has varied during the course of the report, however the key detail is for it to be sufficiently large to measure both sides of the step, allowing for a simplified levelling of the results. Figure 3.7 shows a picture of this machine.



**Figure 3.7:** The interior of the Dektak profilometer, the sample is to be placed on the silver coloured disc and has to be manually put into position beneath the red needle.

Once the step height is measured, the mass can be calculated through multiplying with the surface area to obtain the volume and then multiplying with the density of silicon to find the mass. The losses will be the result minus the effectively used mass. Said effectively used mass is determined using Equation 3.3.

However, the step height is not perfectly flat nor is the machine perfectly accurate, therefore determining the volume requires consideration of the errors present. The method implemented in this report is to take the difference between the pre-step height and the post-step height. Where the errors in both are calculated through using an polynomial approximation, using the fact that both sections should in theory be flat. Once both errors are determined the total error can be determined using Equation 3.1. This method however does have a weakness, namely it requires a human to decide what constitutes as pre-step and post-step, a distinction which can vary the result. In this report the decision was chosen to take all the points which are within the upper 10% of the full range as pre-step height and within 10% of the bottom of the full range as the post-step height. Or if the range is larger than 10000 nm, the data points within 1000 nm of an extreme.

Finally the conductivity of the RTIL is measured using a conductivity meter. The meter used in this report possesses multiple ranges in which it can measure conductivity, these being 20  $\mu$ S/cm, 200  $\mu$ S/cm, 20 mS/cm and 200 mS/cm. The error is the greater between 0.3% of the used range and 2  $\mu$ S/cm. The machine is capable of automatically selecting the optimal measurement range. The error is equal to 0.1% of the measurement range.

3.4. Experiments 32

#### 3.4. Experiments

For this work a series of experiments have been carried out. The previous sections have described the general steps to prepare the materials and the methods by which data can be acquired. This section instead will cover what experiments exactly were conducted and the steps taken to do them.

#### 3.4.1. Verifying setup

The first step taken experimentally in this report is to verify the prior steps, to ensure the theory and the application thereof is done correctly. To that end the first experiment seeks to replicate past results. The choice was made to attempt to replicate a discharge using 6.6M KOH without any further adjustments to the anode or cathode, using the older design. The steps taken for this are used as the basis for each following experiment, with minor adjustments depending on the experiment. As part of this verifying process both of the anode options were used, so that they can be compared to each other and to find any differences, if they exist.

Below is an itemized list of steps taken for this initial experiment:

- Cut a cathode segment into appropriate size and assemble half the battery cell.
- Measure the weight of the anode, then assemble the full cell and fill with 6.6M KOH.
- Connect the cell to the autolab, input discharge current and time, then start the measurement.
- After finishing the measurement, disassemble the cell and clean the anode thoroughly with DI water.
- Once cleaned weigh the anode sample on a scale and measure the step height using the Dektak profilometer.
- Clean the battery cell after the test and measure the resistance through the PCB's, replacing them if the resistance grows beyond 10  $\Omega$

Of these steps the electrolyte used to fill the battery will change depending on the experiment in question, furthermore, if necessary a cleaning step to remove native oxide will also be added.

Shown in Figure 3.8 is a series of pictures depicting the battery cell using the old design, in various stages of assemblage. This sequence of assembly will remain unchanged for all the following experiments that use either of the battery designs.

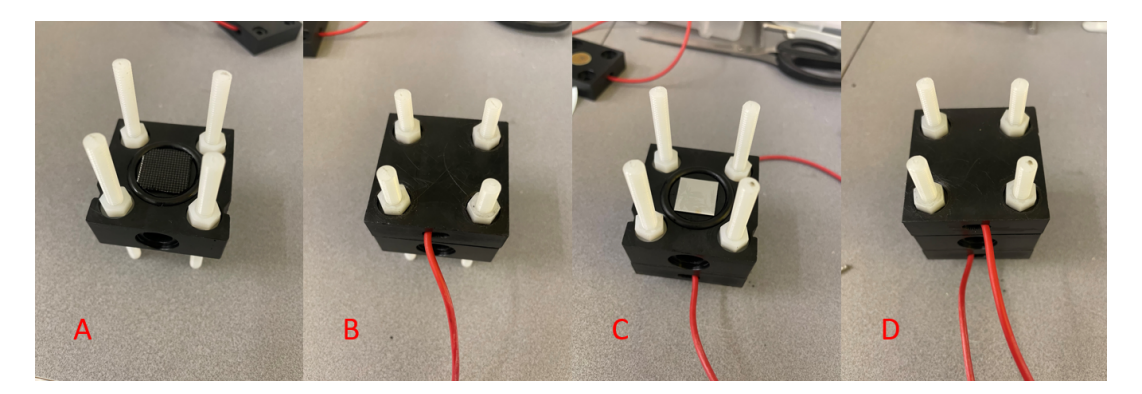


**Figure 3.8:** Shown here is the battery cell in various stages of assemblage. The stages are denoted by letters, A to D and correspond to the following situations. A, the cathode is cut into the correct shape and placed on the center piece. B, the cathode side is fixed in place using an outer piece and bolts. C, the anode is prepared and placed on the other side of the center piece. D, the anode is fixed in place using an outer piece and bolts.

Naturally, it is important to set parameters for each measurement. For this part of the experiment, the intention is to verify the set up is working accurately, as such the aim has been to set the measurement parameters to ones which have been used before in the literature. This equals to setting the current to 10  $\mu$ A for every test, repeating the test three times at 2, 5 and 20 hours of discharging. Where an one hour OCP period is set to remove the native oxide prior to the discharging. This way there is no need to work with HF yet.

Secondly, after testing that the setup is working properly using the older battery design, the new design should be verified as well. The expectation here is that it should work in a similar manner, but with slightly higher potentials due to the decreased width of the reservoir, which would have decreased the resistance experienced by the system. To that end, a similar set of steps as the previous experiment are undertaken. After which the two discharge profiles are compared to see what the difference, if any, is. The weights however are not compared as the overall reaction is still the same.

#### 3.4.2. RTIL characterization

The aim in this section is to determine some basic characteristics of the RTIL, given that the chosen RTIL has not yet before been used in a Si-air battery pair, there is little known about how it would function, if at all. From literature it was obtained that this RTIL has seen limited use in a Zn-air battery setup. With the rough estimate that Si and Zn have semi comparable work functions, the initial experiment assumed that the two anodes would show similar discharge potential. To that end the following tests were undertaken:

- Test on whether the RTIL works at all, through using a similar testing set up as described in Section 3.4.1 To minimize the variables, the native oxide layer should be removed prior to the test starting. Once it has been established that the battery cell does discharge, a second test should be carried out to see what the influence, if any, of native oxide is.
- Test what is the limiting factor of the discharge. This is done by running repeated measurements at the same parameters, but changing components between measurements.
   By varying the anode, cathode and electrolyte, it can be seen which of these three components limit the discharge capacity.
- Test the limits of the pristine RTIL, in terms of discharge time and potential. This is done
  through repeating the prior experiments at various escalating currents for short periods
  of 10 minutes. Should the potential reach 0 V within a 10 minute period the experiment
  will be halted.

Care should be taken during the cleaning of the set up after testing with RTIL as the liquid is viscous a-polar, therefore difficult to remove with only water. The liquid further barely experiences any evaporation and has been seen remaining on surfaces for at least 2 weeks during the experiments. In this paper it has been opted to clean using a combination of wiping with cleanroom paper and application of IPA.

#### 3.4.3. Testing KOH concentrations

Next tests are done using varying KOH concentrations, as mentioned in Section 2.5.1 KOH experiences a change in conductivity depending on the concentration. The aim here is to see what the effect of this conductivity has on the discharge pattern. Naturally the discharge is not solely influenced by the conductivity. For example it has been mentioned that at low concentrations the battery will experience rapid passivation at sufficiently high currents. To prevent this from being a factor, the decision has been made to start this set of experiments at a low current. This current has been chosen to be 1  $\mu$ A. By varying the concentration from 6.6M to

0.22M, a gradient of discharge curves are obtained. The experiment will be repeated for 50  $\mu$ A to observe the effects of higher current combined with lowered concentration.

For both series of experiments an important additional step is necessary, before weighing and assembling the full battery cell, the anode must be cleaned, the native oxide layer must be removed. This is due to the varying concentration leading to different times required for the KOH to naturally remove the native oxide layer. Therefore, to prevent this variance in the result, instead the native oxide layer should be removed in advance so that each measurement retains the same duration. The removal of this native oxide is done through dipping the anode samples into a 0.5% HF solution for 2 minutes. The etch rate of  $SiO_2$  in 0.5% HF is not known, but extrapolating from the etch rate of 49%, 5% and 2% HF it is estimated to be around 2.5 nm/min [77]. This is sufficiently long to remove any native oxide layer, yet not long enough to remove the aluminium back contact layer.

These two sets of experiments are aimed at increasing the understanding of the way the conductivity and concentration of KOH influences the discharge. This can be compared to the RTIL to see if this shows a similar behaviour.

#### 3.4.4. Testing RTIL concentrations

The final set of experiments will use RTIL mixed with water which is hypothesized to change the conductivity, as discussed in Section 2.5.2. As the literature where this RTIL was mixed with water used wt%, so too will that be done in this paper. Specifically the tests will be done using 1wt% and 3 wt%. Note that the RTIL has a higher density than water and as such should weighed to ensure the correct amount of water can be added. The steps taken in this paper are as follows:

- Weigh an beaker and set the scale to zero, then pour in approximately 20 ml of the RTIL.
- Measure the weight of the poured RTIL and add DI water as appropriate using a pipette.
- · Mix vigorously and measure the conductivity of the mixture
- Construct the battery cell as previously done, taking care to remove the native oxide layer of the anode.
- Add the RTIL mixture and start the measurement, as the two liquids do not mix due to being polar and a-polar, mix them once again prior to pouring into the battery cell.
- Repeat for varying current and varying water concentration

Due to the RTIL being a-polar, water and the RTIL do not mix, instead what is created is an emulsion. As mentioned in one of the steps this necessitates remixing prior to every experiment. However this leads to a second potential issue. Namely given that water is of lower density than the RTIL, it will float on top of it, thereby being exposed to the air. When the emulsion breaks this will cause the water to be able to evaporate, leading to gradually reducing water content in the electrolyte.

Furthermore, in combination with the previous section, tests regarding the anode will be done. Namely, to check whether or not it is a  $SiO_2$  layer which is being created on top of the anode during discharge. This will be tested by discharging an sample at 1  $\mu$ A until the potential has dropped to 50% of the initial value, afterwards the sample will be submerged in 0.55% HF and then reused in the same conditions. Should the reduction in potential be caused by the formation of an  $SiO_2$  layer, it is expected that the potential will have recovered to some degree as HF removes  $SiO_2$ . In this report the used anode was submerged for 2 minutes, similar to the length that was used to remove the native oxide layer. This short period ensures that

3.4. Experiments 35

the aluminium back contact does not become damaged, yet is still long enough to remove approximately 2 nm of  ${\rm SiO}_2.$ 

# 4

### Results

In this chapter the results of the experiments are discussed. These results will be split into four sections, namely the verification of the set up, the characterization of the Room Temperature Ionic Liquid (RTIL), the conductivity comparison using KOH and the same using RTIL. In Sections 4.1, 4.2, 4.3 and 4.4, respectively.

#### 4.1. Verification of setup

First shown will be the tests done to verify the set up, in order to ensure that the components are all working as expected and to minimize user error in any measurements.

#### 4.1.1. Reproducibility

The initial tests that were done aimed at understanding the used machinery and ensuring that the setup is working properly. During these tests it was learned how the measuring set up worked and how to construct the battery properly and in a safe manner. As such the expected outcome for these tests is to show behaviour similar to that found in the by Durmus et al. and Coerkamp [37][48]. Shown below in Figure 4.1 is a 6 hour discharge of the battery cell Si anode based on a wafer supplied by Topsil. The discharge is preceded by an 1 hour OCP period to remove native oxide, the discharge itself is executed at 10  $\mu$ A.

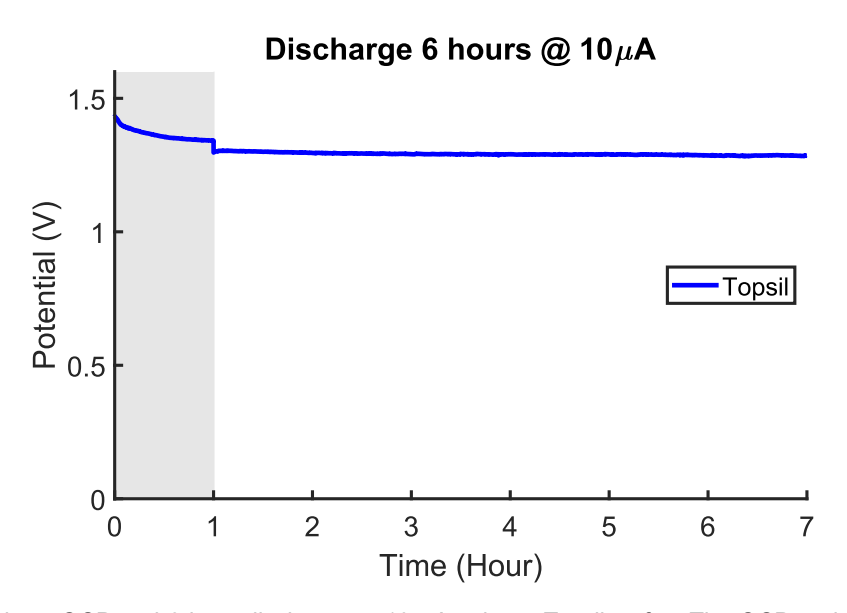


**Figure 4.1:** 1 hour OCP and 6 hour discharge at 10  $\mu$ A using a Topsil wafer. The OCP period is highlighted in grey.

This figure clearly shows two regions, namely the OCP period during the first hour and the discharge in the following two hours. During the OCP period the measured potential is higher than during the discharge period. However, in contrast to the results by Coerkamp [48], during the entire OCP period the potential is around 1.3-1.4V. Where the results from Coerkamp have a low initial potential in this OCP period that increases to the expected 1.3-1.4V value in approximately 40 minutes [48]. The absence of this low initial potential suggests that there is no native oxide layer present at the start of the OCP period.

Corresponding with this measurement is also the step height measurement as shown in Figure 4.2.

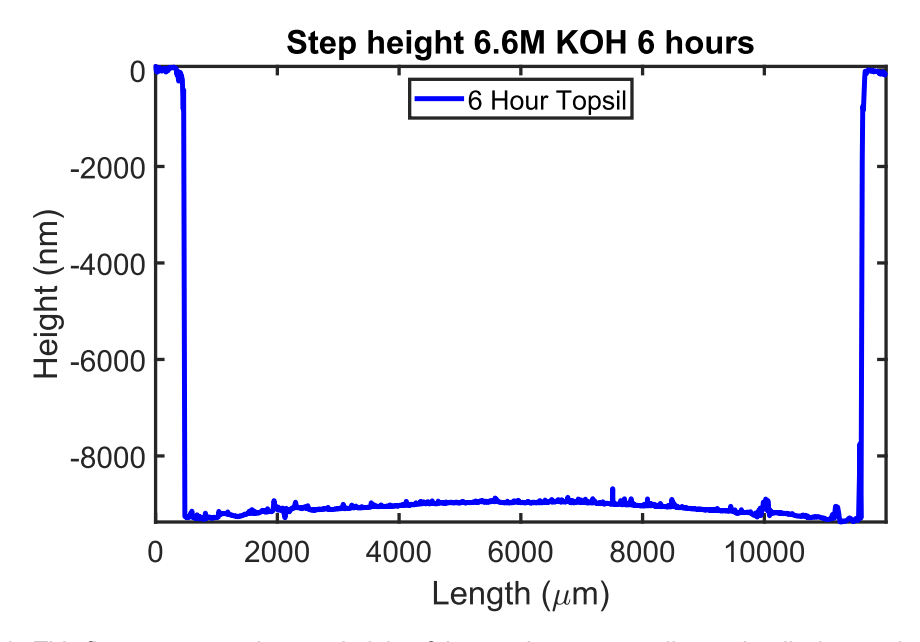


**Figure 4.2:** This figure presents the step height of the anode corresponding to the discharge shown in Figure 4.1. The step height has been measured by scanning the sample lengthwise.

Here the average step height is  $9.0\pm0.1~\mu m$ . The first hour during the discharge was at OCP, the results obtained indicate that no SiO<sub>2</sub> was present. Mentioned in Section 2.5.1 is the slow corrosion speed of SiO<sub>2</sub>, happening at only 3.4 nm/hour at 6.6M KOH concentration. Figure 4.1 implies an absence of a SiO<sub>2</sub> layer at the start of the OCP period, therefore, the Si sample effectively has been in direct contact with the KOH for 7 hours. This increased exposure time suggests that the Si consumption rate is approximately 1.3  $\mu$ m/h.

This consumption rate is greater than what was found by Coerkamp [48] where a Si consumption rate of 1.25  $\mu$ m/h was found at a current of 50  $\mu$ A using KOH of the same concentration. There exists one difference between the experiment ran by Coerkamp and the one presented in this report.

This experiment was conducted at 10  $\mu$ A instead of 50  $\mu$ A, however, this is not expected to influence total amount of Si consumed in a major way, as a large majority of the corrosion will be due to the parasitic reaction (>97%) [37][48]. The mass of the Si used by the discharge reaction, given in Equation 2.6, is calculated using equation 3.3, the step height can be obtained by dividing this mass by the active surface area, and the density of Si. The active surface area used here is 1.6 cm², the reason behind this is discussed in Section 4.1.2 and further elaborated on in Appendix B. For the discharge in Figure 4.1 this step height is 68

nm. This is approximately 0.75% of the total step height. An increase in the current to 50  $\mu$ A would in theory increase the step height by approximately 280 nm. Over an 7 hour period this corresponds to 40 nm/hour, this lies within the error of 100 nm/hour.

There is a difference of 0.25  $\mu m$  in total silicon consumption between the result here and that found by Coerkamp. Given that the difference in discharge current is not the cause, a different possibility is explored. The disassembly of the battery and the removal of the KOH from the battery cell requires time, during this time the KOH is still in contact with the Si anode. This time is estimated to be around 5 to 10 minutes. The exact time varies per experiment and in this report has not been measured.

The method by which the step height and the error are acquired has been discussed in Section 3.3. However, a visual example is also given in Appendix A.

#### 4.1.2. Comparing silicon anodes

Next the reproducibility is tested where silicon from two suppliers, Topsil and Siegert are investigated and compared to values which were obtained by Durmus et al. [37] and Coerkamp [48]. To that end the aim has been to create identical situations in which both anodes are discharged in a similar manner. As the experiment was conducted in the EKL CR10000, the environment can be considered the same for every experiment, for the battery cell itself the important part is to use the same electrolyte, 6.6M KOH in this case. With this the two anodes can be discharged at the same current for the same duration, allowing for a comparison between the two. Shown below in Figure 4.3 are the discharge curves for both anodes at 10  $\mu$ A for 2, 6 and 18 hours. Each discharge is preceded by an 1 hour OCP period.

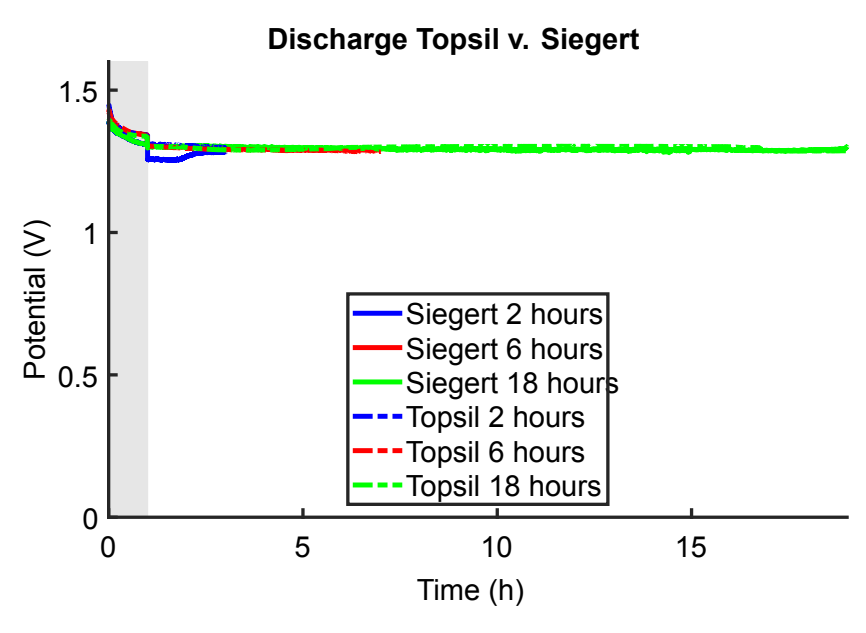


**Figure 4.3:** Depicted are six discharges, done for three different run times and the two different anodes. However all other parameters are the same. The first hour of each measurement is held at OCP, again highlighted in grey.

Figure 4.3 displays six discharge curves, all measured at 10  $\mu$ A for varying times using the two anodes discussed. This test serves two purposes, namely first to compare the two anodes and see if there are any differences, but second is also to test the system for reproducibility. As the discharge current and the electrolyte are the same across the tests, the result should remain consistent. If the anode has no effect, all six measurements should be the same. This

behaviour can be seen with two exceptions. Namely during OCP in the first hour, the potentials are not aligned and for the 2 hour Siegert discharge it appears the potential started at a lower level compared to the other five discharge curves.

Next two step heights are compared where using the Dektak a surface height profile is obtained for each sample. These profiles are given in Figure 4.4.

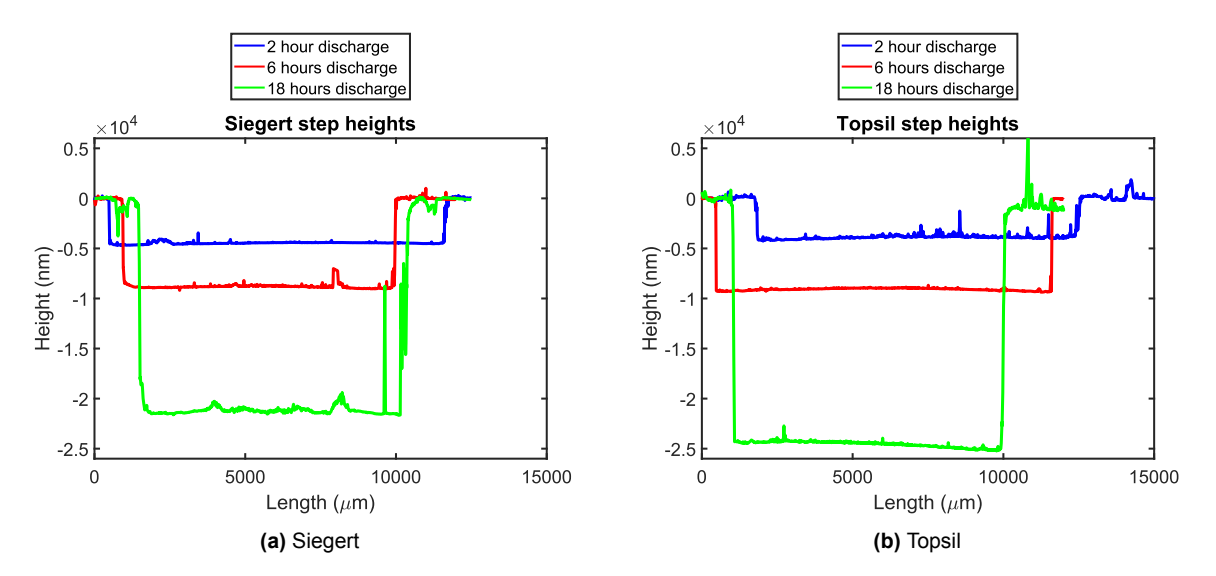


**Figure 4.4:** Displayed are the heights of both the Siegert and the Topsil samples. Of note is that one of the Topsil measurements used a larger scan length than the remainder of the measurements, however this has no impact on the step itself.

It can be seen in Figure 4.4 that the 2 hour discharge shows similar step heights for both samples. However, in the 6 and especially 18 hour discharge there are larger differences between these two samples. This may be caused by differences in the time it took to remove the KOH from the samples. As the KOH will continue to corrode the silicon sample even when the discharge is finished, removing the KOH later would lead to a larger amount of consumed silicon. This was the case with the 18 hour Topsil measurement, where the removal of the KOH was delayed by one hour due to unexpected experimental circumstances, this delay effectively adds an additional hour of OCP. Due to this the Topsil sample had been in contact with KOH for a total of 20 hours, consisting of 2 hour of OCP and 18 hours of discharge. With these step heights obtained the mass can be calculated using the surface area and the density of silicon.

There were two methods through which the mass was determined, namely through a scale and through the step height. Given that the surface area of 1 cm<sup>2</sup> was an assumption made based on the work of Coerkamp [48], to test whether or not this is applicable the two weighed mass and the calculated mass are plotted against each other in Figure 4.5

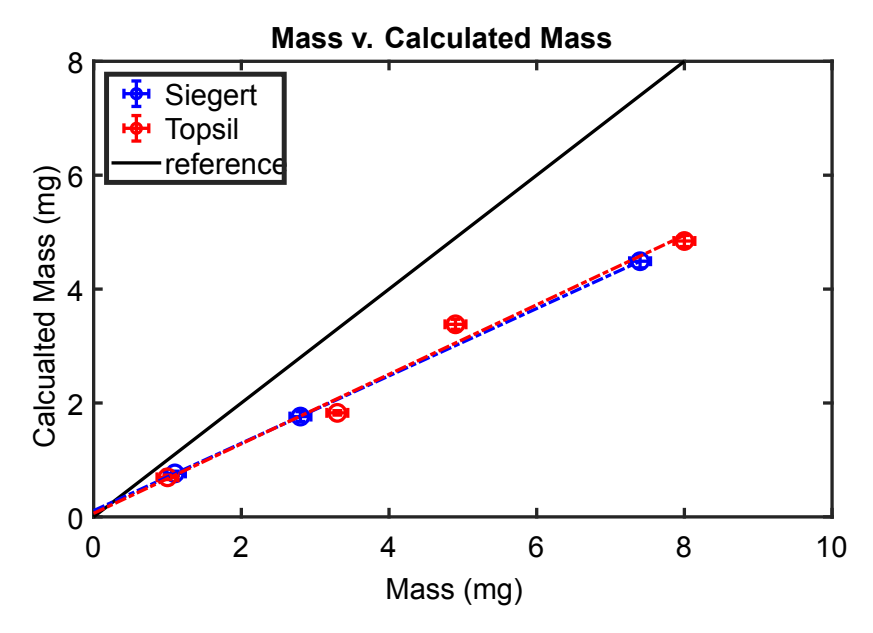


**Figure 4.5:** Plotted here are the calculated mass on the y-axis against the weighed mass on the x-axis. In black is a line representing the two masses being equal. A first order polynomial fit is made through the data points.

Additionally in Figure 4.5 a black reference line can be seen. This line represents the 1:1 ratio between weighed mass and calculated mass. As can be seen the data points do not follow the black reference line, instead they lie beneath it. This difference is due to the calculated mass obtained from the step height measurement is smaller than the weighed mass. This is only possible if the surface area used to calculate said mass is wrong. The fitted line follows the reference closer for an surface area of 1.6 cm<sup>2</sup>, this represents an increase in the diameter of approximately 3 mm. The width of the O-ring is approximately 2 mm, thus an increase of 3 mm in diameter is possible if the KOH can reach the silicon under the O-ring. Thus an surface area of 1.6 cm<sup>2</sup> will be used for the mass calculations using the step height. See Appendix B for further elaboration on the active surface area.

In terms of discharge potential the two anodes are similar, however in terms of consumed mass they differ as can be seen in Figure 4.5. Shown below in Figure 4.6 are the total consumed mass assuming a surface area of 1.6 cm<sup>2</sup> for the two anodes and their corresponding fits.

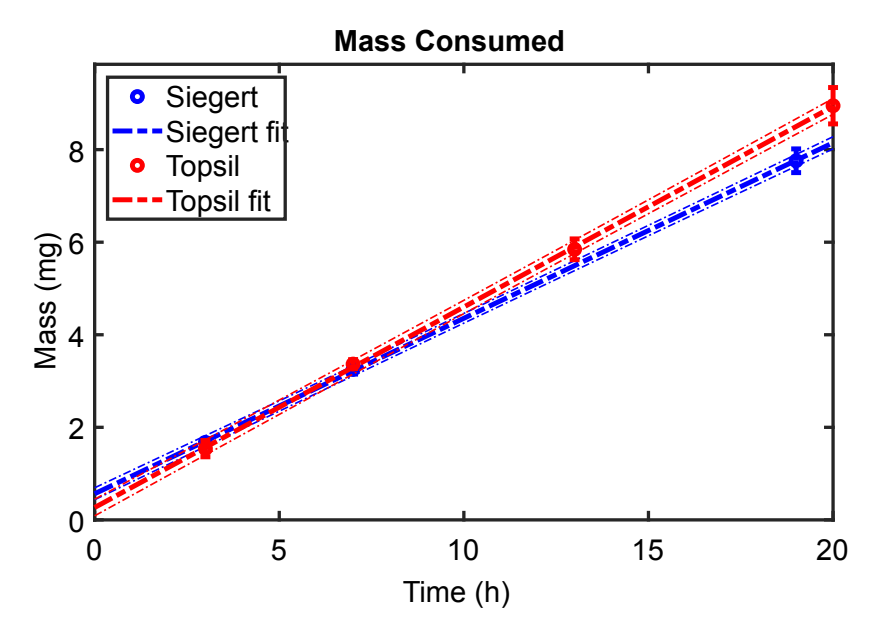


**Figure 4.6:** Given in this figure is the total mass consumed versus the time for both anodes, using the mass determined by a scale. Included are the first order polynomial fits of the data points and their 95% confidence intervals.

The linear fit seen in Figure 4.6 follows the points closely as expected when considering the consistent electrolyte and discharge current. Note that this figure displays the total consumed mass, therefore both the OCP period and the discharge period are included, hence the furthest Topsil data point being at T = 20 hours. The results indicate that during discharge slightly more silicon is consumed when using the Topsil wafers in comparison to the Siegert wafers, though initially the consumption is somewhat smaller. However, it can be seen in the fit that the error margin is slightly higher for the data measured on the Topsil samples. The error of the Topsil sample on average being 0.22 mg and the error for the Siegert sample being on average 0.14 mg. Finally from the fit is obtained a corrosion rate for the Siegert sample of 0.38 mg/hour and for Topsil a consumption rate of 0.43 mg/hour. Note that the fit does not pass the origin at T = 0, this is possibly caused by small errors in the measurements, as during the process of disconnecting and dismantling the battery cell the KOH still remains in contact with the anode sample, thus the corrosion reaction will still be happening. The time it takes to disconnect and disassemble the cell was not measured in this report, but is estimated to be between 5 to 10 minutes.

#### 4.1.3. Comparing battery design

In order to lower the resistance of the electrolyte, a new cell was designed of which the distance between the electrodes was 0.8 cm. For comparison a measurement was carried out at 1  $\mu$ A with the old and new cell, having a distance of 2 cm and 0.8 cm, respectively. The hypothesis is that this lowered resistance will increase the discharge potential by way of lowered ohmic overpotential. However, the reduced volume of electrolyte may lead to the electrolyte evaporating too quickly. This has been done through doing the same measurements with both battery designs using 6.6M KOH as electrolyte. Shown below are the discharge curves of both battery designs, for the same current and time.

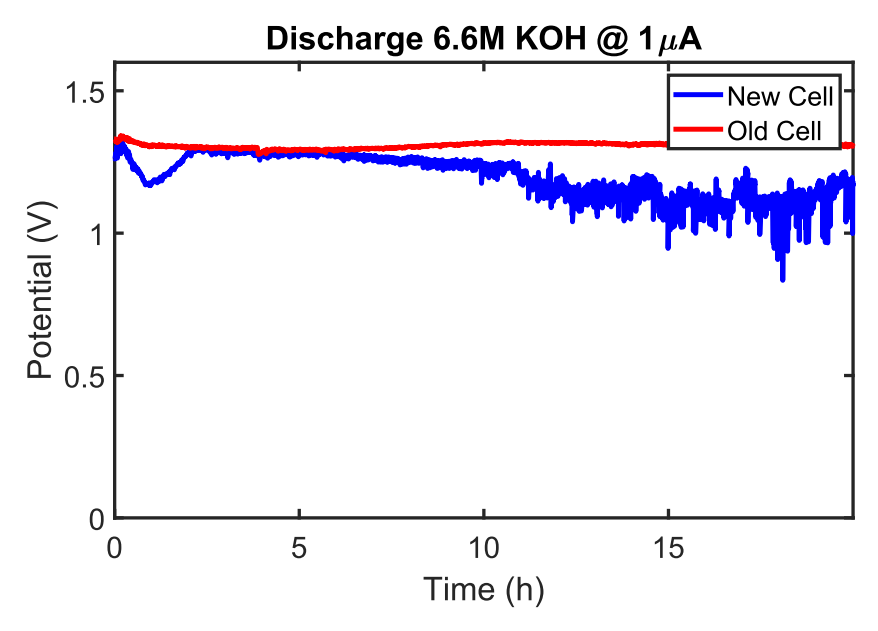


**Figure 4.7:** Presented in this figure are discharge plots for both battery designs when discharged at 1  $\mu$ A. The discharge using the new cell appears to have destabilized after 10 hours.

Shown in Figure 4.7 are two discharges carried out using the two different designs. Immediately seen is that for the new cell there appears to be a major destabilization of the discharge curve past the 10 hour mark. Furthermore, unexpectedly it appears that the old cell exhibits a higher discharge potential, despite the lowered resistances. This is hypothesized to be caused by the lowered volume of the electrolyte, as the surface area of the cathode is still the same, a larger portion of the electrolyte will be absorbed by the cathode, leading to a drop in the level of electrolyte present in the reservoir. Furthermore, identical leakage would lead to a larger fraction of the electrolyte leaking in the new cell.

Next the step heights and subsequently the masses are compared. The hypothesis being that the rate of corrosion is dependant solely on the concentration of the KOH, assuming at least sufficient liquid to cover the entire sample. Given in Figure 4.8 are the step heights for the two samples.

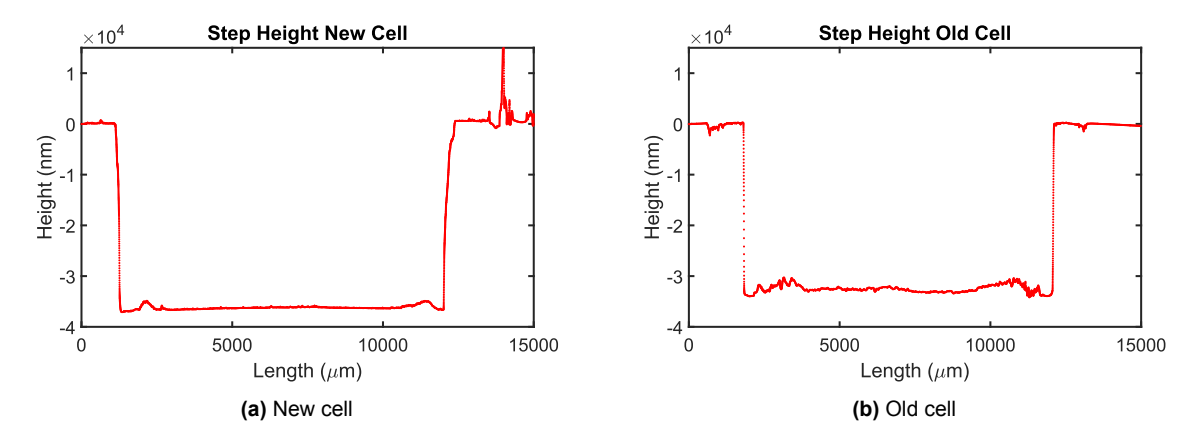


**Figure 4.8:** The step heights measured of the two samples discharged using the two different cell setups: (a) cell with anode-cathode distance of 0.8 cm, and (b) distance of 2.0 cm.

The step heights are determined to be  $36\pm2~\mu m$  and  $33.3\pm0.7~\mu m$ , respectively. Of note is

that though the discharge itself was 20 hours, the disassembly of both battery cells were done 4 hours later due to the lab being inaccessible for this period. This additional exposure time results in significantly higher step heights when compared to previous results.

The mass and error for the new and old cell are  $13.0\pm0.8$  mg and  $12.3\pm0.2$  mg, respectively. The higher error for the new cell is caused by the large positive spike on the right side of the graph. This result suggests that the sample in the new cell experiences more corrosion than the sample in the old cell. This is in contrast to the earlier hypothesis where the corrosion speed was thought to be independent of the distance between the two anodes. There is no clear indication what is causing this difference, however, it is speculated that in the new cell the KOH may have a slightly larger surface area due the new O-ring having the same outer diameter, but being thinner.

#### 4.2. RTIL characterization

Next the RTIL, BMPyr[NTf<sub>2</sub>], will be studied. As this RTIL has seen no prior use in this battery pair, the first experiment will be to ascertain whether or not this electrolyte will allow for a working battery. The steps afterwards will be to determine to what extent this RTIL functions when used as an electrolyte in a battery cell. Such as what are the discharge limits, currents and the associated potentials. The results of these tests will be given in the following subsections.

#### 4.2.1. Initial Test

The initial experiment to test the functioning of the battery is done in two parts. First an OCP measurement is done to find out what potential the battery can reach. Then a discharge at low current is carried out to characterize the battery. Figure 4.9 shows the OCP curves of si-air batteries using the above-mentioned RTIL. For one measurement the Si anode was exposed to an HF dip in order to ensure that any native  $SiO_2$  was removed.

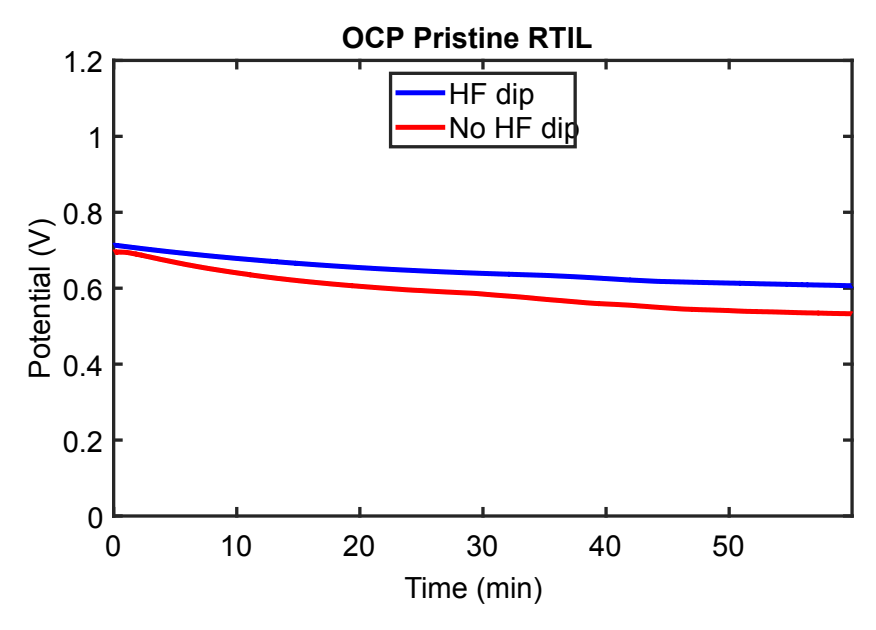


**Figure 4.9:** This figure displays the OCP when using a Topsil anode and the RTIL BMPyr[NTf<sub>2</sub>], there are two curves present, once where the anode is dipped into HF to remove the native oxide and once without.

Both anodes were held at OCP for 1 hour, during which a gradual decrease in potential was observed. This decrease is happening even while no discharge is occurring, implying that even at OCP some reaction carries on within the cell. Further, the sample which had no HF

dip did not show a major difference. The discussion chapter goes further into the reasoning why this result could have occurred.

Attempts were made to measure the weight and the step height of the sample before and after the OCP period, however, no discernible difference was observed using either the weight scale or the profilometer. Given that the Dektak is capable of measuring step heights in the order of 10 nm, this implies that the rate at which the RTIL corrodes silicon must be less than 10 nm per hour. This may indicate that using this RTIL there is hardly any parasitic corrosion.

#### 4.2.2. Boundary testing

After it had been established that a non-zero and measurable OCP was obtained with this configuration the question becomes at what current levels this battery will work. At this stage the RTIL has been used as obtained from the manufacturer, with an specified purity of 99.9%. To find out the relationship between the potential and the discharge current for this RTIL the battery cell has been constructed in a similar manner multiple times. The cell is discharged at escalating currents for 10 minutes at a time, taking care to remove the native oxide prior to any discharge. The following current levels were tested: 20 nA, 100 nA, 500 nA and 2.5  $\mu A$ . Shown below in Figure 4.10 are the discharge curves for these currents.

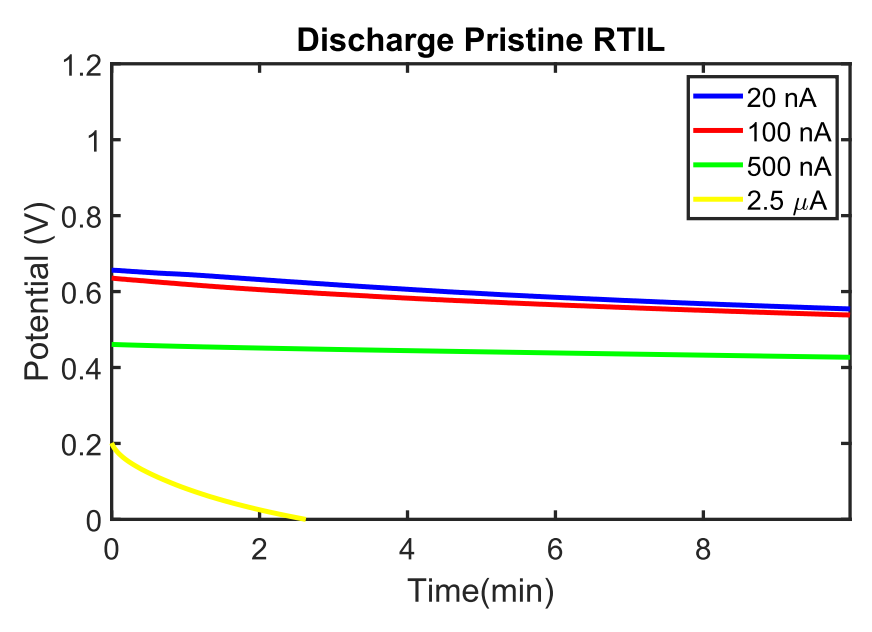


**Figure 4.10:** Plotted here are various potential curves, obtained for a set of discharge currents. The aim has been to keep all else equal and only the current has been changed. Pristine RTIL was used for these discharges.

It is seen in Figure 4.10 that the current decreases over time, with the fastest decrease observed for the 2.5  $\mu$ A discharge. This decrease in potential suggests that some limiting factor must be present, beyond the silicon itself, as with the chosen currents a 10 minute discharge cannot consume all of the silicon available.

#### 4.2.3. Limiting factors

In this section experiments will be presented aimed at finding out which component determines the decrease in potential over time. To do so the three components that make up the battery will be tested. This is done through a 20-minute discharge, where midway during the discharge two components are replaced and one is kept the same. The expectation is that if a component is limiting the discharge potential, even replacing the other two components the discharge curve

should continue where it was left off. Meanwhile if the component is not limiting it is expected that there will be a sharp discontinuity. The curves are plotted in Figure 4.11

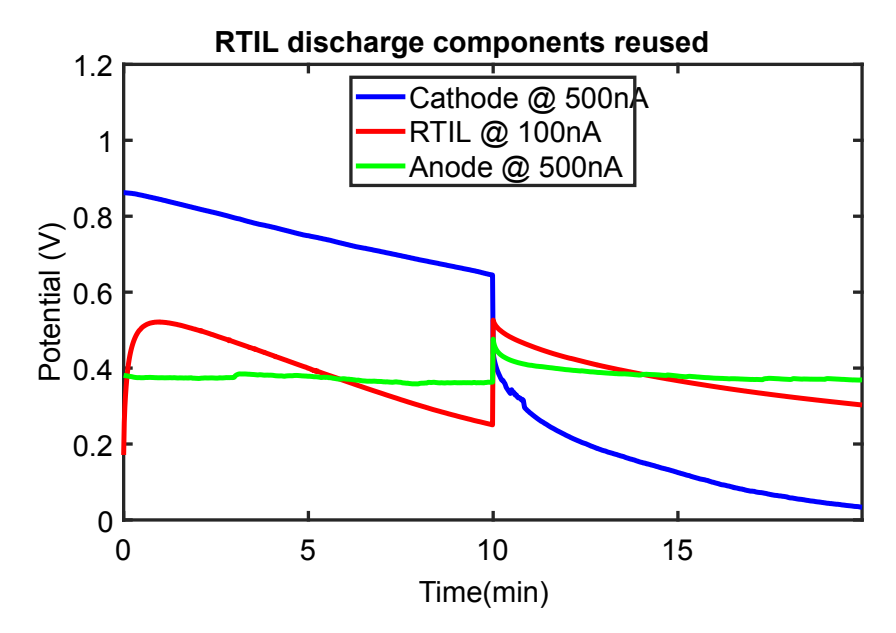


**Figure 4.11:** This figure presents three curves, each representing a different component being reused midway in a 20 minute discharge. The legend denotes which component was reused for which graph.

The curves in Figure 4.11 are classified as per the legend, where each curve consists of a 20-minute discharge experiment, where the discharge is stopped at 10 minutes to have components replaced. Not all components are replaced, however, and the legend shows which component is reused in that particular curve.

First considered is the curve in which the cathode is reused. This curve shows that at the 10-minute mark the potential experiences a sharp drop off. Following the earlier hypothesis this implies that the cathode is not the component that determines the discharge potential. Given that the anode and the electrolyte were changed at the 10-minute mark, one of these two components are suspected to be the limiting factor.

Second to be considered is the curve where the RTIL is reused and this curve shows that at the 10-minute mark the potential increases to approximately the same value as was found at the start of the discharge and showing a similar decreasing trend. Previously suspected was that the anode or the electrolyte is the limiting component, from this curve in a similar manner can be determined that the limiting component should be either the anode or the cathode. The common component between the two experiments then is the anode, implying that the anode determines the discharge potential.

To test this statement, is the third experiment, here it is seen that at the 10-minute mark there is a small spike in potential, however it quickly returns to the same value as before the 10-minute mark. This is in line with the hypothesis of the limiting component determining the potential and therefore even if the other two components are replaced, a similar potential should still be measured.

With this information, it is speculated that the anode heavily influences the discharge potential, as the great decrease in the potential seen in the curve where the cathode was reused could

be caused by the replacement of the anode. This is further supported by the difference in the starting potential between the cathode reused and the anode reused curves. Since they are discharged at the same current, with all the same components, the expectation is that the potential should start at the same level, however, the results do not show this. This inconsistency is further explored during the discussion.

#### 4.2.4. Comparing battery design

Similar to the two battery designs compared in Section 4.1.3 which used KOH as the electrolyte, an experiment was carried out to examine the differences between the two cells using RTIL. Unlike the experiment in Section 4.1.3 here the objective was to find out whether or not the distance and volume play a role in the potential. And hence, was carried out at OCP instead of 1  $\mu$ A. Though the shorter distance will also lead to a lower resistance, at OCP this resistance should not be of concern. Figure 4.12 plots the OCP for the two battery designs when using pristine RTIL.

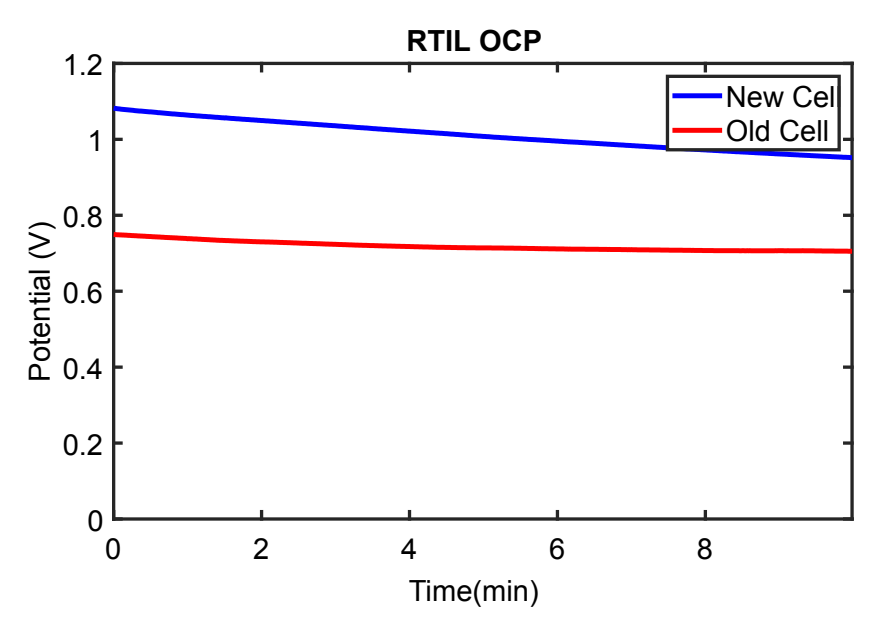


**Figure 4.12:** Plotted here are two 10 minute OCP measurements using pristine RTIL, one with the old battery cell and one with the new cell. This measurement has as result that the OCP of the new cell is higher than that of the old cell.

It can be seen in Figure 4.12 that the new cell exhibits a higher OCP. This observation suggests that the new battery design supports a higher OCP and in turn a higher potential during discharge, due to the shorter distance between the two electrodes. The result also suggests that the distance between the two electrodes does play a role, where a shorter distance has led to a higher OCP. With this result obtained, the decision was made to continue employ the new battery design during the RTIL experiments.

#### 4.3. KOH concentrations

Having done the initial testing on both KOH and RTIL now the main question addressed in this report is to be handled. Namely, how does conductivity influence the discharge. This is of interest for KOH as the results can be compared to the results obtained from RTIL, where the similarities and differences between the two electrolytes can be observed. Furthermore, Durmus et al. [37] has previously found the potential difference with varying conductivity to be greater than what can be explained purely through reduction in ohmic overpotential. This

experiment also seeks to reproduce this result.

First, results are shown when using KOH as electrolyte, where the conductivity is obtained using Equation 2.11. This equation is plotted for a temperature of 294.15 K in Figure 2.11.

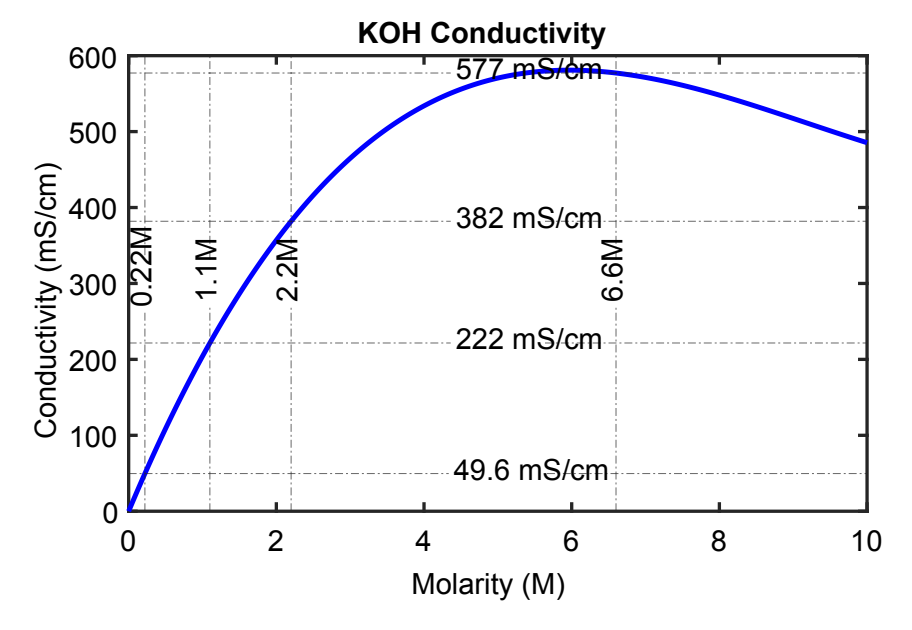


**Figure 4.13:** Plotted here is the conductivity of KOH as obtained from Equation 2.11 using T = 294.15 K. Vertical lines denote the concentrations which were used in this experiment, accompanying horizontal lines point to the conductivity.

Shown in Figure 4.13 are vertical and horizontal lines with molarity and conductivity values. These values correspond with the KOH concentrations used in the experiments.

The battery is discharged at a current of 1 and 50  $\mu$ A. Shown in Figure 4.14 are these two sets of discharge curves, where each set consists of the concentrations hightlighted in Figure 4.13.

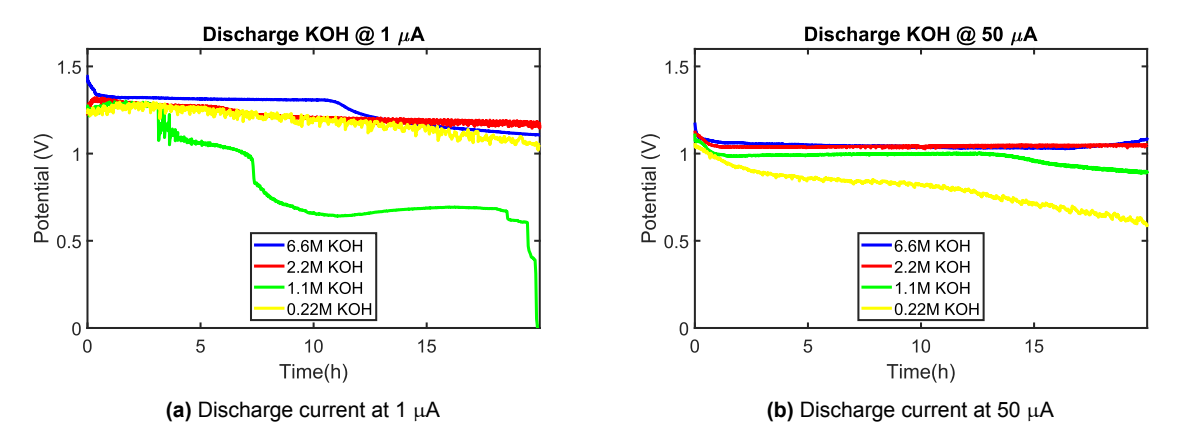


**Figure 4.14:** Displayed are two sets of discharge curves for varying KOH concentration. Displayed in (a) are the discharges at 1  $\mu$ A and in (b) those at 50  $\mu$ A. Notably the discharge curves on the left show erratic behaviour. Meanwhile the curves on the right exhibit stable behaviour, with sharper decreases in potential only occurring after more than 10 hours have past.

The discharge curves shown in Figure 4.14 using 1 μA current appear to exhibit more erratic

behaviour, with the 1.1M KOH discharge showing sharp decreases in potential as time progresses. Further, even the 6.6M discharge shows a dip around the 10 hour mark. In contrast, the 50  $\mu$ A discharge curves show stable behaviour for 6.6M and 2.2M KOH, with the 1.1M and 0.22M KOH showing a steady decline in potential.

The results show a decrease in potential for both currents which are in line with the expectation of decreasing concentration leading to lower potential, given the decreasing conductivity and the results demonstrated by Durmus et al. [37]. However, it is also seen that the potentials for the 50  $\mu A$  discharge are lower than those of the 1  $\mu A$  discharge. The potential found for the 50  $\mu A$  discharge approximately 1 V, lower than both the results found from Durmus et al. and Coerkamp [48], who have found potentials of 1.2 V and 1.1 V, respectively. It is speculated that given the consistent lower potential the decrease is caused by the equipment. The resistance of the electrodes and the attached wires was tested and found to be below 0.1  $\Omega$ , however, the resistance of the clamps and the accompanying wires connected to the Autolab were not.

These results suggest that the discharge using KOH becomes less stable at lower currents. Further, the results indicate that though a loss in potential is experienced when using lower KOH concentrations, this loss for 2.2M KOH is minimal when compared to 6.6M. For lower concentrations it does appear that the potential gradually decreases.

To observe the suspected effect of the conductivity on the potential more closely, the average potential of each measurement is plotted against their respective conductivities. Where the average is determined by dividing the sum of all data points by the number of data points in each measurement. This will be done for both discharge currents in Figure 4.15.

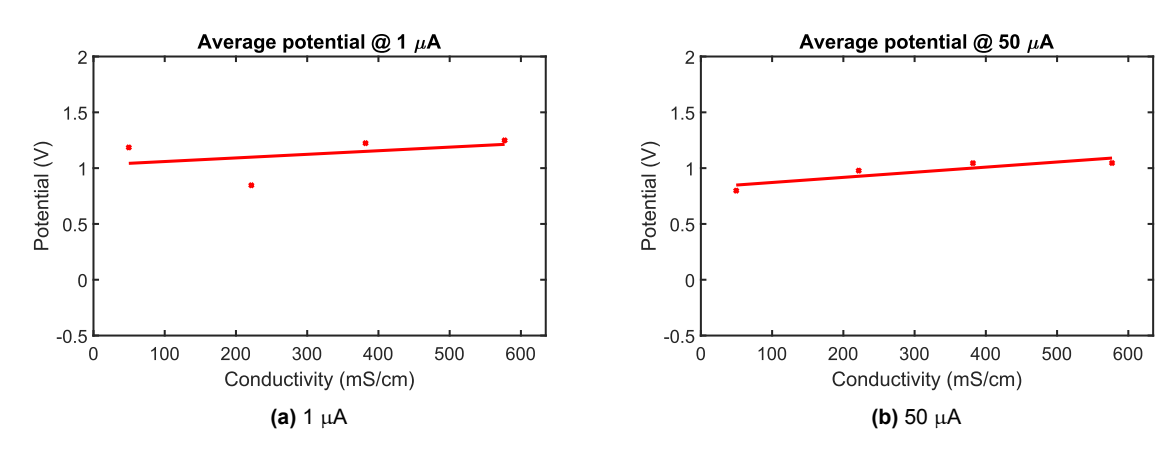


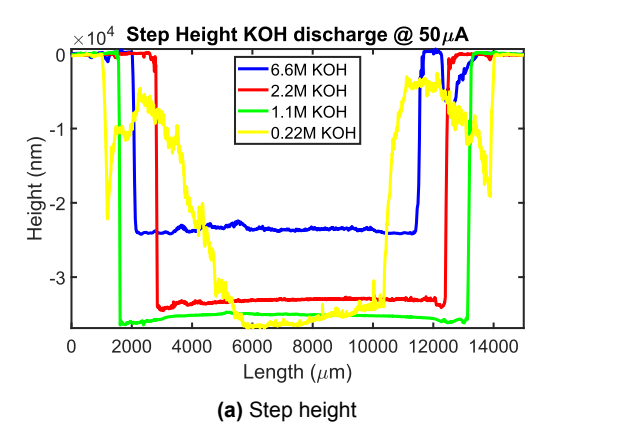
**Figure 4.15:** Given is the average potential plotted against the conductivity for a current of 1  $\mu$ A in (a) and 50  $\mu$ A in (b).

In Figure 4.15 are also plotted a first order polynomial fitted line through the points for each set of data. From these lines it can be observed that as conductivity decreases the potential also decreases. The fit for the data of the 50  $\mu A$  measurement points has as gradient 0.46 mV cm/mS. Similarly for 1  $\mu A$  an gradient of 0.32 mV cm/mS.

Using Ohm's law, with  $R=\frac{l}{\sigma A}$ , and a current of 1  $\mu$ A, a distance between electrodes of 2 cm and an active area of 1.6 cm², the expected potential loss between 577 mS/cm and 50 mS/cm would be approximately 23  $\mu$ V, significantly lower than measured here. As in Ohm's law the current and voltage have a linear relationship, the voltage loss for the 50  $\mu$ A discharge

would be expected to be approximately 1.1 mV, which is also significantly smaller than measured. A similar result was found by Durmus et al. [37] where it was speculated that the reaction kinetics played a large roll in the decrease of potential and the conductivity only contributing a small amount.

To observe whether or not this lowered concentration also decreases the total silicon consumption rate the step heights for the 50  $\mu$ A are shown together with the calculated mass in Figure 4.16.



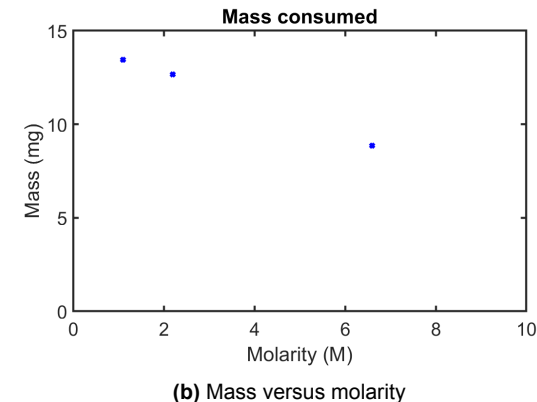


**Figure 4.16:** Shown here are in (a) the step heights obtained from the samples discharged with KOH at 50  $\mu$ A and in (b) the corresponding mass, obtained using the method described in Appendix A.

The results shown in Figure 4.16 suggest an increase of silicon consumption as the concentration is lowered. The step height measurement from the 0.22M KOH sample differs from the other three measurements, showing uneven surfaces and therefore no mass calculation was able to be performed. The other three measurements have an average step height of  $23.8\pm0.72~\mu\text{m},~33.9\pm0.6~\mu\text{m}$  and  $36.1\pm0.53~\mu\text{m}$  for the concentrations of 6.6M, 2.2M and 1.1M, respectively. Using Equation A.2 the mass can be determined from these step heights. These masses are  $8.9\pm0.3~\text{mg}$  for 6.6M,  $12.7\pm0.2~\text{mg}$  for 2.2M and  $13.4\pm0.2~\text{mg}$  for 1.1M.

From the results of Durmus et al. [37] it was found that the etching rate of silicon reaches a maximum around a KOH concentration of approximately 6M, with total rate of silicon consumption decreasing at higher and lower concentrations. There are differences between the setup used here and that of Durmus et al. [37] however. Here the KOH was supplied at the beginning and left during the discharge, in contrast Durmus et al. [37] employed a pump. This pump has led to two differences, firstly the KOH would be refreshed over time as there is a flow in the system and secondly the KOH level in the system would remain constant. Further the KOH volume and the active area in this report are significantly higher than that used by Durmus et al. [37] at 4 ml compared to 0.6 ml and 1.6 cm² compared to 0.44 cm², respectively. The results here suggest that the 1.1M KOH discharge experienced the greatest corrosion speed, the link between the noted differences and this increased corrosion speed is as of yet untested.

The step heights from the 1  $\mu$ A samples are covered in the next chapter, as those exhibit large surface roughness, to a greater degree than even the 0.22M measurement at 50  $\mu$ A. Of note is that for the 1  $\mu$ A samples the step height is highest for the 6.6M KOH discharge in contrast to the results found for the 50  $\mu$ A discharge. The results indicate that the combination of low KOH concentration and high discharge current result in a higher total amount of silicon consumed.

#### 4.4. RTIL water mixing

Delisari et al. [39] demonstrated the use of the RTIL BMPyr[NTf<sub>2</sub>] in a zinc-air battery pair showing increased discharge potential and stable current when water was mixed into the RTIL, attributed to an increased conductivity and an alteration of the zinc surface.

To test this for Si-air, the following experiments were done. The battery was constructed using the new cell design, using RTIL of three varying concentrations, namely pristine, 1wt% water and 3wt% water. Higher water content was attempted, however, unlike Delisari et al. [39] mixtures containing 5 wt% water and higher experienced breakdown of the emulsion in less than 10 minutes and thus no consistent discharges could be carried out. The conductivity of these three mixtures was also measured using a conductivity meter, which has an error of 0.3% of the measurement range, with this range being 20 mS/cm during the measurements. With the results shown in Table 4.1.

**Table 4.1:** Shown here are the conductivities of the RTIL as measured using the conductivity meter. Also given is the temperature of the conductivity during the measurement.

Water wt%	Conductivity (mS/cm)	Temperature (K)
0	$\textbf{2.2} \pm \textbf{0.06}$	293 ± 1
1	$2.6\pm0.06$	$292\pm1$
3	$3.0\pm0.06$	$293\pm1$

Table 4.1 shows that indeed the conductivity is increasing with the water concentration. With this information obtained, the next step would be to discharge the battery using these mixtures. The discharges were done in a similar manner to previous experiments, where now there is a varying electrolyte, through repeating the experiments for each mixture with multiple currents a picture is painted of the behaviour of this RTIL. These discharge curves can be found in Figure 4.17.

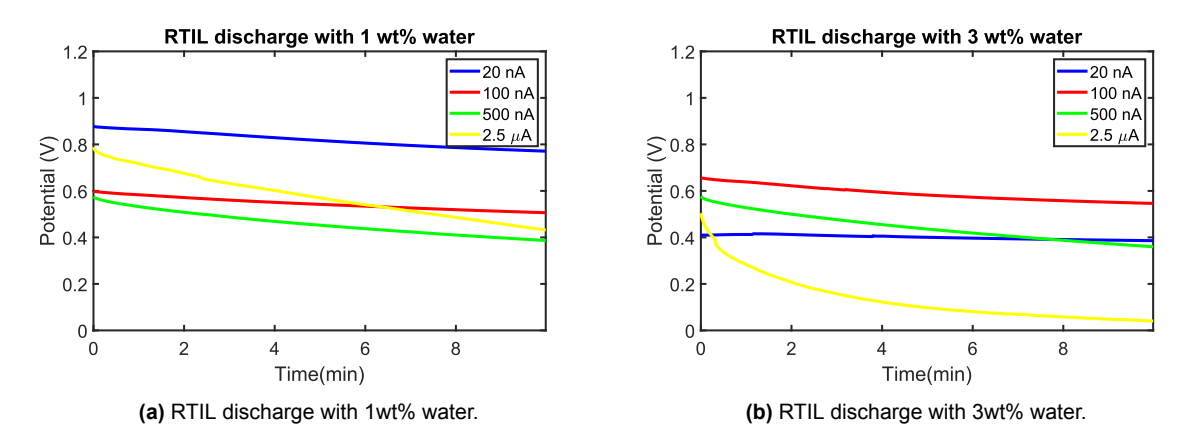


**Figure 4.17:** Shown here are two sets of discharges using RTIL mixed with water. On the left hand side with 1wt% water and on the right hand side with 3wt% water. Each set has 4 discharges at varying currents, these being 20 nA, 100 nA, 500 nA and 2.5  $\mu$ A

Shown here in Figure 4.17 are the discharge curves using 1 wt% water and 3 wt% water. Figure 4.10 shows the pristine RTIL behaviour. Comparing these three graphs it becomes noticeable that the discharge graphs with water show inconsistent behaviour. An example of this inconsistency is the behaviour of the 20 nA discharge, which in the 3wt% RTIL exhibits a lower potential than the higher current discharges. In contrast the opposite is true when considering the pristine and 1wt% water RTIL discharges, where the 20 nA discharge exhibits

the highest potential.

Figure 4.18 displays the average potential, obtained again by dividing the sum of all data points for the potential by the total number of said data points, versus the conductivity for the measurements of Figure 4.17. In this manner it is attempted to see if there is a correlation between the conductivity and the potential.

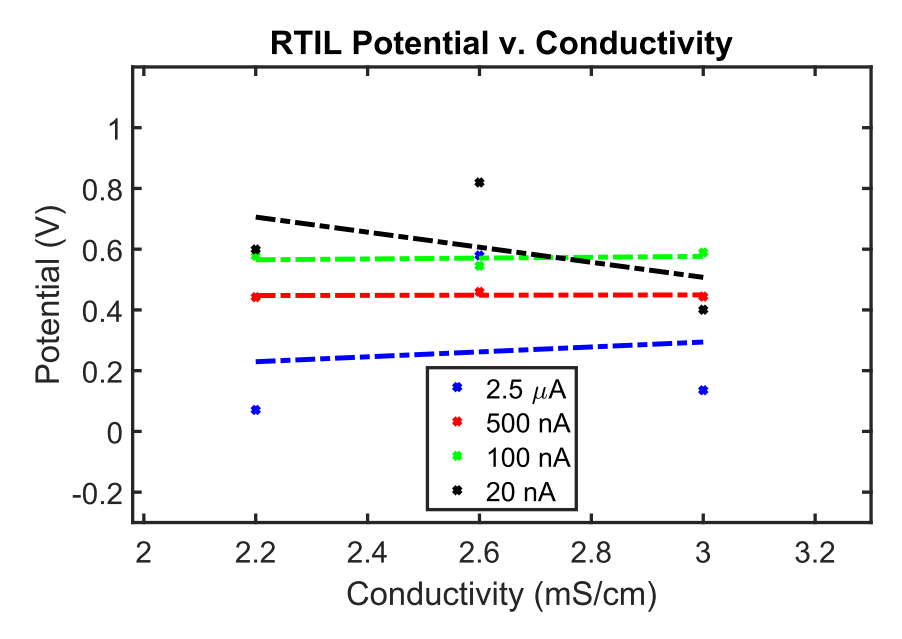


**Figure 4.18:** Plotted in this figure are the average potential of the measurements from Figure 4.17 against the conductivity of each measurement. Additionally given are first order polynomial fits to the data points.

Seen in Figure 4.18 is that the fitted potential shows a decreasing trend for three of the currents, however for 20 nA the potential instead is rising. Furthermore, it can be seen that of the four currents, which current provides the largest potential changes. Unlike for KOH as shown in Figure 4.15 where the potential decreases with the conductivity for every measurement.

Previously in Section 4.3 it was mentioned that the potential decrease found in the KOH measurements cannot be solely due to the conductivity. The same is the case for the RTIL, as the current used here lies between 20 nA and 2.5  $\mu$ A. At these currents and the range of conductivity the drop in potential would at most be 0.2 mV, using a distance between electrodes of 0.8 cm. Due to this no clear relationship between the conductivity and the discharge potential for the RTIL can be determined.

## 5 Discussion

This chapter will discuss the results presented in the previous chapter. In Section 5.1 battery cell will be discussed, followed by Section 5.2 that focuses on the use of KOH and Section 5.3 on the Room Temperature Ionic Liquid (RTIL).

#### 5.1. Battery cell

This section will discuss the bending of the anode encountered during step height measurements as well as the inconsistent native oxide presence found during the experiments.

#### 5.1.1. Inconsistent Native Oxide

During the experiments presented in this report an inconsistency in the native oxide layer was encountered. Silicon when freely exposed to air forms a thin oxide layer. This oxidation process is self limiting and will lead to a native silicon oxide layer with a thickness of 2.1 nm, which is reached within 10 hours [78]. The inconsistency encountered is that in the samples used in this report, this layer is not always present even though some samples were prepared and left exposed to the air for more than two weeks. Figure 5.1 shows pictures of a series of samples after being dipped into water. The samples were stored in a CD holder and no special care was taken to store said CD holder in a controlled environment. Nor were the samples cleaned prior to dipping into the water.

5.1. Battery cell 53

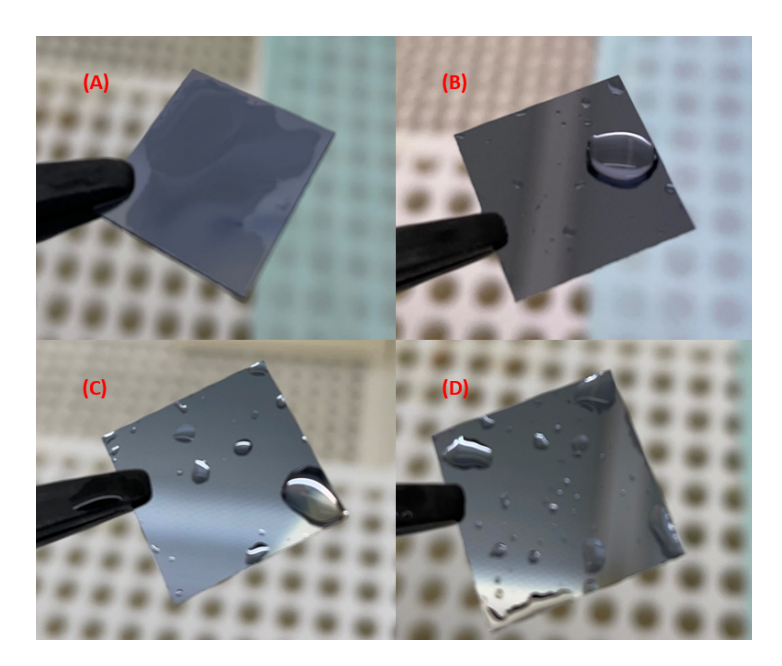


**Figure 5.1:** This picture shows four samples taken from the CD holder at random. They are each submerged in water and then taken out and flipped horizontally such that a picture may be taken. The residual water on sample A is clearly different when compared to samples B, C and D. Where in A the water is diffused over the entire surface, meanwhile in B, C and D they form distinct droplets.

Using the fact that silicon is hydrophobic and  $SiO_2$  is not, it can be concluded that three of these four samples, B, C and D, suggest no  $SiO_2$  to be present, as the remaining water on the sample forms distinct droplets. Meanwhile on sample A instead the water is diffused over the surface. The expectation would be that the four samples should show similar behaviour in terms of native oxide growth. A possible explanation for this difference is the exposure to air requirement for the native oxide to grow. It is possible that, though unintended, the storage of the samples was such that no air was able to reach some of the samples. This could be caused by the samples being stacked on top of each other, with the silicon side facing each other, which is speculated to have prevented the silicon from being exposed to the air.

Knowing this, some measures should be taken in future experiments if an electrolyte is to be used that does not innately remove the native oxide. Namely, the samples should be submerged in water before every measurement to ascertain whether or not native oxide is present. This is especially important when doing experiments where the presence of native oxide is desired. It is during such experiments that this inconsistency could cause an assumption that samples that have been stored and exposed to air for more than a week would naturally have an oxide layer to be wrong.

#### 5.1.2. Curved Anode Samples

During the measurement of the step height bending of the sample was encountered. This bending introduces a loss of accuracy when considering small step heights such as those expected to occur when discharging with RTIL and when discharging KOH for short periods of time. An example of this curvature can be seen in Figure 5.2, where the step height was measured for an unused anode sample.

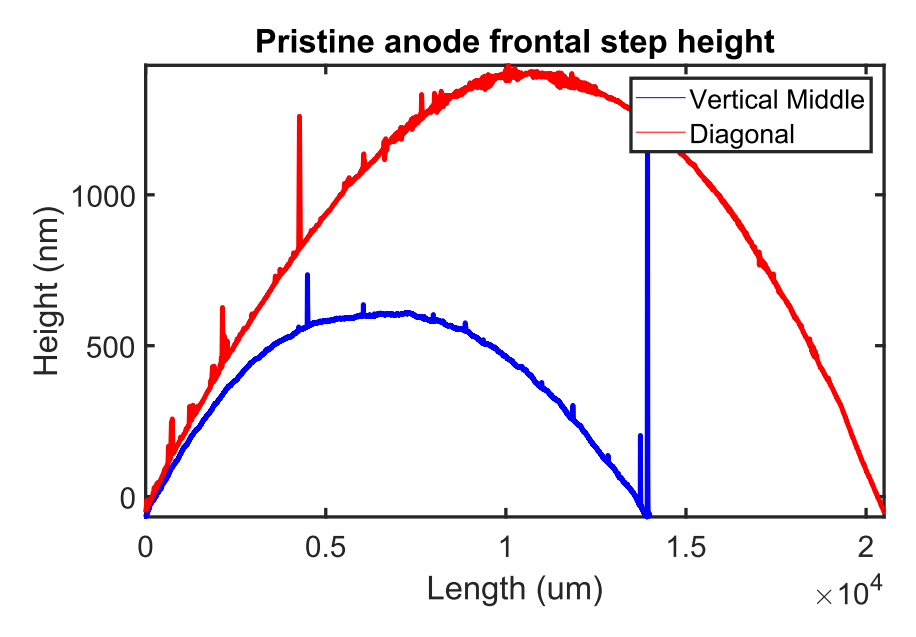


**Figure 5.2:** Step height of an unused anode. Two graphs are included, one going vertically across the middle of the sample and one going diagonally across the sample. Both measurements were done on the same side of the sample. The vertical middle measurement has a major spike on the right side of the graph, likely caused by surface contaminants.

As seen in Figure 5.2 there is a curvature present. This curvature is most pronounced when measuring the step height corner to corner in a diagonal manner. This suggests that the samples are curved the most at the corners in comparison to the center. The cause is yet unknown, however it is speculated to be caused by the laser cutter. The laser cutter introduces heat into the unbroken wafer, it is possible that during this time the wafer is curved slightly. It also makes sense why the corners would see the greatest deformation, as the laser would pass over the corners twice as often as compared to the sides of each sample.

#### 5.2. KOH

In this section the results obtained while using KOH as the electrolyte are further discussed. Handled will be the OCP period and the corrosion experienced by the anode during tests which use KOH, the leakage which occurs and the evaporation of the KOH when left exposed to the air.

#### 5.2.1. Corrosion & OCP period

First to be discussed is the corrosion of both the silicon and the silicon oxide surface layer, and the associated OCP period. From Coerkamp [48] it was found that KOH at 6.6M concentration can corrode  $SiO_2$  at a rate of 3.4 nm/hour. Given that any native oxide layer growth is self limiting and peaks at 2.1 nm, this implies that even for a sample left exposed to air for a long time, at most a single hour would be sufficient to remove any native oxide. This is why the OCP period is applied, as it allows the KOH to remove any native oxide layer that has formed, and as there is no discharge, no new layer is created either.

During the experiments performed by Coerkamp [48] the OCP period exhibited a low initial potential, which increased to a higher value of 1.3-1.4 V value after approximately 40 minutes, coinciding with the theorized removal of the SiO<sub>2</sub> layer. However, the results presented in this report, suggest that does not happen. Instead, the OCP is measured to be immediately at a value of 1.3-1.4 V, similar to the results of Durmus et al. [37] who have used argon/sulfur hexa-

fluoride plasma to remove surface oxides prior to measuring. This can be seen in Figures 4.1 and 4.3. In fact, instead of a jump in the OCP at the 40 minute mark, the OCP appears to be gradually decreasing over time.

The absence of a decreased potential at the beginning of the discharge suggests that there is no native oxide layer present, which as mentioned in the previous section could be caused by way the samples were stored. The fact that native oxide interferes with the battery discharge however is exhibited clearly in literature, such as in the results obtained by Coerkamp [48].

Additionally, to further emphasize the irregularity regarding the native oxide layer is Figure 5.3. This figure displays a OCP plot using 6.6M KOH.

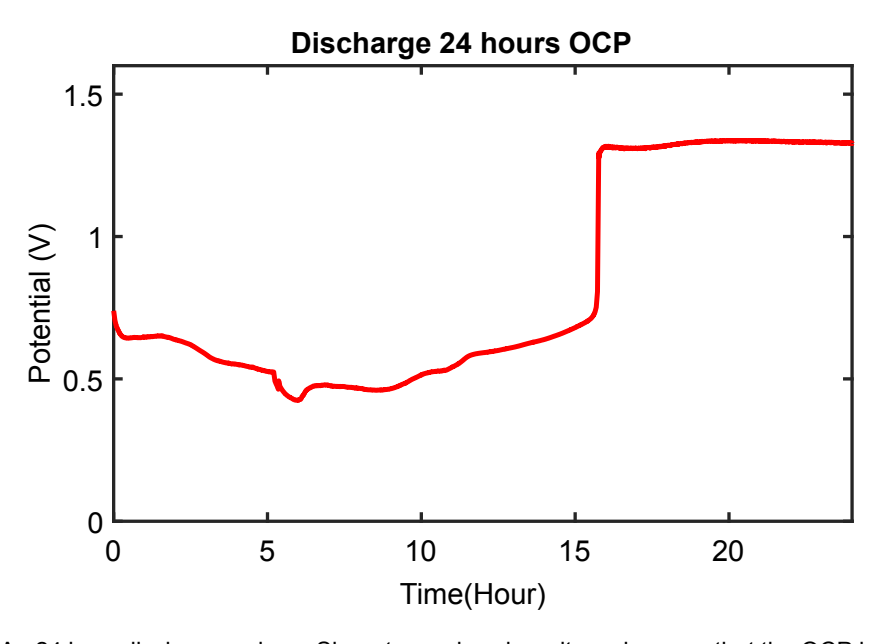


**Figure 5.3:** An 24 hour discharge using a Siegert sample, where it can be seen that the OCP is of a low value up until 15 hours into the measurement, unlike the expected value of 40 minutes.

In Figure 5.3 the duration in which the potential is below the expected value of 1.3-1.4 V is significantly longer than the 40 minutes found by Coerkamp [48]. As 6.6M KOH was used the etch rate of 3.4 nm/hour is a good approximation. With this knowledge the results suggest a far thicker layer of SiO<sub>2</sub> was present on this sample, in the order of 50 nm. It is uncertain why this thicker layer of SiO<sub>2</sub> is present however, as native oxide thickness reaches a maximum at 2.1 nm. Silicon oxide can be grown to greater thicknesses than 2.1 nm, however this does not occur naturally. An example of such growth is thermal oxidation, where by introducing heat to the sample a silicon oxide layer may be grown. Thermal oxidation for silicon is done at high temperatures of 1000-1600 K [79]. A layer of 50 nm thick  $SiO_2$  would take over an hour to grow at temperatures of 1200 K [79]. This is unlikely to be caused by the laser cutter as the sample was safe to touch within 5 minutes after the laser is finished cutting, for a 50 nm layer to be grown within 5 minutes a temperature of upwards of 1400 K is necessary. Given the specific heat capacity of silicon of 0.7 J  $g^{-1}$  k $g^{-1}$ , a wafer diameter of 10 cm, thickness of 285  $\mu$ m and the laser power being 20W, assuming no loss of heat due to convection during the process the laser would need 200 seconds of sustained operation to heat the silicon sample to the required temperature. This is over double the amount of time the laser would be in operation during the cutting process.

When repeating experiments using this setup, care must be taken to ensure that the samples are free of  $SiO_2$ . If the removal is done using HF, it must be noted that the aluminium back contact is also corroded by HF. In particular, should a layer as thick as the one shown in Figure 5.3 be present, removing the  $SiO_2$  with HF will imply a long exposure time and in turn cause the aluminium to be fully etched away as well. In such a case replacing the sample is the better decision.

Finally considered during this section is the inconsistent corrosion of the sample during certain discharges. The expectation during this report has been to find flat surfaces when scanning the step heights, supported by the findings of Coerkamp [48]. Shown below in Figure 5.4 are the step heights obtained form a series of 1  $\mu$ A discharges.

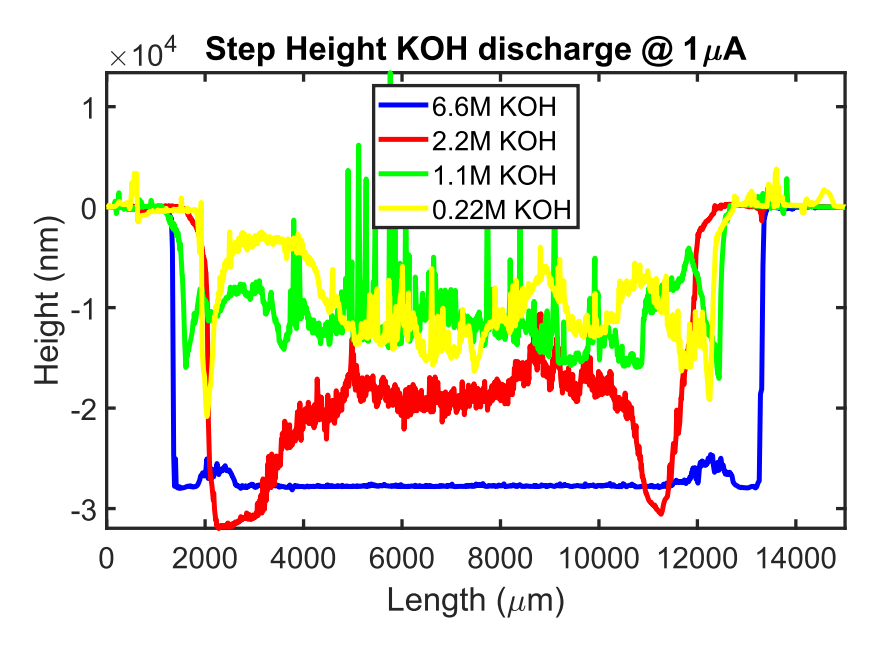
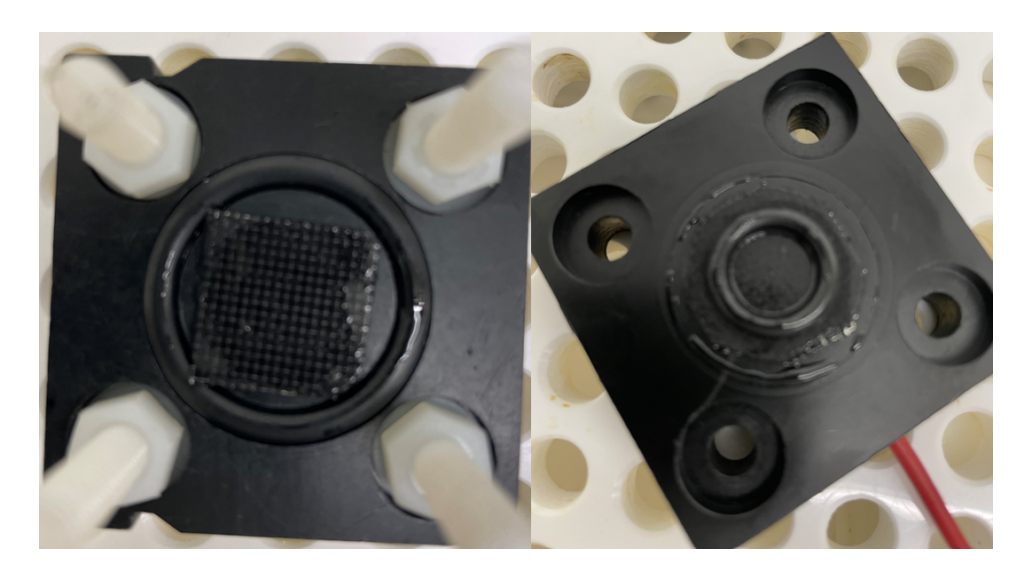


Figure 5.4: The step heights measured for the discharges done at a current of 1  $\mu$ A. Notable is that with exception of the 6.6M KOH discharge, the step heights are highly erratic, where a flat plane was expected.

Seen in Figure 5.4 is that the step height appears to be irregular for lower KOH concentrations. Through testing using acetone and HF it was determined that these irregularities were not caused by either carbon deposition from the cathode or SiO<sub>2</sub> deposition from discharging. It is as of yet unknown what the precise cause of these irregularities is, but from the result they appear to occur when discharging at a low current with a low KOH concentration. Durmus et al. [37][60] report that the anisotropic etching, that is different etching rates depending on orientation of the silicon, of KOH may be the cause for uneven etching. Where for low concentrations of KOH this anisotropic behaviour is more pronounced and thus visible.

#### 5.2.2. Leakage & Evaporation

A consistent phenomena with using KOH and to a lesser extent RTIL, due to the higher viscosity, has been the tendency of the electrolyte to leak through the cathode. This is caused by the cathode being porous, which when in contact with either electrolyte for long periods will become saturated to the point where the liquid will start to seep through. For the KOH this is undesirable as it will start to corrode the electrodes. Figure 5.5 shows a set of pictures in which this leakage can be observed.



**Figure 5.5:** Shown here are a set of pictures showing leakage. On the left side is shown the backside of the cathode being wet. And on the right is seen liquid surrounding the cathode, outside of the smaller O-ring.

As can be seen in Figure 5.5 there appears to be liquid surrounding the cathode. Furthermore, it can be seen that the backside of the cathode is glimmering from absorbing the electrolyte. Both of these indicate that the liquid electrolyte is not being completely contained within the reservoir, as otherwise only the area within the small O-ring would be wet.

Another aspect of using KOH as the electrolyte is the evaporation rate. The KOH when used as electrolyte for longer discharges will find itself evaporating while exposed to air. A solution has been attempted to use a cap to lessen this exposure, however from the results it appears that adding this cap exacerbates the leakage problem. This report proposes that this is caused by the corrosion reaction, which has as product hydrogen gas, by sealing one of the openings of the battery this gas is forced to exit through the remaining openings, which in turn may have effectively pushed the electrolyte through the cathode faster. The battery cell after discharge when using a cap to seal off the central reservoir is shown in Figure 5.6.

5.3. RTIL 58

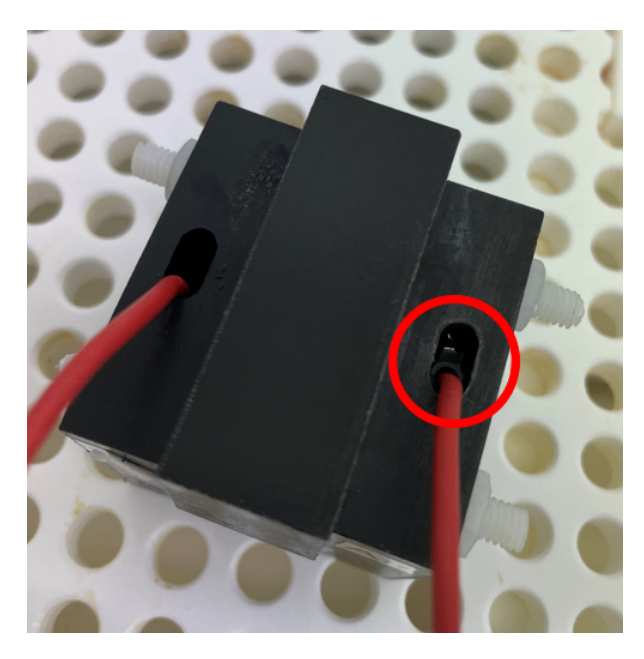


**Figure 5.6:** Displayed in this picture is the battery cell after a 20 hour discharge using KOH. During this discharge a cap was placed on the battery cell to seal off the electrolyte inlet. Encircled is the cathode holder where liquid is visible.

Figure 5.6 shows the battery cell after a 20 hour discharge with KOH, using a Teflon cap to seal off the central segment. On the figure is encircled the opening of the cathode holder, through which the wire connected to the PCB exits. It is seen that there is liquid in this opening which can only have come from the central reservoir during the discharge. Due to this, capping off the central segment is not a viable method of reducing the evaporation rate of the KOH.

#### 5.3. RTIL

In this section the results where the RTIL, BMPyr[NTf<sub>2</sub>], was used will be further discussed. In particular miscibility of the RTIL and the reproducibility of the results obtained using it will be discussed. Further discussed is the low discharge current achieved using the RTIL.

#### 5.3.1. Miscibility & Reproducibility

A major complication encountered during the experiments using BMPyr[NTf<sub>2</sub>] as the electrolyte was its a-polar nature. As one of the experiments called for mixing with water, this led to issues. The RTIL does not mix with water due to being a-polar, furthermore, it does not create a long lasting emulsion either when mixed. As the experiments called for no more than 3 wt% water added to the RTIL, mixing would only create a thin layer of water bubbles at the surface of the RTIL, which will when left alone separate quickly, with full separation within 20 minutes. Figure 5.7 shows a picture of the mixed state of this RTIL with water.

5.3. RTIL 59



**Figure 5.7:** Presented in this figure is a picture of the RTIL, BMPyr[NTf<sub>2</sub>], being mixed with water. Note that due to the a-polar vs polar interaction an emulsion is created, but only at a thin layer near the surface due to the imbalance in the two liquid quantities and densities.

The difficulty with mixing these two liquids present a problem, as the emulsion is created on the surface layer of the RTIL pouring the RTIL into the battery will not lead to the intended wt% being present. Furthermore, due to the water remaining on the surface of the RTIL a second problem occurs, namely the water is still in contact with the surrounding air, leading to evaporation. This is problematic due to the RTIL not experiencing such evaporation, and as such as time passes the concentration of water in the mixture will gradually decrease.

In addition to this, there are problems of reproducibility even when using pristine RTIL. Where the measurements return inconsistent results. This is shown in Figure 5.8 where a series of discharges were carried out at a constant current using pristine RTIL.

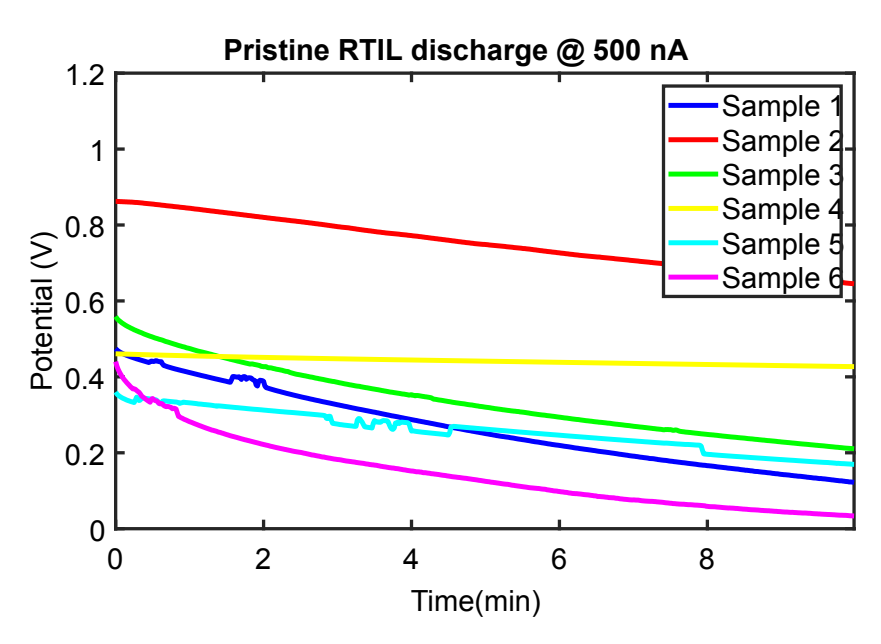


Figure 5.8: Given here are a series of discharges where a constant current is maintained.

5.3. RTIL 60

Here in Figure 5.8 a series of discharges are carried out using pristine RTIL at a constant current. Yet as can be seen, unlike what is expected, the results vary between each experiment. Combining this set of results in which consistently the entire battery cell was replaced with the results obtained previously in Section 4.2 a hypothesis may be arrived at, in which the anode samples influence the potential. This due to each of these measurements showing different starting potentials, but during the discharge using the same anode twice, the potential remained the same.

#### 5.3.2. Low Current

Discussed next is the current with which the RTIL has been working with. As seen in the results the RTIL shows a decline in potential over time, with the slope of the decline generally increasing as the current does. This has as a consequence that the battery using this RTIL can only be discharged at low currents, of less than 2.5  $\mu A$ . This low current makes it difficult to determine the efficiency, as this is calculated from the mass consumption, however, the mass consumed during the discharges using RTIL is lower than the error range of the scale. Assuming 1 electron per 1 silicon atom and a surface area of 1.6 cm² a discharge current of 2.5  $\mu A$  for 1 hour would at most result in a step height of 14 nm. The Dektak has an error in the order of 10 nm, and so would be unable to accurately detect this. Seen next in Figure 5.9 is an example of this step height being undetectable.

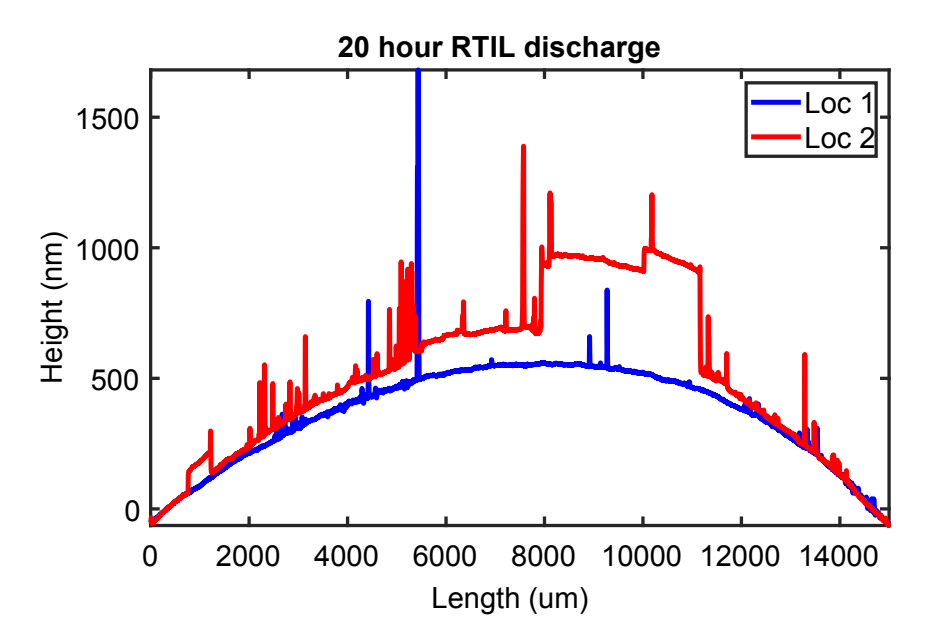


**Figure 5.9:** Seen here is the step height at two random locations of an anode discharged with RTIL for 20 hours at a current of 100 nA. Note that as the RTIL does not passively corrode Si, any consumption of mass is solely linked to the discharge. The curvature of the sample and the spikes in the sample make determining a step height impossible.

Figure 5.9 shows the step height of an anode discharged while using RTIL as electrolyte, note the similarity to the step height sample of a pristine anode as seen in Figure 5.2. With this knowledge, the mass consumption during RTIL discharge is not measurable with the currently used tools.

# 6

## Conclusion

The objective of this report is to determine the relationship between the conductivity of the Room Temperature Ionic Liquid (RTIL) 1-butyl-1-methylpyrrolidinium bis(trifluoromethyl-sulfonyl)imide (BMPyr[NTf<sub>2</sub>]) and the discharge characteristics of Si-air batteries. To do so multiple discharge experiments were carried out using this RTIL as the electrolyte. Further, to compare the behaviour of the novel RTIL with that of the more established KOH additional experiments using KOH have also been carried out where the conductivity was varied through usage of concentration variations. In this chapter the conclusions obtained in this report are summarized and recommendations are given for further research.

#### 6.1. Conclusions

First discharge experiments with KOH were carried out, this was done to build familiarity with the equipment and test if the set up as devised produces reproducible results. To do so the battery cell was discharged for varying lengths of time and the potential and Si consumption were compared.

After the first KOH experiments, the viability of the chosen RTIL to function as an electrolyte was tested. This was done through galvanostatic discharge experiments using a similar setup was done using KOH. From these experiments it was found that using this RTIL the battery cell discharges, with currents tested up to  $2.5~\mu A$ .

Next considered were the limitations in using this RTIL, where the aim was to increase the understanding on what the discharge limits were for this electrolyte. This was done through a 20-minute discharge during which at the halfway mark two of the components are replaced, the component that remains is the one of interest. From this it was found that reusing the electrolyte and the cathode results in large discontinuities in the potential, speculated to be caused by the anode being changed. Reusing the anode, however, finds the potential remaining constant. The tentative conclusion reached here is that the anode determines the potential and is limiting the discharge. However, a precise relationship between anode state and the discharge potential has not yet been found.

Subsequently, in this report discharges of the battery using both KOH and RTIL with varying conductivities are presented and discussed. These varying conductivities were obtained for the KOH by varying the concentration and for the RTIL by mixing water into the substance. In this manner the RTIL has seen a modest conductivity range between 2.2 mS/cm to 3.0 mS/cm. Meanwhile the KOH has seen a substantial conductivity range from 49.7 mS/cm to 577 mS/cm. The conductivity for the RTIL was measured using an conductivity meter, mean-

while the conductivity of the KOH was obtained through an equation.

From these discharges it was found that for KOH lowering the conductivity sees a lowering of the potential as expected. With fitted gradients having found a decrease of 0.46 mV per 1 mS/cm for the 50  $\mu A$  discharge and an decrease of 0.32 mV per 1 mS/cm for the 1  $\mu A$  discharge. However, the lowering of the potential is greater than what can be explained by only the ohmic overpotential, which following ohm's law is not expected to be larger than 1.8 mV and 40  $\mu V$ , for 50 and 1  $\mu A$ , respectively. Further, unstable discharge and leakage was encountered. In particular at low KOH concentrations and low currents the discharge using KOH becomes unstable, possibly caused by anisotropic etching of the silicon anode.

Meanwhile for the RTIL discharges it was found that the reproducibility is low, caused by a combination of factors. First there is the miscibility of the RTIL with water. Due to the RTIL being a-polar an emulsion is created during the mixing, however, this emulsion breaks within 20 minutes and complicates measurements. Second is the low current at which this RTIL discharges, with the maximum being at 2.5  $\mu A$  this leads to reduced accuracy and outside interference being proportionally higher, when compared to the maximum discharge current tested using KOH in this report, that being 50  $\mu A$ . When plotting the potential of the RTIL at varying discharge currents against the conductivity, the results indicate that a decreasing conductivity increases the potential when discharging at 20 nA. For the remaining discharge currents at 100 nA, 500 nA and 2.5  $\mu A$  the potential decreases with the conductivity. Similar to the KOH case the ohmic overpotential cannot fully explain this decrease and increase in the potential. As with the used discharge currents at the very most an drop of 0.2 mV is expected, using an electrode distance of 0.7 cm.

Unfortunately, the conclusion of this report is that with the current results, no conclusive relationship between the conductivity of the RTIL and the discharge potential can be determined yet. The results suggest the potential is also influenced by other factors than only the conductivity. It is established that if any parasitic corrosion is occurring with this RTIL, it is at a rate slower than 10 nm/h.

#### 6.2. Recommendations

This section covers a series of recommendations for further research into this subject. These recommendations will be given in the format of a list of bullet points, with no order of importance.

- During discharge of the battery using RTIL mixed with water as the electrolyte the emulsion breaks over time. In a future experiment it is recommended to place the battery cell on a vibrating table or insert a mixer into the electrolyte container so that this breaking of the emulsion can be prevented
- During the discharge of the battery using KOH evaporation of the electrolyte was occurring. This may influence the measurement if the loss in electrolyte is large enough that the surface of the anode is no longer fully in contact with the electrolyte. The recommendation is to increase the volume of the electrolyte, but not opening size or the active area, so that a larger amount of reserve electrolyte is present.
- While working with RTIL this report has found that the results using it have a low reproducibility. This report has not managed to pinpoint what aspect of the discharge has causes this. During this report the anode, the cathode and the electrolyte were looked at. Of these the anode appeared to have the greatest influence on the discharge potential, however no clear relationship was established. As such the recommendation,

- should further experiments with this RTIL be attempted, is to look further into the anode behaviour, through for example examining the anode underneath a microscope
- This report has so far only used <100> n-type doped silicon wafers, with doping concentration in the order of 10<sup>15</sup> dopants per cm<sup>2</sup> using an aluminium back contact. As the RTIL used in this report was based on its prior use in Zn-air batteries and the similar work functions of doped silicon and zinc, where zinc has an work potential between 3.73 and 4.33 eV depending on the zinc structure. Higher n-type doped silicon has a lower work function, moving further into the zinc range, and may be of interest.
- When discharging using KOH the anode experiences corrosion due to being in contact with KOH; this corrosion occurs even when no discharge is occurring. Therefore some corrosion will occur during assembly and disassembly of the battery cell. This report recommends to measure the time it takes to assemble and disassemble the battery cell during each measurement for higher accuracy regarding the amount of silicon corroded. Alternatively, the option could be taken to adjust the set up such that the time it takes to assemble and disassemble the battery cell is below the measurable limit. This limit would depend on the active area of the new battery cell.
- During the experiments with the RTIL in this report only the conductivity of the RTIL
  was measured and tested. It was found that this conductivity alone cannot explain the
  varying potential, a possible avenue of research is to study the changes in the electrolyte
  or the anode surface. This could be done through studying the electrolyte post discharge
  using spectral analysis or studying the surface of the anode under a Scanning Electron
  Microscope (SEM).
- During experiments using KOH it was found that the amount of silicon corroded increased with decreasing KOH concentration. During this thesis the cause of this increasing corrosion rate was not yet determined. However, Durmus et al. [37] has found that the corrosion should approach a maximum at approximately 6M KOH. Therefore it is recommended in a future experiment to look closer into the increased corrosion rate found in this report. Traditionally KOH corrosion rates increase with the temperature, it is a possibility that at lower concentrations of KOH an increase the temperature had occured, the temperature of the electrolyte was not measured during the experiments shown here.

- [1] S. Bilgen. "Structure and environmental impact of global energy consumption". In: Renewable and Sustainable Energy Reviews 38 (2014), pp. 890–902. ISSN: 1364-0321. DOI: https://doi.org/10.1016/j.rser.2014.07.004.
- [2] S. Shafiee and E. Topal. "When will fossil fuel reserves be diminished?" In: *Energy Policy* 37.1 (2009), pp. 181–189. ISSN: 0301-4215. DOI: https://doi.org/10.1016/j.enpol. 2008.08.016.
- [3] F. Martins, C. Felgueiras, M. Smitkova, and N. Caetano. "Analysis of Fossil Fuel Energy Consumption and Environmental Impacts in European Countries". In: *Energies* 12.6 (2019). ISSN: 1996-1073. DOI: 10.3390/en12060964.
- [4] O. W. in Daya. Years of fossil fuel reserves left. [Online; accessed 03-07-2023]. (2022). URL: https://ourworldindata.org/grapher/years-of-fossil-fuel-reserves-left.
- [5] T. G. Benton, A. Froggatt, L. Wellesley, O. Grafham, R. King, N. Morisetti, J. Nixey, and P. Schröder. "The Ukraine war and threats to food and energy security". In: *Chatham House—International Affairs Think Tank* (2022).
- [6] A. Kammer, J. Azour, A. A. Selassie, I. Goldfajn, and C. Rhee. "How war in Ukraine is reverberating across world's regions". In: *Washington: IMF, March* 15 (2022), p. 2022.
- [7] J. F. Adolfsen, F. Kuik, E. M. Lis, T. Schuler, et al. "The impact of the war in Ukraine on euro area energy markets". In: *Economic Bulletin Boxes* 4 (2022).
- [8] R. Lindsey and L. Dahlman. "Climate change: Global temperature". In: Available online: climate.gov (accessed on 22 June 2023) (2020).
- [9] G. Foster and S. Rahmstorf. "Global temperature evolution 1979–2010". In: *Environmental research letters* 6.4 (2011), p. 044022.
- [10] S. Rahmstorf, G. Foster, and N. Cahill. "Global temperature evolution: recent trends and some pitfalls". In: *Environmental Research Letters* 12.5 (2017), p. 054001.
- [11] Berkeleyearth. 10,000 Years of Carbon Dioxide. URL: https://berkeleyearth.org/dv/10000-years-of-carbon-dioxide/.
- [12] R. Wang, S. Hasanefendic, E. Von Hauff, and B. Bossink. "The cost of photovoltaics: Re-evaluating grid parity for PV systems in China". In: *Renewable Energy* 194 (2022), pp. 469–481. ISSN: 0960-1481. DOI: https://doi.org/10.1016/j.renene.2022.05. 101.
- [13] Z. Li. "Prospects of Photovoltaic Technology". In: *Engineering* (2022). ISSN: 2095-8099. DOI: https://doi.org/10.1016/j.eng.2022.07.008.
- [14] IRENA. "Renewable power generation costs in 2017". In: *Report, International Renewable Energy Agency, Abu Dhabi* (2018).
- [15] A. Louwen and W. van Sark. "Chapter 5 Photovoltaic solar energy". In: *Technological Learning in the Transition to a Low-Carbon Energy System*. Ed. by M. Junginger and A. Louwen. Academic Press, 2020, pp. 65–86. ISBN: 978-0-12-818762-3. DOI: https://doi.org/10.1016/B978-0-12-818762-3.00005-4.

[16] R. Wiser, K. Jenni, J. Seel, E. Baker, M. Hand, E. Lantz, and A. Smith. "Expert elicitation survey on future wind energy costs". In: *Nature Energy* 1.10 (2016), pp. 1–8.

- [17] IEA. Net renewable electricity capacity additions by technology, 2017-2024. [Online; accessed 03-07-2023]. (2023). URL: https://www.iea.org/data-and-statistics/charts/net-renewable-electricity-capacity-additions-by-technology-2017-2024.
- [18] NEA. How much electricity do solar panels produce? [Online; accessed 03-07-2023]. (2020). URL: https://www.nea.org.uk/who-we-are/innovation-technical-evaluation/solarpv/how-much-electricity-solar-produce/.
- [19] M. J. Bos. "Storage of renewable electricity in methanol: Technology development for CO2 air capture and conversion to methanol". In: (2019).
- [20] IEA. *Grid-Scale Storage*. [Online; accessed 03-07-2023]. (2022). URL: https://www.iea.org/reports/grid-scale-storage.
- [21] IEA. Evolution of Li-ion battery price. [Online; accessed 03-07-2023]. (2020). URL: htt ps://www.iea.org/data-and-statistics/charts/evolution-of-li-ion-battery-price-1995-2019.
- [22] IEA. An energy sector roadmap to carbon neutrality in China. [Online; accessed 03-07-2023]. (2021). URL: https://www.iea.org/reports/an-energy-sector-roadmap-to-carbon-neutrality-in-china.
- [23] N. Nitta, F. Wu, J. T. Lee, and G. Yushin. "Li-ion battery materials: present and future". In: *Materials today* 18.5 (2015), pp. 252–264.
- [24] W. He, W. Guo, H. Wu, L. Lin, Q. Liu, X. Han, Q. Xie, P. Liu, H. Zheng, L. Wang, X. Yu, and D.-L. Peng. "Challenges and Recent Advances in High Capacity Li-Rich Cathode Materials for High Energy Density Lithium-Ion Batteries". In: *Advanced Materials* 33.50 (2021), p. 2005937. DOI: https://doi.org/10.1002/adma.202005937.
- [25] Amprius. AMPRIUS PRODUCTS. [Online; accessed 03-07-2023]. (2023). URL: https://amprius.com/products/.
- [26] S. Zhao, Z. Guo, K. Yan, S. Wan, F. He, B. Sun, and G. Wang. "Towards high-energy-density lithium-ion batteries: Strategies for developing high-capacity lithium-rich cathode materials". In: *Energy Storage Materials* 34 (2021), pp. 716–734.
- [27] E. Eason. World lithium supply. 2010.
- [28] L. Kavanagh, J. Keohane, G. Garcia Cabellos, A. Lloyd, and J. Cleary. "Global lithium sources—industrial use and future in the electric vehicle industry: a review". In: *Resources* 7.3 (2018), p. 57.
- [29] A. G. Olabi, E. T. Sayed, T. Wilberforce, A. Jamal, A. H. Alami, K. Elsaid, S. M. A. Rahman, S. K. Shah, and M. A. Abdelkareem. "Metal-air batteries—a review". In: *Energies* 14.21 (2021), p. 7373.
- [30] Y. Liu, Q. Sun, W. Li, K. R. Adair, J. Li, and X. Sun. "A comprehensive review on recent progress in aluminum–air batteries". In: *Green Energy & Environment* 2.3 (2017), pp. 246–277.
- [31] P. Gu, Y. Xu, Y. Zhao, W. Liu, H. Xue, and H. Pang. "Electrocatalysis of Recharge-able Non-Lithium Metal–Air Batteries". In: *Advanced Materials Interfaces* 4.19 (2017), p. 1700589.

[32] A. R. Mainar, E. Iruin, L. C. Colmenares, A. Kvasha, I. de Meatza, M. Bengoechea, O. Leonet, I. Boyano, Z. Zhang, and J. A. Blazquez. "An overview of progress in electrolytes for secondary zinc-air batteries and other storage systems based on zinc". In: *Journal of Energy Storage* 15 (2018), pp. 304–328. ISSN: 2352-152X. DOI: https://doi.org/10.1016/j.est.2017.12.004.

- [33] M. Fleischer. "The abundance and distribution of the chemical elements in the earth's crust". In: *Journal of Chemical Education* 31.9 (1954), p. 446.
- [34] S. Clark, A. Latz, and B. Horstmann. "A Review of Model-Based Design Tools for Metal-Air Batteries". In: *Batteries* 4.1 (2018). ISSN: 2313-0105. DOI: 10.3390/batteries401 0005. URL: https://www.mdpi.com/2313-0105/4/1/5.
- [35] X. Zhong, H. Zhang, Y. Liu, J. Bai, L. Liao, Y. Huang, and X. Duan. "High-Capacity Silicon–Air Battery in Alkaline Solution". In: *ChemSusChem* 5.1 (2012), pp. 177–180.
- [36] G. Cohn, D. Starosvetsky, R. Hagiwara, D. D. Macdonald, and Y. Ein-Eli. "Silicon-air batteries". In: *Electrochemistry Communications* 11.10 (2009), pp. 1916–1918. ISSN: 1388-2481. DOI: https://doi.org/10.1016/j.elecom.2009.08.015.
- [37] Y. E. Durmus, Ö. Aslanbas, S. Kayser, H. Tempel, F. Hausen, L. De Haart, J. Granwehr, Y. Ein-Eli, R.-A. Eichel, and H. Kungl. "Long run discharge, performance and efficiency of primary Silicon—air cells with alkaline electrolyte". In: *Electrochimica acta* 225 (2017), pp. 215–224.
- [38] G. Cohn and Y. Ein-Eli. "Study and development of non-aqueous silicon-air battery". In: *Journal of Power Sources* 195.15 (2010), pp. 4963–4970.
- [39] B. Dilasari, Y. Jung, and K. Kwon. "Effect of water on the stability of zinc in 1-butyl-1-methylpyrrolidinium bis(trifluoromethylsulfonyl)imide ionic liquid". In: *Journal of Industrial and Engineering Chemistry* 45 (2017), pp. 375–379. ISSN: 1226-086X. DOI: https://doi.org/10.1016/j.jiec.2016.10.005.
- [40] G. Book. "Compendium of chemical terminology". In: *International Union of Pure and Applied Chemistry* 528 (2014).
- [41] C. Puente and I. López. "Direct Electrochemical Synthesis of Metal Complexes". In: (2018). Ed. by B. Kharisov, pp. 87–141. DOI: https://doi.org/10.1016/B978-0-12-811061-4.00003-7.
- [42] H. Xu, B. Chen, P. Tan, W. Cai, W. He, D. Farrusseng, and M. Ni. "Modeling of all porous solid oxide fuel cells". In: *Applied Energy* 219 (2018), pp. 105–113.
- [43] W. Wang, X. Wei, D. Choi, X. Lu, G. Yang, and C. Sun. "Electrochemical cells for medium-and large-scale energy storage: fundamentals". In: (2015), pp. 3–28.
- [44] M. Carmo and D. Stolten. "Energy storage using hydrogen produced from excess renewable electricity: Power to hydrogen". In: (2019), pp. 165–199.
- [45] S. Hosseini, S. Masoudi Soltani, and Y.-Y. Li. "Current status and technical challenges of electrolytes in zinc–air batteries: An in-depth review". In: *Chemical Engineering Journal* 408 (2021), p. 127241. ISSN: 1385-8947. DOI: https://doi.org/10.1016/j.cej. 2020.127241.
- [46] K. M. Abraham and Z. Jiang. "A Polymer Electrolyte ☐ Based Rechargeable Lithium/Oxygen Battery". In: *Journal of The Electrochemical Society* 143.1 (1996), p. 1. DOI: 10. 1149/1.1836378.

[47] D. H. Dang, K. A. Thompson, L. Ma, H. Q. Nguyen, S. T. Luu, M. T. N. Duong, and A. Kernaghan. "Toward the circular economy of Rare Earth Elements: a review of abundance, extraction, applications, and environmental impacts". In: *Archives of Environmental Contamination and Toxicology* 81.4 (2021), pp. 521–530.

- [48] R. Coerkamp. "Mitigating the corrosion reaction in alkaline silicon-air batteries through nonuniform doping". In: *TU delft repository* (2022). URL: http://resolver.tudelft.nl/uuid:81622d57-82fc-4d33-9d8c-206c674c809b.
- [49] D. Chen, Y. Li, X. Zhang, S. Hu, and Y. Yu. "Investigation of the discharging behaviors of different doped silicon nanowires in alkaline Si-air batteries". In: *Journal of Industrial and Engineering Chemistry* 112 (2022), pp. 271–278. ISSN: 1226-086X. DOI: https://doi.org/10.1016/j.jiec.2022.05.020.
- [50] Q. Liu, Z. Pan, E. Wang, L. An, and G. Sun. "Aqueous metal-air batteries: Fundamentals and applications". In: *Energy Storage Materials* 27 (2020), pp. 478–505. ISSN: 2405-8297. DOI: https://doi.org/10.1016/j.ensm.2019.12.011.
- [51] T. B. Reddy. *Linden's Handbook of Batteries, Fourth Edition*. en. Fourth Edition. New York: McGraw-Hill Education, (2011). ISBN: 9780071624213. URL: https://www.accessengineeringlibrary.com/content/book/9780071624213.
- [52] J. Fu, Z. P. Cano, M. G. Park, A. Yu, M. Fowler, and Z. Chen. "Electrically rechargeable zinc–air batteries: progress, challenges, and perspectives". In: *Advanced materials* 29.7 (2017), p. 1604685.
- [53] Y. Li and H. Dai. "Recent advances in zinc–air batteries". In: *Chemical Society Reviews* 43.15 (2014), pp. 5257–5275.
- [54] G.-G. Park, Y.-J. Sohn, T.-H. Yang, Y.-G. Yoon, W.-Y. Lee, and C.-S. Kim. "Effect of PTFE contents in the gas diffusion media on the performance of PEMFC". In: *Journal of Power Sources* 131.1-2 (2004), pp. 182–187.
- [55] H. A. Gasteiger, S. S. Kocha, B. Sompalli, and F. T. Wagner. "Activity benchmarks and requirements for Pt, Pt-alloy, and non-Pt oxygen reduction catalysts for PEMFCs". In: *Applied Catalysis B: Environmental* 56.1 (2005), pp. 9–35. ISSN: 0926-3373. DOI: htt ps://doi.org/10.1016/j.apcatb.2004.06.021.
- [56] J. Prins. "Alkaline Pre-treatment of the Air Electrode in a Silicon-air Battery". In: *TU Delft repository* (2020).
- [57] R. Holze. "Electrochemistry of silicon and its oxides." In: Journal of Solid State Electrochemistry 7.5 (2003), pp. 318–319. ISSN: 1432-8488. DOI: 10.1007/s10008-003-0371-2.
- [58] H. Seidel, L. Csepregi, A. Heuberger, and H. Baumgärtel. "Anisotropic etching of crystalline silicon in alkaline solutions: I. Orientation dependence and behavior of passivation layers". In: *Journal of the electrochemical society* 137.11 (1990), p. 3612.
- [59] E. D. Palik, H. F. Gray, and P. B. Klein. "A Raman Study of Etching Silicon in Aqueous KOH". In: *Journal of The Electrochemical Society* 130.4 (1983), p. 956. DOI: 10.1149/1.2119866.
- [60] Y. E. Durmus, S. S. M. Guerrero, Ö. Aslanbas, H. Tempel, F. Hausen, L. De Haart, Y. Ein-Eli, R.-A. Eichel, and H. Kungl. "Investigation of the corrosion behavior of highly As-doped crystalline Si in alkaline Si–air batteries". In: *Electrochimica acta* 265 (2018), pp. 292–302.

[61] R. Gilliam, J. Graydon, D. Kirk, and S. Thorpe. "A review of specific conductivities of potassium hydroxide solutions for various concentrations and temperatures". In: *International Journal of Hydrogen Energy* 32.3 (2007), pp. 359–364.

- [62] D. W. Armstrong, L. He, and Y.-S. Liu. "Examination of ionic liquids and their interaction with molecules, when used as stationary phases in gas chromatography". In: *Analytical Chemistry* 71.17 (1999), pp. 3873–3876. DOI: 10.1021/ac990443p.
- [63] F. Javed, F. Ullah, M. R. Zakaria, and H. M. Akil. "An approach to classification and hi-tech applications of room-temperature ionic liquids (RTILs): A review". In: *Journal of Molecular Liquids* 271 (2018), pp. 403–420. ISSN: 0167-7322. DOI: https://doi.org/ 10.1016/j.molliq.2018.09.005.
- [64] F. Béguin, V. Presser, A. Balducci, and E. Frackowiak. "Carbons and electrolytes for advanced supercapacitors". In: *Advanced materials* 26.14 (2014), pp. 2219–2251.
- [65] G. Cohn, D. D. Macdonald, and Y. Ein-Eli. "Remarkable impact of water on the discharge performance of a silicon–air battery". In: *ChemSusChem* 4.8 (2011), pp. 1124–1129.
- [66] K. Matsumoto, J. Ohtsuki, R. Hagiwara, and S. Matsubara. "Cesium fluorohydrogenate, Cs(FH)2.3F". In: *Journal of Fluorine Chemistry* 127.10 (2006). Special 2006 ACS Award Issue ": For Creative Work in Fluorine, pp. 1339–1343. ISSN: 0022-1139. DOI: https://doi.org/10.1016/j.jfluchem.2006.04.009.
- [67] R. Hagiwara, K. Matsumoto, Y. Nakamori, T. Tsuda, Y. Ito, H. Matsumoto, and K. Momota. "Physicochemical properties of 1, 3-dialkylimidazolium fluorohydrogenate room-temperature molten salts". In: *Journal of the electrochemical society* 150.12 (2003), p. D195.
- [68] Y. Shodai, S. Kohara, Y. Ohishi, M. Inaba, and A. Tasaka. "Anionic Species (FH)xF-in Room-Temperature Molten Fluorides (CH3)4NF·mHF". In: *The Journal of Physical Chemistry A* 108.7 (2004), pp. 1127–1132. ISSN: 1089-5639. DOI: 10.1021/jp036607u.
- [69] N. Jacob. "Si-air Battery: Alkaline cell modelling in MATLAB (Simscape)". In: *TU Delft repository* (2020).
- [70] M. Vranes, S. Dozic, V. Djeric, and S. Gadzuric. "Physicochemical Characterization of 1-Butyl-3-methylimidazolium and 1-Butyl-1-methylpyrrolidinium Bis (trifluoromethylsulfonyl) imide". In: *Journal of Chemical & Engineering Data* 57.4 (2012), pp. 1072–1077.
- [71] N. Shah and I. Mukhopadyay. "Electrodeposition of Silicon (Si) from ionic liquid at room temperature (for EWT solar cell)". In: *Materials Today: Proceedings* 4.14 (2017), pp. 12716–12721.
- [72] N. Lang and W. Kohn. "Theory of metal surfaces: work function". In: *Physical Review B* 3.4 (1971), p. 1215.
- [73] LabChem. *Potassium Hydroxide 30% w/v*. [Online; accessed 22-06-2023]. (2018). URL: https://www.labchem.com/tools/msds/msds/LC19240.pdf.
- [74] A. Inoishi, T. Sakai, Y.-W. Ju, S. Ida, and T. Ishihara. "A rechargeable Si–air solid state oxygen shuttle battery incorporating an oxide ion conductor". In: *Journal of Materials Chemistry A* 1.48 (2013), pp. 15212–15215.
- [75] A. Epshtein, I. Baskin, M. Suss, and Y. Ein-Eli. "Rechargeable Silicon Redox Batteries".In: Advanced Energy Materials 12.30 (2022), p. 2201626.
- [76] A. A. N. EC08. "Basic overview of the working principle of a potentiostat/galvanostat (PGSTAT)–Electrochemical cell setup". In: *Metrohm Autolab. BV* (2011), pp. 1–3.

[77] K. R. Williams and R. S. Muller. "Etch rates for micromachining processing". In: *Journal of Microelectromechanical systems* 5.4 (1996), pp. 256–269.

- [78] C. Bohling and W. Sigmund. "Self-limitation of native oxides explained". In: *Silicon* 8 (2016), pp. 339–343.
- [79] B. E. Deal and A. Grove. "General relationship for the thermal oxidation of silicon". In: *Journal of applied physics* 36.12 (1965), pp. 3770–3778.



## Error Calculation Dektak

This appendix will cover the error calculation attached to the Dektak step height measurement step by step. This will be done through a series of figures displaying the in between steps. First the raw data obtained from the Dektak is leveled, which is done using the following formula.

$$y(x)_{level} = y(x)_{initial} + x \frac{y(1) - y(x_{max})}{x_{max}}$$
(A.1)

Where  $y(x)_{level}$  is the leveled step height,  $y(x)_{initial}$  the initial step height, x a variable denoting the position of the step height measurement and  $x_{max}$  an extreme of the position.

Through this equation a leveled step height figure can be obtained, shown below in Figure A.1b are a sample step height measurement and the leveled step height next to each other.

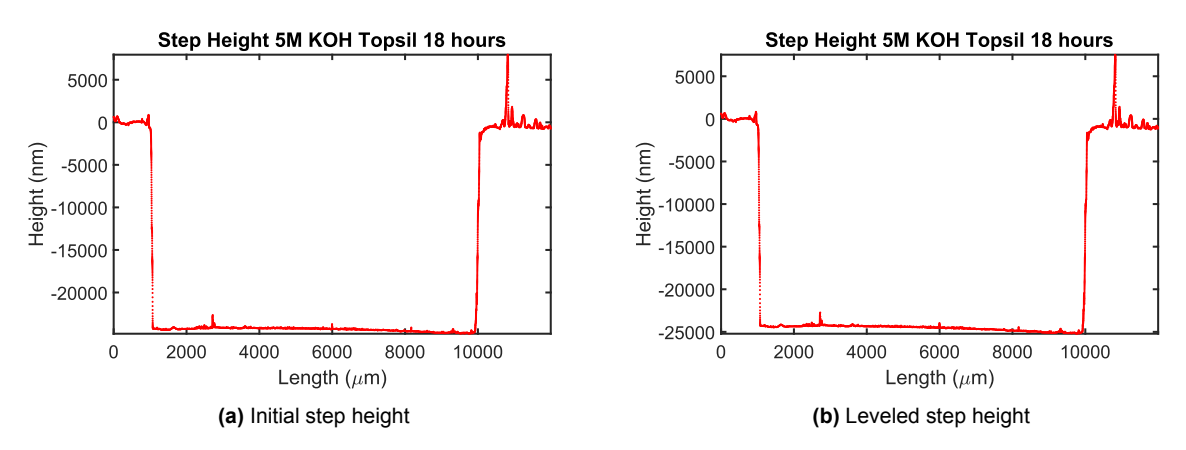


**Figure A.1:** Shown here are on the left side the initial step height as obtained from the Dektak and on the right side the leveled step height.

Seen in Figure A.1b are the step height before leveling off and after leveling off, on the left and right, respectively. Note that in this example the difference between the two figures is minimal.

The next step then becomes determining what the step height precisely is. As mentioned in the report the choice in this report was made to count all values within 10% of each extreme and to ignore the in between values as these are judged to be part of the transition between pre-step and post-step height. Shown below then are for the same measurement as given in Figure A.1a the pre-step heights and the post-step heights, further a fit is drawn through the points.

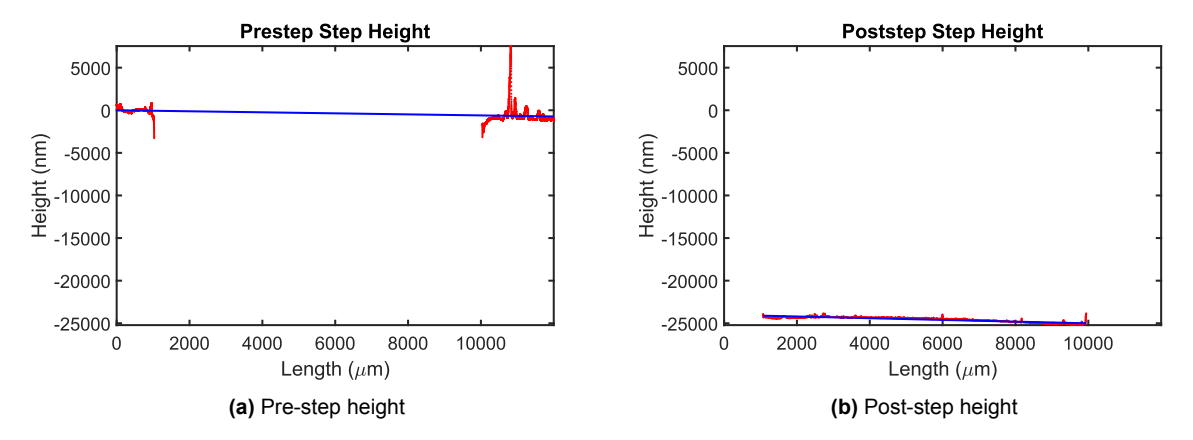


**Figure A.2:** Shown here are on the left side pre-step height and on the right side the post-step height with a fit included.

As can be seen in Figure A.2 some values are neglected for the pre-step and the post-step heights. Further shown in the figure are the first order polynomial fits through the data points, where the error is determined by taking the mean of the errors at each point. The actual step then can be determined by taking the difference between the mean of the fitted curves. The final error then is built up from the mean errors of both fits, in a similar manner as was done for the weight scale measurement in Section 3.3.

The mass then is determined using Equation

$$m_{\text{calculated}} = h_{\text{average}} A \rho_{\text{Si}}$$
 (A.2)

In which  $m_{\rm calculated}$  is the calculated mass in grams,  $h_{\rm average}$  the average step height in cm, A the active surface area in cm<sup>2</sup> and  $\rho_{\rm Si}$  the density of Si in g/cm<sup>3</sup>.

## Active surface area

In this appendix the active surface area is examined. This is done as the initial assumption of 1 cm<sup>2</sup> being the active area was found to be wrong. See Figure 4.5 for reference. Adjusting the surface area to 1.6 cm<sup>2</sup> gives a more aligned graph, shown in Figure B.1.

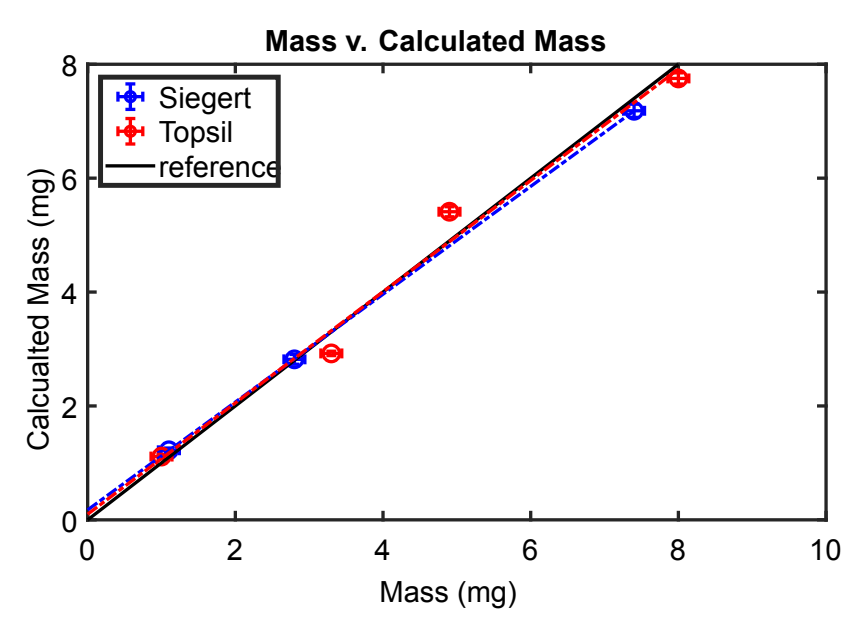
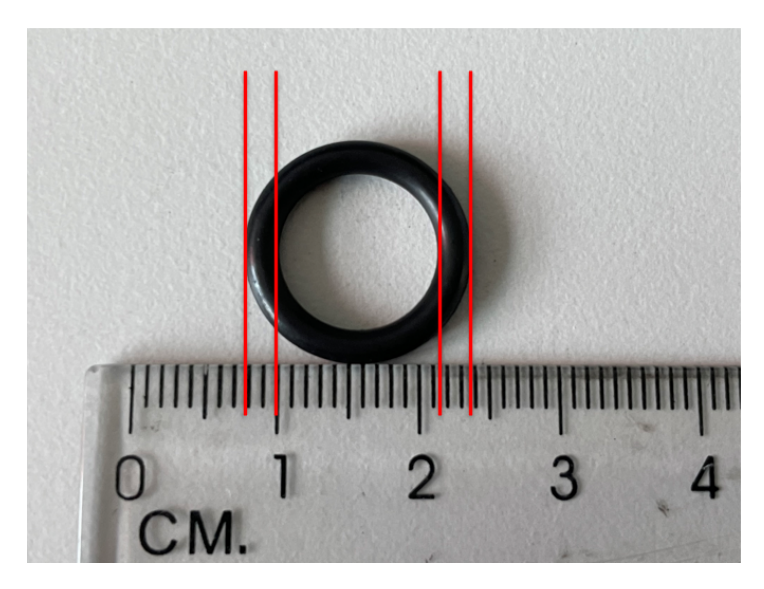


Figure B.1: Shown here is the mass versus the calculated mass, using an area of 1.6 cm<sup>2</sup>.

Seen here in Figure B.1 a high degree of correlation between the reference line and the two fits. Given that this result is obtained from setting the surface are to 1.6 cm<sup>2</sup>, it can be concluded that the actual surface area must lie between 1.5 and 1.7 cm<sup>2</sup>.

The question then is if this is a feasible conclusion, to determine this, the O-rings are studied in closer detail, shown in Figure B.2 is an small O-ring above a ruler. Red lines are added to increase visibility of the sizes.



**Figure B.2:** Shown here is an small O-ring intended to be placed on the anode sample. The inner and outer diameter are visualized by usage of the red lines and the ruler at the bottom.

Seen in Figure B.2 is that the O-ring has an inner diameter of approximately 1.1 cm, this diameter corresponds with a surface area of 1 cm<sup>2</sup>, however, the O-ring is circular, thus the KOH could feasibly seep underneath the O-ring and thus increase the active surface area. Using the outer two red lines, it can be seen that the outer diameter of the O-ring is approximately 1.5 cm, corresponding with a surface area of 1.8 cm<sup>2</sup>. This result shows the feasibility of the active surface area being between 1.5 and 1.7 cm<sup>2</sup>, as this size would still lie within the total area of the O-ring.

To observe whether or not this actually is occurring on the samples, three arbitrary samples that were discharged using KOH were picked, to be laid next to a ruler as shown in Figure B.3. Again red lines are added for ease of viewing the distances involved.

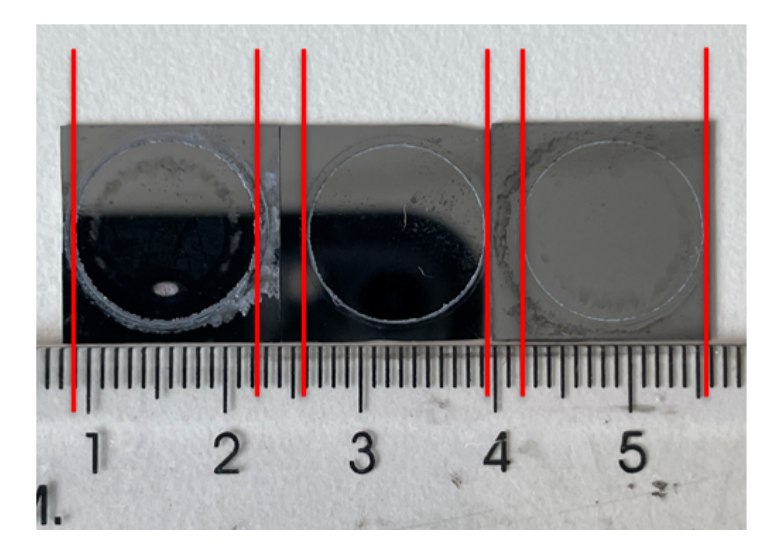


**Figure B.3:** Shown here are three samples which were discharged using KOH. The red lines indicate the size of diameter of the corroded area with assistance from the ruler below.

As can be seen in Figure B.3 the diameter of the corroded surface is larger than 1.1 cm, with diameters of 1.3-1.4 cm being observable. This result then, shows that the KOH during the

discharge of the battery seeps underneath the O-ring and the active area is larger than the inner area of the O-ring.